N73-12872

MSC-07561

NASA TECHNICAL MEMORANDUM

NASA TM X-58102
November 1972

CASE FILE
COPY

A STUDY OF HEAVY TRANS-IRON PRIMARY COSMIC RAYS ($Z \geq 55$) WITH A FAST FILM CERENKOV DETECTOR

A Dissertation Presented to the
Faculty of the Graduate School of the
University of Rochester; Rochester, New York
in Partial Fulfillment of the
Requirements for the Degree of
Doctor of Philosophy

NATIONAL AERONAUTICS AND SPACE ADMINISTRATION

MANNED SPACECRAFT CENTER

HOUSTON, TEXAS 77058

1. Report No.	2. Government Accession No.	3. Recipient's Catalog No.
NASA TM X-58102		

4. Title and Subtitle	5. Report Date
A STUDY OF HEAVY TRANS-IRON PRIMARY COSMIC RAYS ($Z \geq 55$) WITH A FAST FILM CERENKOV DETECTOR	November 1972
	6. Performing Organization Code

7. Author(s)	8. Performing Organization Report No.
Lawrence Steven Pinsky, MSC	MSC-07561
	10. Work Unit No.
9. Performing Organization Name and Address	951-16-00-00-72
Manned Spacecraft Center Houston, Texas 77058	11. Contract or Grant No.
	13. Type of Report and Period Covered
12. Sponsoring Agency Name and Address	Technical Memorandum
National Aeronautics and Space Administration Washington, D.C. 20546	14. Sponsoring Agency Code

15. Supplementary Notes

16. Abstract

This research is concerned with the detection and measurement of the cosmic ray charge spectrum for nuclei heavier than iron (Fe, Z = 26). These "trans-iron" nuclei are of great interest for several reasons. First, they promise to be one of the more sensitive clocks for use in determining the age of cosmic rays. The discovery of radioactive nuclides and their decay products in the primary flux, will allow an estimation of the elapsed time since these cosmic rays were synthesized. In addition, the relatively short interaction length of the very heavy trans-iron particles (~ 0.5 gm/cm^2 for $Z \sim 90$ nuclei in hydrogen) makes their relative abundance a fruitful source of information regarding the amount of interstellar matter that they had to traverse to reach the earth. Further, a study of the trans-iron cosmic rays may provide clues as to the very processes of nucleosyntheses by which the bulk of the trans-iron nuclei in the universe are produced. This in turn may shed light on the mechanics of the supernova, which is postulated to be the major source of all cosmic rays. Finally, trans-iron cosmic ray experiments may demonstrate the existence of the recently postulated "super-heavy" nuclei (Z = 110-114).

17. Key Words (Suggested by Author(s))	18. Distribution Statement
*Astrophysics-Cosmology *Nucleosyntheses *Cosmic Rays *Interstellar Radiation *Radiation Detectors	

19. Security Classif. (of this report)	20. Security Classif. (of this page)	21. No. of Pages	22. Price
None	None	231	

Page intentionally left blank

A STUDY OF HEAVY TRANS-IRON PRIMARY COSMIC RAYS ($Z \geq 55$) WITH A FAST FILM CERENKOV DETECTOR

by

Lawrence Steven Pinsky

Submitted in Partial Fulfillment
of the
Requirements for the Degree

DOCTOR OF PHILOSOPHY

Supervised by Gautam D. Badhwar

Department of Physics and Astronomy

The University of Rochester
Rochester, New York

1972

Page intentionally left blank

VITAE

Lawrence Steven Pinsky was born in [redacted] on [redacted] He entered Carnegie Institute of Technology (now Carnegie-Mellon University), Pittsburgh, Pennsylvania, in September 1964, as a physics major. He received his Bachelor of Science Degree in June 1968, and entered the Physics Department of the University of Rochester as a first year graduate student in September of the same year. During that first year, he held a research assistantship with the Cosmic Ray Group and worked with Professors J. G. M. Duthie and G. D. Badhwar. During the latter half of his first year at the University of Rochester, he was notified that he was to be drafted in June 1969, at the end of his second graduate semester. With this in mind, and since he had completed the other Master's Degree requirements, he was administered a Master's qualifying examination by Professors M. F. Kaplon and J. G. M. Duthie. A Master of Arts Degree in Physics was subsequently awarded to him in June 1969.

Mr. Pinsky was inducted into the United States Army on June 19, 1969, and received a direct commission as a second lieutenant in the Corps of Engineers on September 12, 1969. After completing his military schooling, he was assigned to the Manned Spacecraft Center in Houston, Texas, where he joined the Cosmic Ray Physics Branch, then headed by Dr. Donald Hagge, and subsequently by Dr. Richard Kurz. Lt. Pinsky was re-enrolled in absentia at the University of Rochester in September 1970, and with Professor G. D. Badhwar as his advisor,

he conducted the research on the fast film Cerenkov detectors presented in this dissertation. He successfully completed the Ph.D. qualifying examination in January, 1971.

While at the Manned Spacecraft Center, Lt. Pinsky has simultaneously undertaken a number of additional experiments. Along with Dr. W. Z. Osborne of the University of Houston, he has conducted the Apollo Light Flash Investigation which is aimed at explaining the nature of the "flashes of light" which are thought to be due to Z>10 cosmic rays, observed by the Apollo astronauts. Further, he has in collaboration with Professor P. J. McNulty, and Dr. V. P. Bond, undertaken an examination of the light flash phenomenon at a number of the particle accelerators around the country. Lt. Pinsky has, in collaboration with Dr. E. V. Benton of the University of San Francisco, flown emulsion and plastic detector stacks on all of the Apollo missions since Apollo 13. He has also provided fast film Cerenkov detectors for the LAPE II (Large Area Plastic Experiment) balloon flight which was conducted as a joint effort by R. Filz of the Air Force Cambridge Research Laboratory, Bedford, Massachusetts, and Dr. W. Enge of the University of Kiel in Germany.

ACKNOWLEDGMENTS

The author wishes to acknowledge the help that has been contributed to this research. This work was conducted at and funded by the National Aeronautics and Space Administration's Manned Spacecraft Center in Houston, Texas. It was undertaken as part of the CREPE (Cosmic Ray Emulsion Plastic Experiment) Program whose scientific head is Dr. W. Z. Osborne, and to whom the author feels a very personal debt of gratitude. Dr. Osborne contributed many hours of valuable discussions and suggestions on almost every facet of the development and analysis of the fast film Cerenkov detectors. The other members of the CREPE Program at the Manned Spacecraft Center who contributed to such tasks as nuclear emulsion scanning, and balloon flight operations were Dr. Richard Eandi and Rudi B. Rushing. The plastic track detector data presented in this dissertation was entirely the work of Dr. P. Buford Price's group at the University of California at Berkeley, and most notably the effort of Edward Shick and Dr. Edward Kobetich. The balloon flight operations were conducted by Winzen Research Inc., Minneapolis, Minnesota, and the fast film Cerenkov detectors were fabricated and processed by the Itek Corporation, Lexington, Massachusetts. The author especially wishes to acknowledge the help of Ronald Carbonier, Robert Vandle and John Sullivan of Itek. The Eastman Kodak Company, Rochester, New York, has been very helpful in supplying the required film and developing materials, and Richard Madigan of Kodak, deserves a special acknowledgment for his efforts.

At the University of Rochester, the author wishes to acknowledge the invaluable and everpresent assistance of Betty Cook, the graduate student advisor, and Professor Gautam Badhwar. Professor Badhwar first introduced the author to the idea behind the fast film Cerenkov detectors and has since served as his thesis advisor, for which the author would like to acknowledge his grateful appreciation.

Finally, the author wishes to thank his wife, Brenda, whose love, devotion and perseverance at the typewriter have made this dissertation possible.

TABLE OF CONTENTS

APPENDICES

LIST OF TABLES

LIST OF FIGURES

LIST OF FIGURES (Continued)

FIGURES APPEARING IN THE APPENDICES

CHAPTER I

INTRODUCTION

1. INTRODUCTION TO THE GENERAL PROBLEM

It has been said that the astrophysicist differs from other physicists in that he has no control over the object of his studies. He cannot bring a star into the laboratory and subject it to different tests at his convenience; he cannot create supernovae as he desires, nor can he change the vantage point nature has given him. Rather he must be content, for the present, with looking out into space at the information nature has seen fit to provide him. This information travels over vast interstellar, and even intergalactic, distances in the form of electromagnetic radiation, covering the entire energy spectrum from low frequency radio waves to > 100 MeV gamma rays. Similarly, other information is coming to us continually, in the form of charged particle radiation; and the cosmic ray physicist, like the astronomer, looks into space with his "telescopes", to gather this information.

The work presented here is concerned with the detection and measurement of the cosmic ray charge spectrum for nuclei heavier than iron (Fe, Z = 26). These "trans-iron" nuclei are of great interest for several reasons. First, they promise to be one of the more sensitive clocks for use in determining the age of cosmic rays. The discovery of radioactive nuclides and their decay products in

the primary flux, will allow an estimation of the elapsed time since these cosmic rays were synthesized. In addition, the relatively short interaction length of the very heavy trans-iron particles ($\sim$ 0.5 gm/cm^2 for Z $\sim$ 90 nuclei in hydrogen), makes their relative abundance a fruitful source of information regarding the amount of interstellar matter that they had to traverse to reach the earth. Further, a study of the trans-iron cosmic rays may provide us with clues as to the very processes of nucleosyntheses by which the bulk of the trans-iron nuclei in the universe are produced. This in turn may shed light on the mechanics of the supernova, which is postulated to be the major source of all cosmic rays. Finally, trans-iron cosmic ray experiments may demonstrate the existence of the recently postulated[1] "super-heavy" nuclei (Z = 110-114).

2. COSMIC RAYS

Cosmic rays were "discovered" in April 1912, when Victor Hess[2] found that the penetrating radiation responsible for discharging his electroscope, increased with altitude as his manned balloon ascended. For many years after its beginning, cosmic ray physics was limited to the study of extensive air showers, (i.e., the secondary particles produced by the interaction of the primary cosmic rays with the atmosphere). Techniques to lift detectors above most of the atmosphere were not perfected until the 1940's. Then, as the field grew, cosmic ray physics gave birth to high energy physics as the muon[3], the pion[4], the kaon[5] and even the

positron[6], were first discovered among the cosmic ray secondaries. With the advent of the high altitude balloon and the sounding rocket, nuclear track emulsions and cloud chambers[7] were used to confirm the earlier conclusions based on air shower data, that protons were the major component of the primary cosmic ray flux. Then, in 1948, Freier, et. al., [8, 9, 10], found the tracks of nuclei with $Z > 3$ in nuclear emulsions exposed during a high altitude balloon flight. It has since been established that a substantial amount of the primary flux is composed of He ($Z = 2$) nuclei, and about 1% by number are composed of the stripped nuclei of the elements heavier than He, extending up to the Uranium group elements ($88 < Z < 96$).

3. TRANS-IRON COSMIC RAYS

Until 1966, the entire body of cosmic ray data had yielded only one or two events that were possibly heavier than Fe, and it looked as though the spectrum might end there.[11]

At that time, Fleischer, et. al.,[12] were investigating the possibility of etching "fossil" cosmic ray tracks left in meteorite crystals. They reported numerous short tracks[13] which they attributed to the Bragg peak in the ionization, which occurs in the last few microns of the tracks of stopping Fe nuclei. Among these short tracks were several longer tracks, which they interpreted as being due to trans-iron primaries. This was the first substantial

evidence that trans-iron nuclei really did exist in the primary cosmic ray flux, and led to the first abundance estimate for trans-iron cosmic rays. Their value of 2×10^{-4} relative to Fe, compares favorably with current values.[14]

Fowler[15], inspired by these meteorite results, flew the first "large area" detector designed to search for trans-iron cosmic rays. Known as "Texas I", it was launched from Palestine, Texas, and consisted of 4 layers of nuclear emulsion in a 4.5 square meter array. The emulsion layers were interleaved with lead to give it a stopping power of 4 gm/cm^2. A stack of at least that thickness was required to obtain a measure of the cosmic ray particle energies. This was done by examining the change in the ionization rate as the particle penetrated through the stack. The ionization rate is proporational to Z^2/β^2 where β is the velocity of the particle relative to the velocity of light in a vacuum. This first flight yielded 13 tracks with $Z >> 26$[16] (including 2 with $Z \sim 90$), and about 2×10^5 Fe "group" (Cr, Fe, Ni) tracks. Thus, the integral flux for $Z >> 26$ came out at about 0.65×10^{-4} that of Fe which corresponded well with the meteorite measurements when corrections for solar modulation were taken into account. The most recent estimates indicate that $Z \gtrsim 90$ nuclei only compose about 1% of the trans-iron flux.[17]

Since that first flight there have been 14 other large area passive detector arrays flown,[18] including 6 more by Fowler[19] (Texas II, III, and IV; and 3 from Sioux Falls, S. D.); 3 by Blanford, et. al.,[20] (the "Barndoor" series); 2 by Filz, et. al.,[21] (the Large Area Plastic Experiment - LAPE series), and 3 by the Manned Spacecraft Center (the Cosmic Ray Emulsion Plastic Experiment - CREPE series). The earlier of these flights were configured similar to Fowler's original experiment, however, more recent arrays have contained sheets of etchable plastic track detectors in addition to the nuclear emulsions. (The latest attempt included an array with an area $\sim$ 75 m^2. Unfortunately, the entire gondola was lost due to a balloon termination malfunction.)

In addition to the balloon exposures, several small emulsion stacks have been flown onboard various U. S. and Russian spacecraft; however, the areas involved were insufficient to record more than one or two trans-iron events.

There have also been attempts to detect trans-iron cosmic rays with active counters. Binns, et. al.,[22] flew an instrument which consisted of parallel plate pulse ionization chambers and a Lucite Cerenkov counter. Their detector had an effective area of $\sim$ 1 m^2 ster, and as such, has proven too small to gather more than a few trans-iron primaries per balloon flight.

The total area-time exposure factor for all of the experiments mentioned in this section is $\sim$ 1.5 m^2 ster years,[23] and this exposure has yielded $\sim$ 210 events with $Z > 50$.[24]

4. TRANS-IRON DETECTORS

The recent work on trans-iron cosmic rays has led to two significant advances in detector techniques. The first is the development of the plastic track detectors mentioned in the previous section. This was an extension of the meteorite work by Fleischer, et. al.[25] It was discovered that certain plastics, most notably Lexan, Cellulose Triacetate and Cellulose Nitrate, could be etched in NaOH with the result that the tracks of heavily ionizing particles left cone shaped "etch pits" similar to those shown in Figure 1. They found further, that the etch rate, which is determined by measuring such parameters of the "pit", as depth and width, were directly related to the radiation damage rate, which is given by the expression:[26]

$$J = (aZ^{*2}/\beta^2)\ (\ell n\ (\beta^2/(1 - \beta^2)) - \beta^2 + K), \qquad (1)$$

where a and k are empirically chosen constants and Z* is the effective charge:

$$Z^* = Z\ (1 - \exp(-130\beta Z^{2/3})). \qquad (2)$$

From equation (1), it is clear that one needs some measure of the velocity in order to get an accurate charge estimate from these detectors. Previously employed methods for velocity measurements such as the use of "thick" detector arrays, have yielded charge determination accuracies as good as ± 4%.[27] Other uncertainties are introduced by the fact that the etch rates for similar tracks vary from sheet to sheet and even from place to place in the same sheet. Further, the etch rates tend to decrease with increasing time between exposure and etching,[28] and an additional complication is the fact that exposure to any ultra-violet radiation tends to enhance the etch rate.[29] These peculiarities can be worked around by scanning the area surrounding an event for stopping Fe tracks, to be used as a relative calibration. This calibration effort has been aided by the recent availability of heavy ions from accelerators. With these calibrations, the plastic track detectors have become one of the major tools in the trans-iron cosmic ray search.

The second significant advance in trans-iron detectors was an improvement in the emulsion measuring technique. As mentioned in Section 3, the ionization rate is proportional to Z^2/β^2, which for example, implies that a relativistic ($\beta \sim 1$), $Z \sim 50$ nucleus would have an ionization rate in emulsion similar to that of an Fe nucleus with $\beta \sim 0.5$. Thus, without some additional information about the velocity, the emulsions, when measured for simple ionization rate

FIGURE 1

ETCH PITS IN PLASTIC TRACK DETECTORS

This figure contains a pictorial representation of the pits left in a typical plastic track detector after etching. The successive sheets indicate the effects of the velocity decreasing through a stack. When the velocity is known in a given sheet, the parameters of the etch cone will yield a measure of the charge.

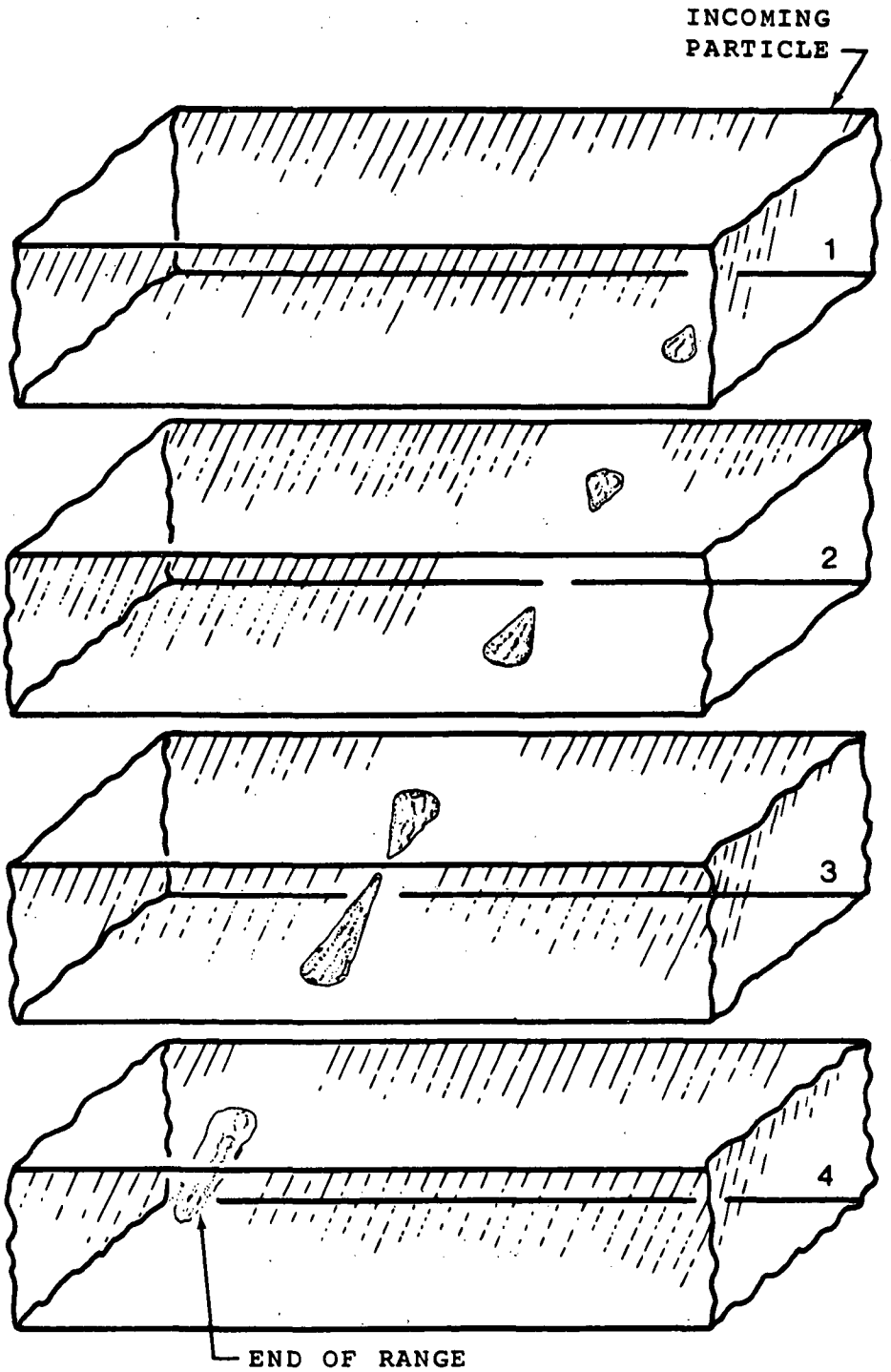

FIGURE 1

(such as by grain counts or core diameters), were plagued by large uncertainties in the charge estimates. The improvement in emulsion technique consists of measuring the energy spectrum of the δ-rays generated along the track of the particle in question. Rather than tracing the paths of individual δ-rays to obtain their ranges, one measures the probability of grain development as a function of the distance from the track. This grain development curve yields the same integrated information about the δ-ray energy spectrum as a compilation of the individual δ-ray ranges. Figure 2 is a plot of the radius for which 40% grain development above background occurs vs. the radius for which the probability of grain development is 0.1% above the background. The appropriate curves for Z = 30, 40, etc. are indicated, and successive points along a given curve correspond to increasing values of β. It is readily apparent that for $0.3 \lesssim \beta \lesssim 0.70$, a measurement of the two radii yields a unique value of both charge and velocity. The typical accuracy with which the two radii can be measured will yield an uncertainty in the charge estimate of approximately 2 charge units.[30] When β is $\gtrsim 0.70$, however, this uncertainty will be considerably greater. It can be seen from Figure 2 for example, that a particle with Z = 90, and $\beta \sim 1$ is virtually indistinguishable from a particle with Z = 75 and $\beta \sim 0.75$. This implies a total uncertainty of ∿ 15 charge units. If on the other hand, an independent measure of the velocity is available, the events with $\beta \gtrsim 0.7$ become easily distinguishable and the radii measurement accuracies will again yield charge assignment uncertainties approaching 2 charge units.

Currently, the emulsions and plastics flown in large area arrays represent the most viable method of gathering trans-iron cosmic ray data. The active detector systems flown to date have been too small to obtain more than a few trans-iron events per balloon flight, and until it becomes possible to fly these instruments on earth orbiting spacecraft to obtain long exposures, they will not compete with the passive arrays.

5. THE DRAWBACKS OF CONVENTIONAL VELOCITY DETERMINATION METHODS

From the discussion above, one can see that if nuclear emulsions and plastic track detectors are to provide accurate charge determinations, they require an independent measurement of the velocity, at least for particles with $\beta \gtrsim 0.70$. The two conventional methods used to obtain these energy or velocity measurements are: first, as mentioned above, flying thick stacks to slow or stop the particles, and second, to conduct several flights with slightly thinner stacks at different geomagnetic "cut-offs", and then by comparing all of the data, statistically deduce the spectrum. This second method becomes difficult in view of the very poor statistics which result from the extremely low fluxes. For example, if a 25 m^2 array were to be exposed for $\sim$ 80 hours at a low geomagnetic cut-off

FIGURE 2

R(0.4) vs. R(0.001)

This is a plot of the radius for which the probability of grain development in nuclear emulsion (such as Ilford G-5) due to δ-rays is 0.4, versus the radius for which the probability is 0.001. The appropriate curves for Z = 30, 40, etc., are plotted and successive points along a given curve correspond to increasing values of β. β is indicated at intervals of 0.1 along each curve.

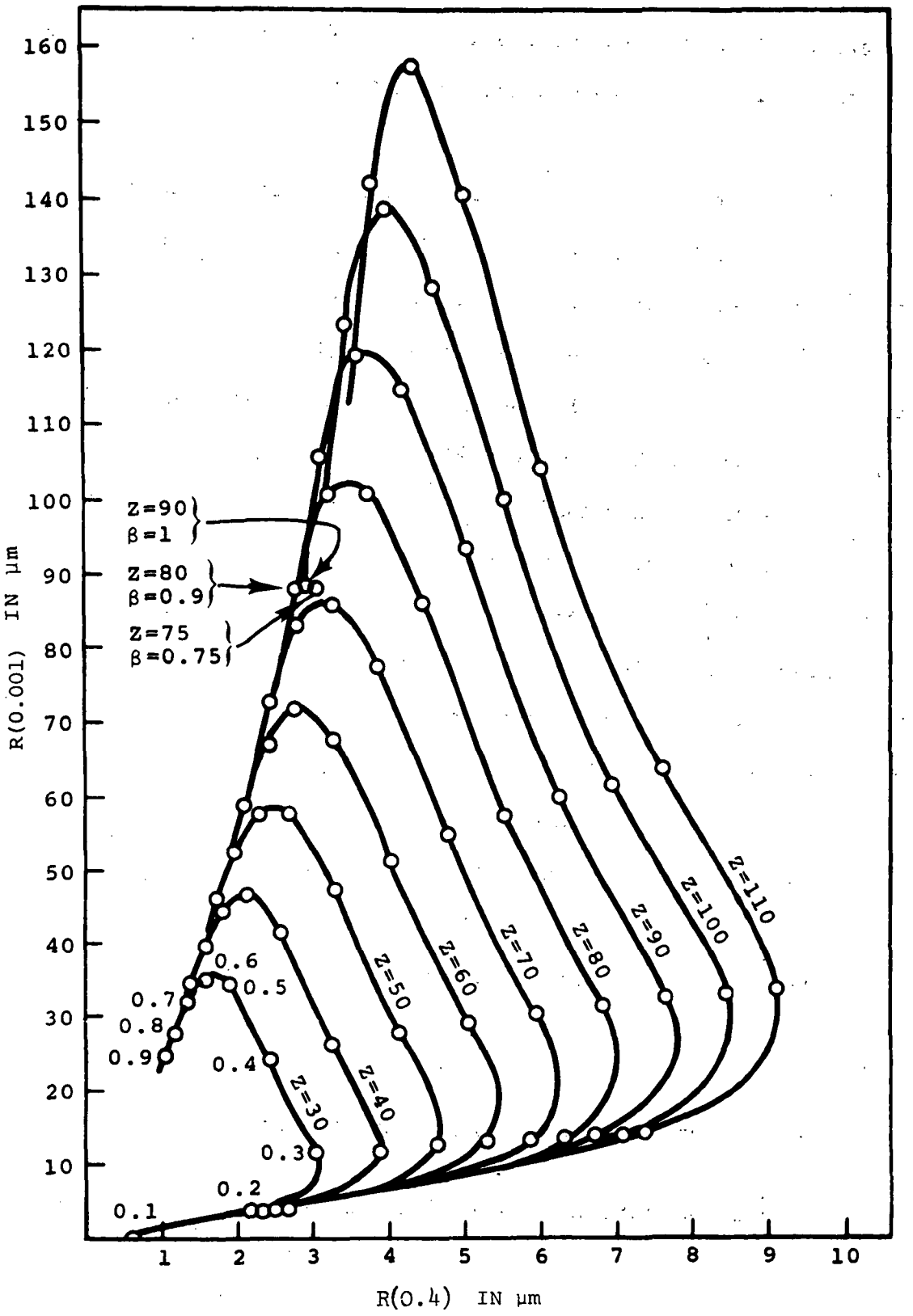
R(0.001) IN µm
R(0.4) IN µm
Z=90
β=1
Z=80
β=0.9
Z=75
β=0.75
Z=110
Z=100
Z=90
Z=80
Z=70
Z=60
Z=50
Z=40
Z=30
0.1
0.2
0.3
0.4
0.5
0.6
0.7
0.8
0.9

FIGURE 2

(e.g., 1.6 GV), with between 2.5 and 5 gm/cm^2 of residual atmosphere, it would collect only $\sim$ 64 events with $Z \gtrsim 50$.

The use of a thick stack to obtain an estimate of the velocity is extremely penalizing in balloon payload weight. Current gondola fabrication techniques allow an almost even weight to area trade-off; thus, if one could reduce the stack weight by half, the area could be literally doubled. In the past, stacks have been as thick as $\sim$ 10 gm/cm^2, solely to obtain velocity measurements. If an alternative method of velocity determination were available, these stacks could be reduced to < 1 gm/cm^2, and almost a factor of 10 area increase could be realized with the same balloon system. This thick stack method further suffers from the occurrence of nuclear interactions in the detector. When a primary nucleus fragments in the stack (10 gm/cm^2 of Pb represents $\sim$ 0.2 interaction lengths for a $Z \sim 90$ primary), one is denied a measure of the full range; and the energy estimate which results from an examination of that portion of the track which lies above the interaction, has the same uncertainties associated with it that the thinner stack experiments have.

6. A NEW INDEPENDENT VELOCITY DETERMINATION METHOD

The last few sections have been leading up to the requirement

for the development of a detector which will provide an independent measure of the velocity (at least for $\beta \gtrsim 0.70$), and that can be flown on balloons and spacecraft in the giant arrays along with the nuclear emulsions and the plastic track detectors. Any such detector should be extremely light and durable if it is to be of great material use. This is the motivation for the development and use of the Fast Film Cerenkov Detectors discussed in Chapter II.

Page intentionally left blank

CHAPTER II

FAST FILM CERENKOV DETECTORS

1. DESCRIPTION OF THE FAST FILM TRANS-IRON CERENKOV DETECTORS

A. Introduction

When a charged particle passes through a dielectric medium at a velocity that is greater than the phase velocity of light in that medium, it gives rise to a characteristic radiation, known as Cerenkov radiation.[31] It is directional and propagates as an azimuthally symmetric cone shaped wavefront. The basic idea behind the fast film Cerenkov detector (which was originally suggested by Badhwar, Deney, and Kaplon)[32] is to photographically record the Cerenkov light generated by a fast charged particle when it passes through a transparent dielectric medium such as depicted in Figure 3. The photographic image left on the film by the Cerenkov light, can be used to determine the velocity of the particle. This technique, however, is only useful for very heavy nuclei ($Z \gtrsim 50$), because of the current limitations in film sensitivity.

The Cerenkov wavefront propagates at an angle θ with respect to the radiating particle's trajectory, or "track". This angle is

FIGURE 3

THE BASIC DETECTOR CONCEPT

As shown in the pictorial representation of the fast film Cerenkov detector, a fast charged particle will give rise to Cerenkov radiation as it traverses the detector's "radiator" layer. This radiation will illuminate the "film" layer over a region bounded by a conic section, and an analysis of this image will yield a measure of the velocity of the radiating particle.

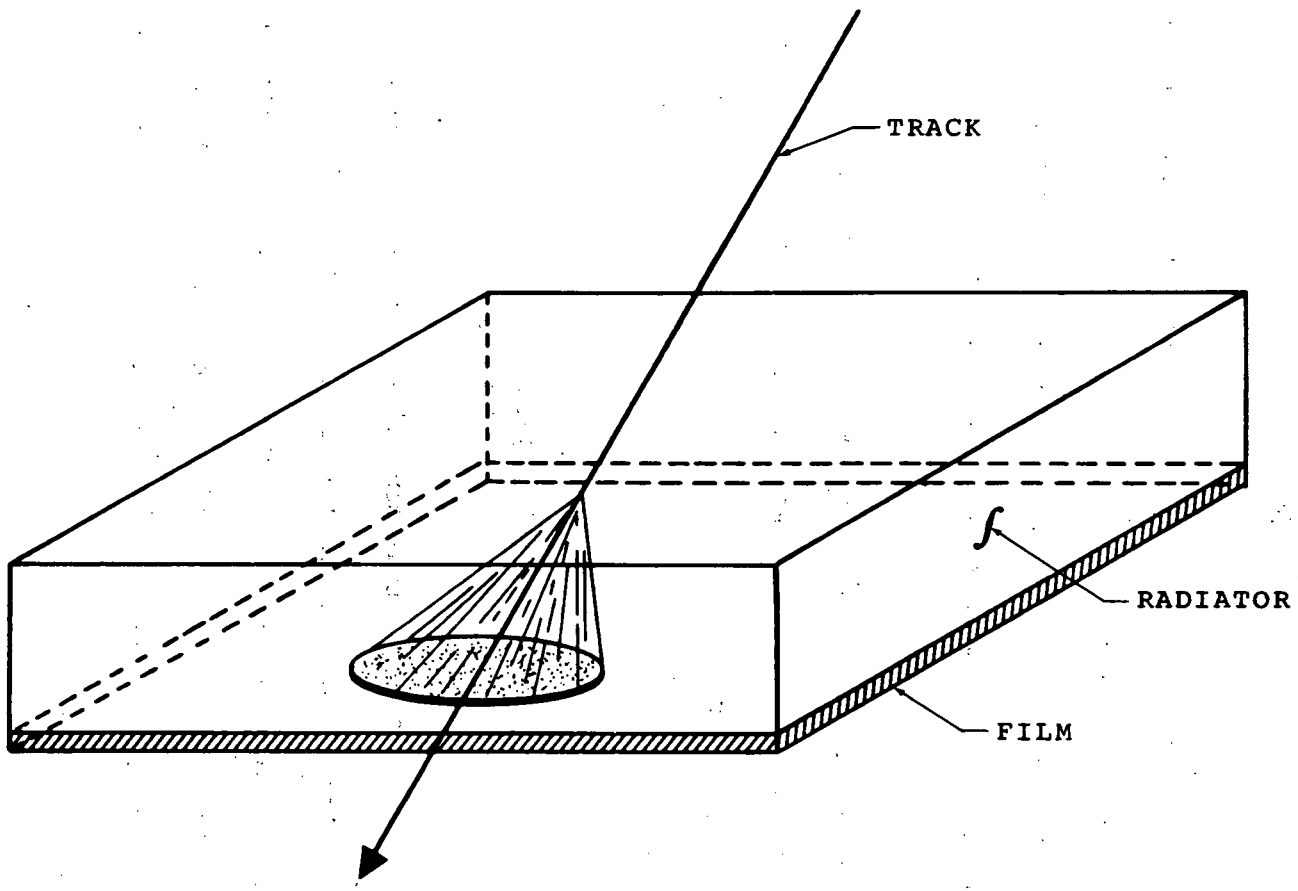

FIGURE 3

given by the relation:[33]

$$\cos \theta = \frac{1}{\beta n} \tag{3}$$

where n is the index of refraction of the medium. Since the index of refraction is the ratio of the phase velocity of light in the medium to that in a vacuum, the threshold velocity above which a charged particle will Cerenkov radiate is given by $\beta = 1/n$.

The number of Cerenkov photons within a spectral region defined by the wavelengths λ_1 and λ_2, emitted per unit path length by a particle of charge Ze, and velocity β, (in normal dielectric media) is given by:[34]

$$\frac{dN}{dl} = 2\pi Z^2 \alpha (1 - 1/\beta^2 n^2) \left(\frac{1}{\lambda_2} - \frac{1}{\lambda_1}\right) , \tag{4}$$

where $\alpha = e^2/\hbar c$. The spectral sensitivity of the film (see Appendix B) is such that our concern is limited to a region of wavelengths for which the index of refraction of the radiator is approximately constant. Let P be the number of Cerenkov photons emitted per unit path length that are observable on the film. Then, from equations (3) and (4), one can write:

$$P = 2\pi\alpha Z^2 \sin^2\theta \, f_{detector} = p \sin^2\theta , \tag{5}$$

where $p = 2 \pi \alpha Z^2 f_{detector}$, and $f_{detector}$ is defined by the term:

$$f_{detector} = \left(\frac{1}{\lambda_2} - \frac{1}{\lambda_1}\right) . \qquad (6)$$

λ_1 and λ_2, for the fast film Cerenkov detectors, are respectively the longer and shorter wavelength film sensitivity cut-offs. If the transparent dielectric Cerenkov radiator employed had possessed a transmission cut-off that was more limiting than the film sensitivity, then that cut-off wavelength would have to be used in equation (6), instead of the film's wavelength cut-off. Figure 4 is a plot of P as a function of β for a given Z and n.

There are two independent methods to obtain the velocity by an analysis of the Cerenkov radiation from a fast particle. From equation (5), a knowledge of the photon output, P, the charge, Z, the index of refraction, n, and the detector response, $f_{detector}$, will yield a measure of the velocity. From equation (3), a knowledge of the Cerenkov angle, θ, and the index of refraction, will also yield a measure of the velocity. It is this second method (i.e., measuring the Cerenkov angle, θ) that is employed by the fast film Cerenkov detectors.

The detector configuration will be discussed next, followed by detector design limitations, and then the mechanics of obtaining the Cerenkov angle, θ, from an analysis of the photographic image. The final section is devoted to photometry and photographic considerations.

FIGURE 4

β vs. P

The Cerenkov output P in photons per μm of track length is plotted vs. β for Z = 26, 50, 60, 70, 80, and 90. The index of refraction used in the plot is 1.484, which corresponds to the material employed in the actual radiator. The film sensitivity cut-offs for Eastman Kodak 2485 have also been incorporated in the plot.

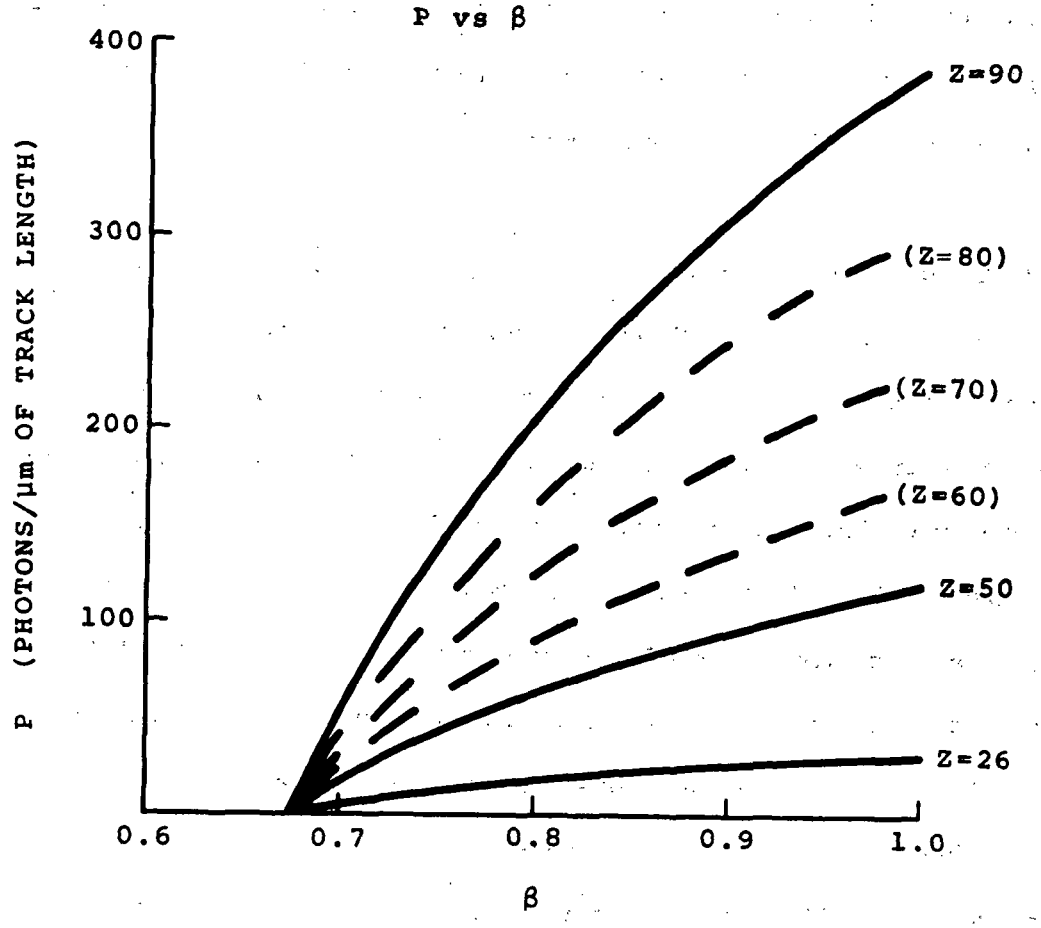
P vs β
400
300
200
100
P (PHOTONS/μm OF TRACK LENGTH)
Z=90
(Z=80)
(Z=70)
(Z=60)
Z=50
Z=26
0.6
0.7
0.8
0.9
1.0
β

FIGURE 4

B. Fast Film Trans-Iron Cerenkov Detector Configuration

The basic detector, is depicted in Figure 5. It consists of the highest speed film currently available, Eastman Kodak 2485 (EK 2485) in optical contact with a transparent polymer gel, similar to lucite. The index of refraction of the gel is matched with that of EK 2485 to eliminate interface reflections. This index of refraction is 1.484 at a wavelength of 5200 Å.

The polymer gel is poured between two sheets of EK 2485 film which are arranged with their emulsion sides facing. This is accomplished in a manner designed to prevent any bubbles from forming between the gel and the film. This sandwich is then pressed between two flat plates, which control the thickness of the gel while it cures. The gel is then in uniform optical contact with the film surfaces. The inclusion of a film surface on either side of the radiator is intended to allow for the examination of any images possibly occurring in the "upper" sheet. Images appearing in the upper sheet could not (in most cases[35]) be due to Cerenkov radiation, because of its directional nature. Rather, they could only be attributed to development caused by δ-rays similar to nuclear emulsion tracks, or to light generated by a scintallation of the radiator. Both effects are relatively symmetric with respect to the two sheets, and thus a comparison of the two images will allow these other competing effects to be removed from the analysis.

The opaque layer indicated in Figure 5, between the film emulsion and the Estar base, was required to prevent exposure of the film by any Cerenkov light or scintillation generated in the base itself. This layer, or anti-halation coating as it is called, becomes transparent during processing, allowing the film to be examined in a normal manner.

2. DESIGN CONSIDERATIONS

A. Detector Evolution

The first effort to photographically record these Cerenkov images was made by simply placing a sheet of Eastman Kodak 2485 film next to a thin plate of normal plexiglass, packaging them in a light tight container, and then exposing them to the primary cosmic ray flux.[36] This first attempt was inconclusive due to static electric discharges which occurred between the film and the plexiglass as they were separated. The discharges caused general fogging and marking of the highly sensitive film.

At this point, the approach described in the previous section was taken. Early attempts were made with a methyl methacrylate gel. This material proved to be too rigid for use as the Cerenkov radiator, because it imparted stresses to the EK 2485 emulsion. These stresses caused pressure marking. Butyl methacrylate was finally used as the radiator gel, and has proven flexible enough to

FIGURE 5

DETECTOR CONFIGURATION

This figure depicts the actual configuration of the fast film Cerenkov detectors which consisted of a plastic gel radiator sandwiched between two sheets of Estar backed Eastman Kodak 2485 film. The antihalation layer between the film emulsion and the Estar is provided to prevent exposure from the base side. The use of both an upper and a lower sheet is intended to allow an examination of any isotropic effects such as scintillation or film development caused by δ-rays.

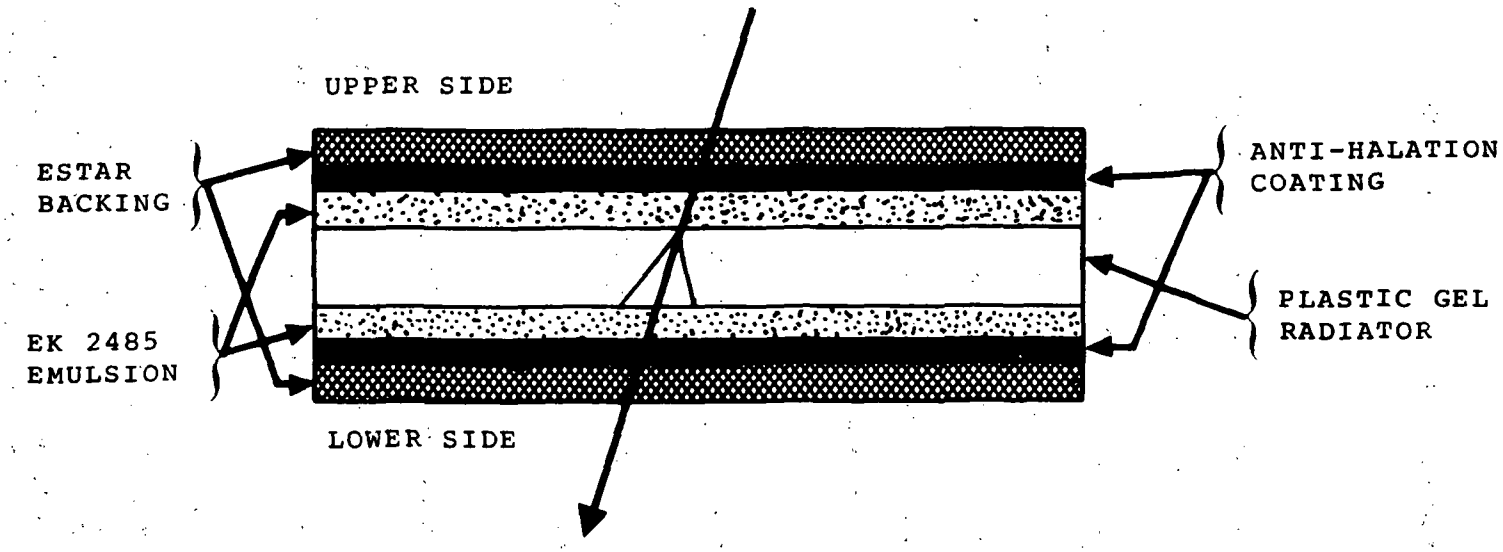
UPPER SIDE
ESTAR BACKING
EK 2485 EMULSION
LOWER SIDE
ANTI-HALATION COATING
PLASTIC GEL RADIATOR

FIGURE 5

allow the detector to withstand a 6 inch radius bend with no adverse effects.

This degree of complexity in fabrication was required due to the inability of Eastman Kodak to coat the 2485 photographic emulsion on any other base except Estar. Estar is exceedingly (and non-uniformly) birefrigent, which makes it unsuitable for our purposes. If it had been possible to coat the EK 2485 photographic emulsion on a suitable base, the base itself could have served as the Cerenkov radiator.

B. Fundamental Physical Problems

Before outlining the detector's basic capabilities, there are several limiting effects that must be discussed.

i) Cerenkov Angle Resolution

The resolution of Cerenkov angle, θ, is experimentally constrained by a number of factors.[37] Briefly, they are:

a) Scattering of the Radiating Particle.

The thickness of the radiator in the fast film trans-iron Cerenkov detectors is $\sim$ 100 μm. In this short distance, a relativistic trans-iron nucleus will undergo such slight Coulomb scattering, that any uncertainty in θ from this effect is quite negligible.

b) Energy Loss of the Radiating Particles

Since the Cerenkov angle is proportional to the velocity, the angle will change as the radiating particle slows. In the 100 μm radiator an average relativistic trans-iron nucleus will loose a total of $\sim$ 0.4 MeV/nuc. This implies $\Delta \theta \sim 10^{-4}$ rad.

c) Dispersion in the Medium

It was stated in Section 1, that for purposes of computing the total Cerenkov output, the index of refraction could be considered a constant. Actually the index of refraction increases from 1.482 at the film's cut-off wavelength, to 1.488 at the upper cut-off. For a given velocity, this difference in index of refraction will cause a maximum spread of $\Delta \theta \sim 1.4 \times 10^{-2}$ rad, between the directions of propagation of the shortest and longest wavelengths in the film sensitivity.

d) Diffraction of the Radiator

The width of the diffraction peak in the Cerenkov wavefront is given approximately by $\Delta \theta \sim \lambda/L \sin \theta$, where λ is the wavelength of the radiation, and L is the total radiation path length. For $\beta \gtrsim .7$, $\Delta \theta \lesssim 1.8 \times 10^{-2}$ rad.

e) Finite Film Grain Size

The mean diameter of the undeveloped grains in the EK 2485 film emulsion is about 0.5 μm. The angle subtended by one grain at 100 μm represents an approximate limit to the resolution of θ. This angle is, $\Delta \theta \sim 0.5 \times 10^{-2}$ rad.

Thus, the resolution of the Cerenkov angle is limited by an uncertainty of $\Delta \theta \lesssim (.014^2 + .018^2 + .005^2 + .0001^2)^{\frac{1}{2}} \sim 2.3 \times 10^{-2}$ rad. This translates into an uncertainty in β of $\lesssim 0.02$, for the worst case ($\beta \sim 1$).

ii) Cerenkov Radiation from δ-Rays

There is an additional effect that must be considered when the primary is very highly charged. In this case, the number of knock-on electrons (δ-rays) is considerable, and some fraction of these will possess velocities above the Cerenkov threshold. Thus, there will be a contribution to the total Cerenkov output from the secondary particles. The δ-ray spectrum is well known for the case of nuclear emulsions. Since the electron density is much greater in the emulsions than in the plastic Cerenkov radiators, the emulsion spectrum can be used as a worst case. Using this spectrum one finds that for a relativistic primary ($\beta \sim 1$) the number of δ-rays produced with $\beta \gtrsim .6$ is approximately $3 \times 10^{-4} Z^2$ per μm of track length. Thus for short track lengths $\sim$ 100 μm, this effect can be neglected.

iii) Development due to Ionization and Scintillation

It was pointed out in Section 1B that an upper sheet was included in the detector to evaluate any development caused by scintillation or δ-rays. The butyl methacrylate employed as a radiator is virtually free of scintillation. An examination of the upper sheets which correspond to lower sheets containing Cerenkov images, yields no evidence of any exposure due to scintillation.

The δ-rays generated by the radiating particle during its passage through 2485 film emulsion cause development in a region 5 μm in diameter. This is reasonable when compared with 5-10 μm nuclear emulsion core sizes. One expects the 2485 δ-ray development to be less because of the much lower electron density in the 2485 film emulsion. This ionization core represents a lower limit in the size of Cerenkov images which can be identified.

C. Detector Capabilities

The fast film Cerenkov detectors are primarily intended for use in determining the velocity of trans-iron nuclei with $\beta > 0.7$. They will in fact yield a measure of the velocity for nuclei with $Z \gtrsim 55$ and $\beta \gtrsim 0.68$. The mechanics of this measurement are discussed in the next section. In addition to the velocity, an analysis of the Cerenkov images will provide an estimate of the charge of the radiating particle. This is done by solving equation (5) for Z, if P is known. However, since the film sensitivity is highly non-linear, the uncertainty in P will cause a corresponding uncertainty in Z which will be considerably greater than the error in the emulsion and plastic charge assignments. Thus, even though the Cerenkov detectors possess some charge measuring capability, their principle role is in determining velocity.

The fast film Cerenkov detectors also satisfy the requirement that they be light and durable. Including packaging, they represent $\lesssim$ 0.2 gm/cm^2. They can be exposed to a space environment for extended periods, including temperatures as high as 50°C with very little degradation. Further, delays in processing after exposure can be as great as 6 months with no noticeable effect (if the storage is at $\lesssim$ 20°C). Pressure marking during handling is prevented by packaging the detector in 12" x 12" sheets, between two layers of thin cardboard. This configuration makes it possible to readily deploy the fast film Cerenkov detectors in the large area plastic and emulsion arrays.

In concluding these remarks on the detector capabilities, it may be worthwhile to point out that an examination of Cerenkov output will discriminate between a highly charged particle and a magnetic monopole. The monopole will radiate as $\overline{Z}^2\ n^2$ where $\overline{Z}$ is the pole strength of the monopole and n is the index of refraction.[38] Since a charged particle radiates as Z^2; for $Z \sim \overline{Z}$, a monopole would produce 2.25 times the charged particle Cerenkov output if n were $\sim$ 1.5. Since current theories predict pole strengths $\sim$ 137 [39], such an event would be hard to miss.

3. CERENKOV IMAGE GEOMETRY

In order to obtain the velocity of the particle from the Cerenkov image, one needs to know how the image depends upon all of the physical parameters. Since the Cerenkov light propagates in a cone shaped wavefront, the image on the lower film sheet will have the shape of a conic section. The parameters of the conic section (i.e., eccentricity and scale) are determined by the thickness of the radiator, T, the dip angle of the track, δ (the complement of the zenith angle), and the Cerenkov angle, θ.

Consider first the case of normal incidence ($\delta = \pi/2$) as depicted in Figure 6. Cerenkov light generated in track length dl, will fall entirely in the annular region with area dA. As mentioned in Section 1, the photon distribution will be azimuthally symmetric (independent of ϕ, the polar angle in the plane normal to the track). One can readily see that all of the light generated along the track below dl will fall on the film within the circle enclosed by the annular region dA; and that all of the light from the track above the element dl, will fall outside the region dA and its enclosed circle. Thus, for a radiator of thickness T, no light will fall beyond a radius $R = T \tan \theta$, and the image will be a circular area. The photon density, $\rho(r)$, as a function of the radial distance, r, from the track impact point is given by the number of photons

FIGURE 6

CERENKOV IMAGE GEOMETRY, NORMAL INCIDENCE

This diagram depicts the geometry for a normally incident ($\delta = \frac{\pi}{2}$) particle. A Cerenkov radiating particle will illuminate a circular region in the plane normal to the track. All of the light generated in the track length dl will fall in the annular region dA and the intensity distribution will be independent of ϕ.

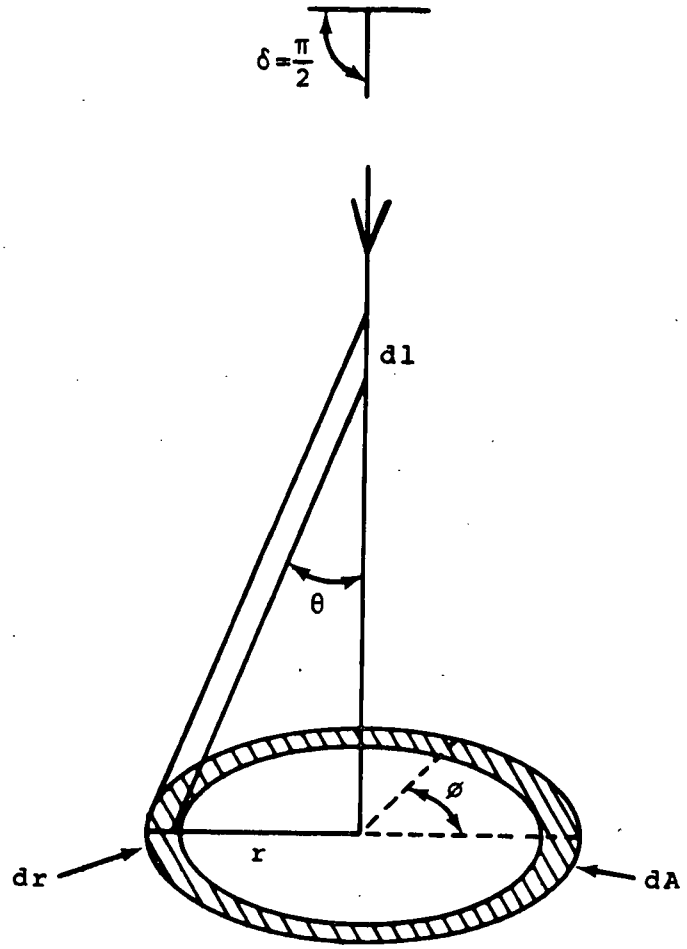

FIGURE 6

generated in the track length dl, divided by the area dA:

$$\rho(r) = \frac{P}{2\pi r \tan\theta} = \frac{p}{2\pi r} \sin\theta \cos\theta \quad , \tag{7}$$

where P is the number of photons generated per unit track length from equation (5).

For non-normal incidence, there are three cases in general; 1) for $\delta > \theta$ the image will be an ellipse; 2) for $\delta = \theta$, a parabola; and 3) for $\delta < \theta$, an hyperbola. Figure 7 illustrates the geometry for the elliptical case. The polar equation for the ellipse as a function of the parameters: δ, θ, and T, will now be derived.

The primed variables are polar coordinates in the film plane and their unprimed counterparts represent polar coordinates that are normal to the track. R and $R'(\phi')$ represent distances from the track impact point to the "edge" of the actual conic section, and r and r' are general polar coordinate radii.

The general equation of the ellipse shown in Figure 7 is given by the expression:

$$\frac{X^2}{a^2} + \frac{Y^2}{b^2} = 1 \quad , \tag{8}$$

where X and Y are the rectangular coordinates with respect to an origin located at the geometric center of the ellipse. a and b

are respectively the semi-major and semi-minor axes of the ellipse. Let X_o be the X coordinate of the track impact point which is located on the semi-major axis. From triangle CDE in Figure 7b one can see that:

$$X_o = a + d - T \tan\left(\frac{\pi}{2} - \delta\right) \quad , \tag{9}$$

where d is the distance from the edge of the ellipse to the vertical projection of the apex of the cone onto the plane of the ellipse. From triangle CBE, d is:

$$d = T \tan\left(\frac{\pi}{2} - \delta - \theta\right) \quad . \tag{10}$$

Thus, from (9) and (10) one finds:

$$X_o = T\left(\cot(\delta+\theta) - \cot\delta\right) + a \quad . \tag{11}$$

Next consider triangle ACE of Figure 7b:

$$2a + d = T \tan\left(\frac{\pi}{2} - \delta + \theta\right) \quad , \tag{12}$$

or combining this expression with (10):

$$a = \frac{T}{2}\left(\cot(\delta - \theta) - \cot(\delta + \theta)\right) \quad . \tag{13}$$

FIGURE 7

CERENKOV IMAGE GEOMETRY, ELLIPTICAL CASE ($\delta > \theta$)

Figure 7 shows the Cerenkov image geometry for the elliptical case ($\delta > \theta$), where a and b are respectively the semi-major and semi-minor axes of the ellipse, and X_o is the distance of the "track impact point" from the geometric center of the ellipse. ϕ' is the polar coordinate in the plane of the ellipse with its origin at the track impact point, measured from the semi-major axis. T is the thickness of the radiator (7b) and δ is the dip angle of the track.

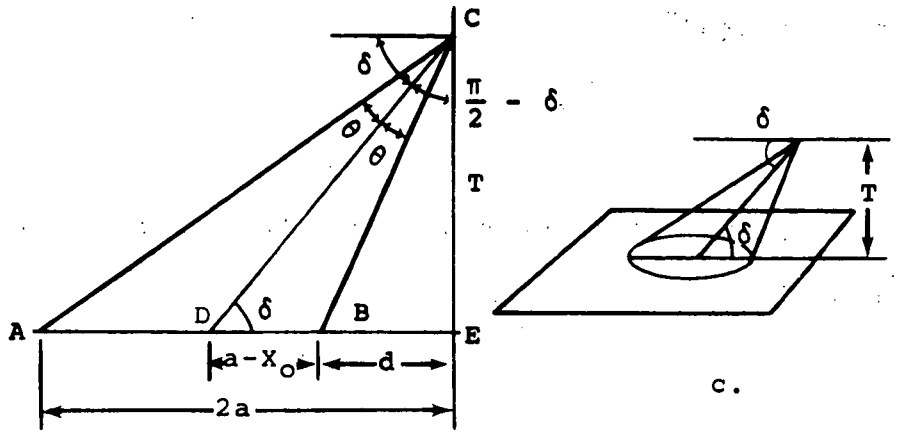
C
δ
π/2 - δ
θ
θ
T
A
D
δ
B
E
a - X_o
d
2a
b.
δ
T
δ
c.

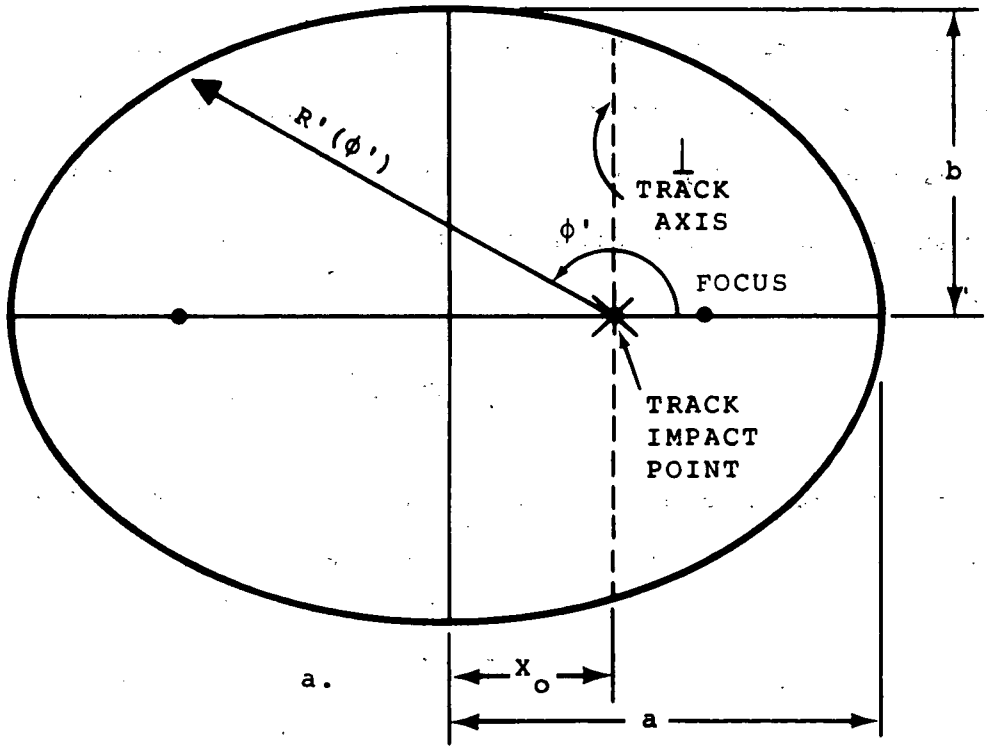
R'(φ')
TRACK
AXIS
φ'
FOCUS
b
TRACK
IMPACT
POINT
a.
X_o
a

FIGURE 7

To calculate b, one makes use of a general relation for the eccentricity given by:[40]

$$\varepsilon = \frac{\cos\delta}{\cos\theta} \quad , \tag{14}$$

which is valid for all conic sections. Since the eccentricity of the ellipse is given by:

$$\varepsilon = (1 - b^2/a^2)^{\frac{1}{2}} \quad , \tag{15}$$

one then has:

$$b = a\ (1 - \frac{\cos^2\delta}{\cos^2\theta})^{\frac{1}{2}} \quad . \tag{16}$$

Now, to obtain the polar equation of the ellipse with the origin located at the track impact point, we first require the parametric equation for X and Y as a function of ϕ', (the desired polar angle measured from the semi-major axis). Since, from equation (8):

$$Y = b\ (1 - X^2/a^2)^{\frac{1}{2}} \quad , \tag{17}$$

there is only one independent parametric relation. We may obtain the relation for X as a function of ϕ' by considering:

$$\tan\phi' = \frac{Y}{X - X_o} \quad , \tag{18}$$

then, with (17):

$$\tan\phi' = \frac{b\,(1 - X^2/a^2)^{\frac{1}{2}}}{X - X_o} \quad , \tag{19}$$

and finally solving (19) for X, one finds:

$$X = \frac{X_o \tan^2\phi' \pm b\,((1 - X_o{}^2/a^2)\tan^2\phi' + b^2/a^2)^{\frac{1}{2}}}{\tan^2\phi' + b^2/a^2} \quad . \tag{20}$$

The upper sign in equation (20) applies for $-\frac{\pi}{2} \geq \phi' \geq \frac{\pi}{2}$, since it yields only values of $X > X_o$, and similarly the lower sign gives only values of $X < X_o$ which implies that it is valid for $\frac{3\pi}{2} \geq \phi' \geq \frac{\pi}{2}$. From (20), (17) and the Pythagorean theorem, the polar equation of the conic section in the film plane, $R'(\delta,\theta,T;\phi')$, is finally obtained as:

$$R'(\delta,\theta,T;\phi') = ((X - X_o)^2 + b^2\,(1 - X^2/a^2))^{\frac{1}{2}} \quad . \tag{21}$$

Appendix A discusses the corresponding relations for the cases of parabolic and hyperbolic images.

Next we require the photon density as a function of r' and ϕ', the polar coordinates in the film plane. Consider Figure 8a. Since

FIGURE 8

GEOMETRY OF THE TRANSFORMATION FROM THE UNPRIMED TO THE PRIMED PLANE

a) The photons generated in the path length dl, which pass through the differential area element dA, will also pass through the area element dA' in the film plane.

b) To obtain the transformation of r as a function of r' and ϕ', consider triangles EFG and E'F'G. Since they are similar triangles, we have $\frac{r}{r'} = \frac{R}{R'(\phi')}$ or $r = r' \frac{T \tan\theta}{R'(\phi')\sin\delta}$ ($R = T \tan\theta/\sin\delta$ since $\overline{EG} = T/\sin\delta$).

c) To obtain the transformation of ϕ as a function of ϕ' consider the projection of the angle ϕ onto a plane tilted at an angle δ with respect to the track. Since the angle transformation does not depend on T (i.e., it must be the same for every dl from (a) above,) T can be set to ∞. In this case we have $AD = C'D'$, $AB = A'B'$, $\tan\phi = \frac{\overline{AB}}{\overline{AD}}$, and $\tan\phi' = \frac{\overline{C'B'}}{\overline{C'D'}}$. Then, since $\sin\delta = \frac{\overline{A'B'}}{\overline{C'B'}}$, we have $\tan\phi = \sin\delta \tan\phi'$.

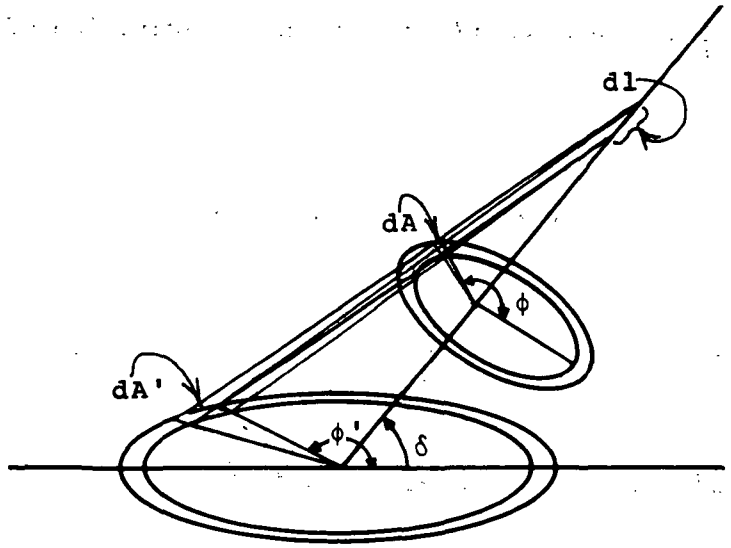

8a

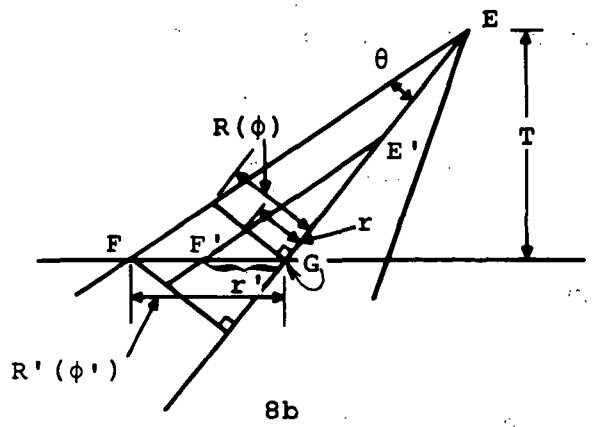

8b

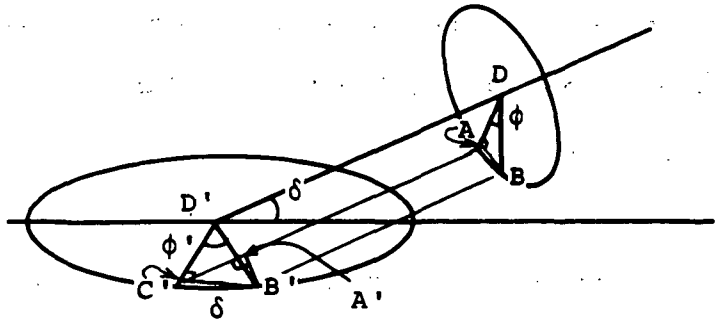

8c

FIGURE 8

we know $\rho(r, \phi)$ from equation (7) we can use conservation of photons to write:

$$\rho'(r',\phi')dA' = \rho(r,\phi)dA \quad , \tag{22}$$

or

$$\rho'(r',\phi') = \frac{dA}{dA'}\rho(r,\phi) = \frac{r\,dr\,d\phi}{r'dr'd\phi'}\rho(r,\phi) \quad . \tag{23}$$

Making use of the similar triangles EFG and E'F'G, indicated in Figure 8b, one has in a straightforward manner:

$$r = r' \frac{T\tan\theta}{R'(\phi')\sin\delta} \tag{24}$$

and differentiating,

$$\frac{dr}{dr'} = \frac{T\tan\theta}{R'(\phi')\sin\delta} \quad . \tag{25}$$

The angle transformation can be obtained by considering the projection of ϕ on to the primed plane as depicted in Figure 8c. Line segments $\overline{AB} = \overline{A'B'}$, $\overline{C'D'} = \overline{AD}$, and $\overline{B'C'} = \overline{C'D'}\tan\phi'$; then from the triangle A'B'C' one finds:

$$\tan\phi' = \sin\delta\,\tan\phi \quad , \tag{26}$$

and by differentiating inverse functions:

$$\frac{d\phi}{d\phi'} = \frac{\sec^2\phi' \sin\delta}{\sin^2\delta + \tan^2\phi'} \quad . \tag{27}$$

Now, combining equations (7), (23), (24), (25) and (27) one has the photon density function:

$$\rho(r',\phi') = \frac{Tp \sec^2\phi' \sin^2\theta}{2\pi r' R'(\phi')(\sin^2\delta + \tan^2\phi')} \quad . \tag{28}$$

This function has experimental significance in that the film response and even the film sensitivity threshold can be thought of in terms of the number of photons/μm^2 impinging on the film (hereafter referred to as the "photon density"). Let ρ_c be the minimum photon density required to cause a detectable exposure on the film. Then, if $\rho(R'(\phi'))$ (the photon density at the edge of the conic section) is $< \rho_c$, that portion of the conic section edge will not be observable on the film. Rather, for that ϕ', the photographic image edge will be given by a curve of constant photon density (iso-density curve), corresponding to ρ_c. It is possible for part of the photographic image edge to be determined by an iso-density curve while the balance of the photographic image edge is determined by the actual conic section edge. Examples of these "composite" edge curves are illustrated in Figure 9. The

FIGURE 9

COMPOSITE CURVES

a) Several iso-density contours are plotted for a typical ellipse.

b) An example of a composite curve where part of the edge is determined by the iso-density curve corresponding to the film sensitivity and the rest of the curve is determined by the actual conic section.

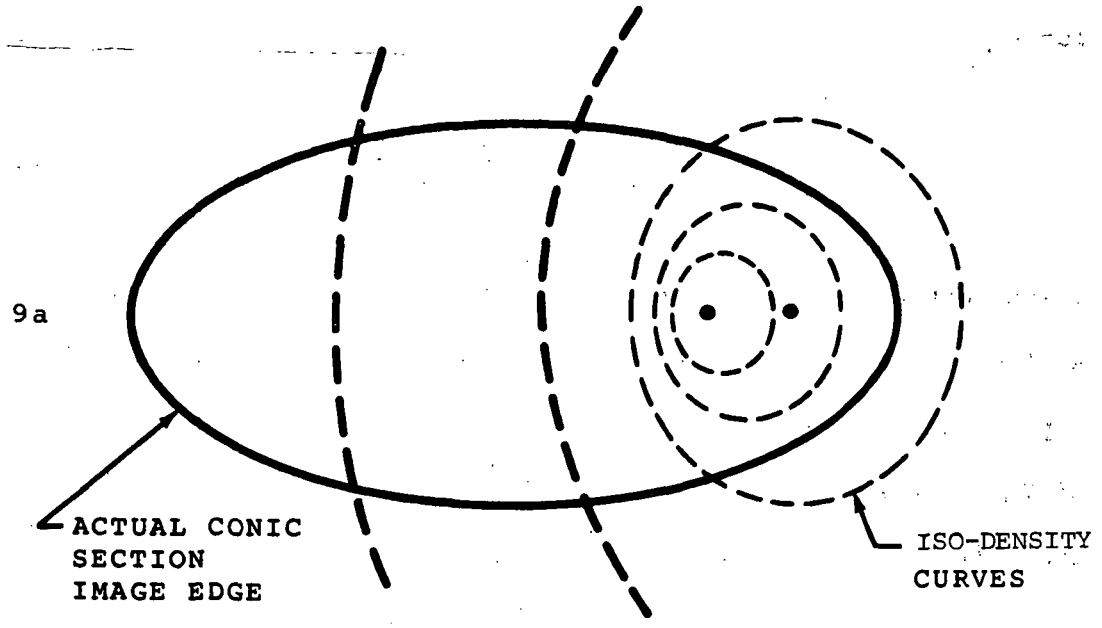
9a
ACTUAL CONIC SECTION IMAGE EDGE
ISO-DENSITY CURVES

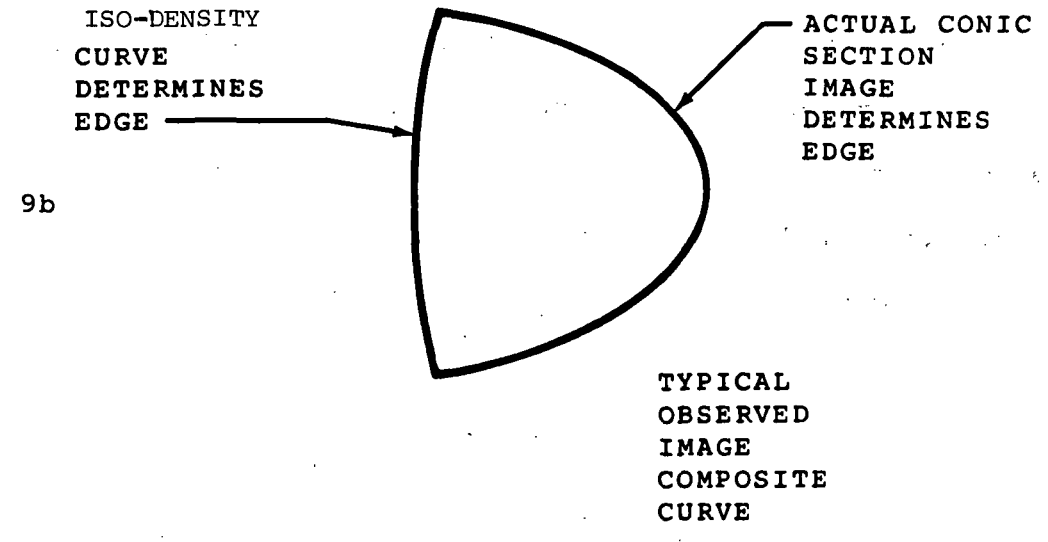
ISO-DENSITY CURVE DETERMINES EDGE
ACTUAL CONIC SECTION IMAGE DETERMINES EDGE
9b
TYPICAL OBSERVED IMAGE COMPOSITE CURVE

FIGURE 9

polar equation for the photon iso-density curve, r'_{ρ_c}, comes directly from equation (19), by replacing ρ with ρ_c and solving for r'_{ρ_c}:

$$r'_{\rho_c}(\phi') = T\left(\frac{p}{2\pi\rho_c}\right)\frac{\sec^2\phi'\,\sin^2\theta}{R'(\phi')\,(\sin^2\delta + \tan^2\phi')} \quad . \tag{29}$$

These photon density expressions are valid for all three conic section cases when the proper $R'(\phi')$ is used. Also, since the T dependence of $R'(\phi')$ can be factored out, $T/R(\phi')$ is independent of T, and therefore, so is r'_{ρ_c}. The polar equation for the composite edge curve, $F(\phi')$, for a given ρ_c, is then given by:

$$\begin{aligned} F(\phi') &= R'(\phi') \quad , r'_{\rho_c}(\phi') \geq R'(\phi') \\ &= r'_{\rho_c}(\phi') \quad , r'_{\rho_c}(\phi') < R'(\phi') \end{aligned} \tag{30}$$

In principle one can uniquely determine θ by fitting the edge of the observed image to either one of the composite edge curves, or to a conic section. δ and the proper semi-major axis orientation are known from the plastic and emulsion measurements, and T can be measured directly. The uniqueness of the shape of the conic section edge and the iso-density curves as a function of θ, comes directly from equation (14), which can be written in the form:

$$\cos\theta = \frac{\cos\delta}{\varepsilon} \quad . \tag{31}$$

Since δ is known, ε, the eccentricity of the conic section, which is a unique parameter of the shape is also a unique function of θ. From equation (29), r'_{ρ_c} is inversely proportional to $R'(\phi')$; therefore, the eccentricity of the iso-density curve is inversely proportional to the conic section eccentricity. The inverse proportionality still preserves the uniqueness.

Although theoretically unique, for $\delta \gtrsim 75°$ the iso-density curves approach being circles to the extent that the eccentricity is difficult to resolve. For these vertical tracks one must rely on resolving the conic section edge to allow an evaluation of θ from a fit to equation (21). For events where $\delta \lesssim 75°$, one can also fit interior iso-density curves to obtain values of θ, redundant to the edge fit, but independent of T.

4. PHOTOMETRY AND PHOTOGRAPHIC CONSIDERATIONS

As stated in Section 1, the film employed in the fast film Cerenkov detectors is EK 2485 which is the most sensitive photographic film currently available. The undeveloped grains are relatively coarse ($\sim$ 0.5 μm in diameter), and the overall sensitivity is slightly directional. The direction, or more properly, the side of maximum sensitivity is controlled at the time the film is coated. The spectral response is fairly flat across the visible wavelengths, dropping slightly in the red from 6000 Å to 7000 Å. The long wavelength cut-off is extremely sharp, and

occurs at about 7000 Å. The short wavelength sensitivity extends into the near ultra-violet, and the actual cut-off experienced at around 3000 Å is due to the transmission curve of the photographic gelation. The spectral sensitivity curve is included in Appendix B.

When the film is processed with extensive and uniform agitation, such as in a sensitometric processing machine, exposure levels down to approximately 1 photon/μm^2 are detectable with an efficiency of about 5%. The mean grain diameter after processing is $\sim$ 3 μm. As such, these low photon fluxes cause a grain development which is distinguishable above the background fog when the exposure is over a large enough total area. Figure 10 is an exposure vs. density plot[41] for the maximum speed attained. This processing was accomplished in an LB-10 sensitometer processing machine with MX-642 developer for 3 minutes at 33°C.

The film is extremely pressure sensitive and great care must be exercised during handling to prevent pressure marking. However, the film is relatively stable when subjected to temperature excursions and has been used at temperatures as high as 50°C and as low as -100°C, with little degradation in fog level. Further, excursions in atmospheric pressures from 1 atm to a hard vacuum, and changes in humidity from 0 to > 90% seem to have little effect.

Finally there seems to be no evidence of reciprocity failure with the ultra-short (Cerenkov) exposure durations, $\sim 10^{-12}$ sec.

Most films suffer differences in development between similar exposures of differing durations, even though the time integrated photon flux is the same for each case. This reciprocity failure is usually more prevalent when the exposures are longer than 1 sec. Shorter exposures generally do not exhibit such failures. Eastman Kodak 2485 has been tested[42] for reciprocity down to exposures as short as 10^{-9} sec. These tests have shown no evidence of reciprocity failure for times between 10^{-6} and 10^{-9} sec. The fast film Cerenkov detector results have extended these limits down to 10^{-12} sec.

Figure 11 is a plot of photon density in the Cerenkov image vs. radial distance from the track impact point for the case of normal incidence. The levels for Z = 26 (Fe), 40, 60, 80, and 100 are shown, along with the calculated region of δ-ray ionization development. The approximate threshold sensitivity of the film is indicated, and it is apparent that if the radiator is thick enough to make $R \gtrsim 100$ μm, there will be little chance of resolving the conic section edge. If the edge is not resolved, one has to fit iso-density curves, as discussed in the previous section.

FIGURE 10

EXPOSURE vs. DENSITY CURVE FOR THE EASTMAN KODAK 2485 AS PROCESSED

This exposure vs. density curve was obtained from a piece of film flown on CREPE II, that had been exposed to a calibrated step tablet prior to the detector fabrication. The processing was accomplished in an LB-10 sensitometric processor at 33°C (90°F) at a rate of 6 in./min.

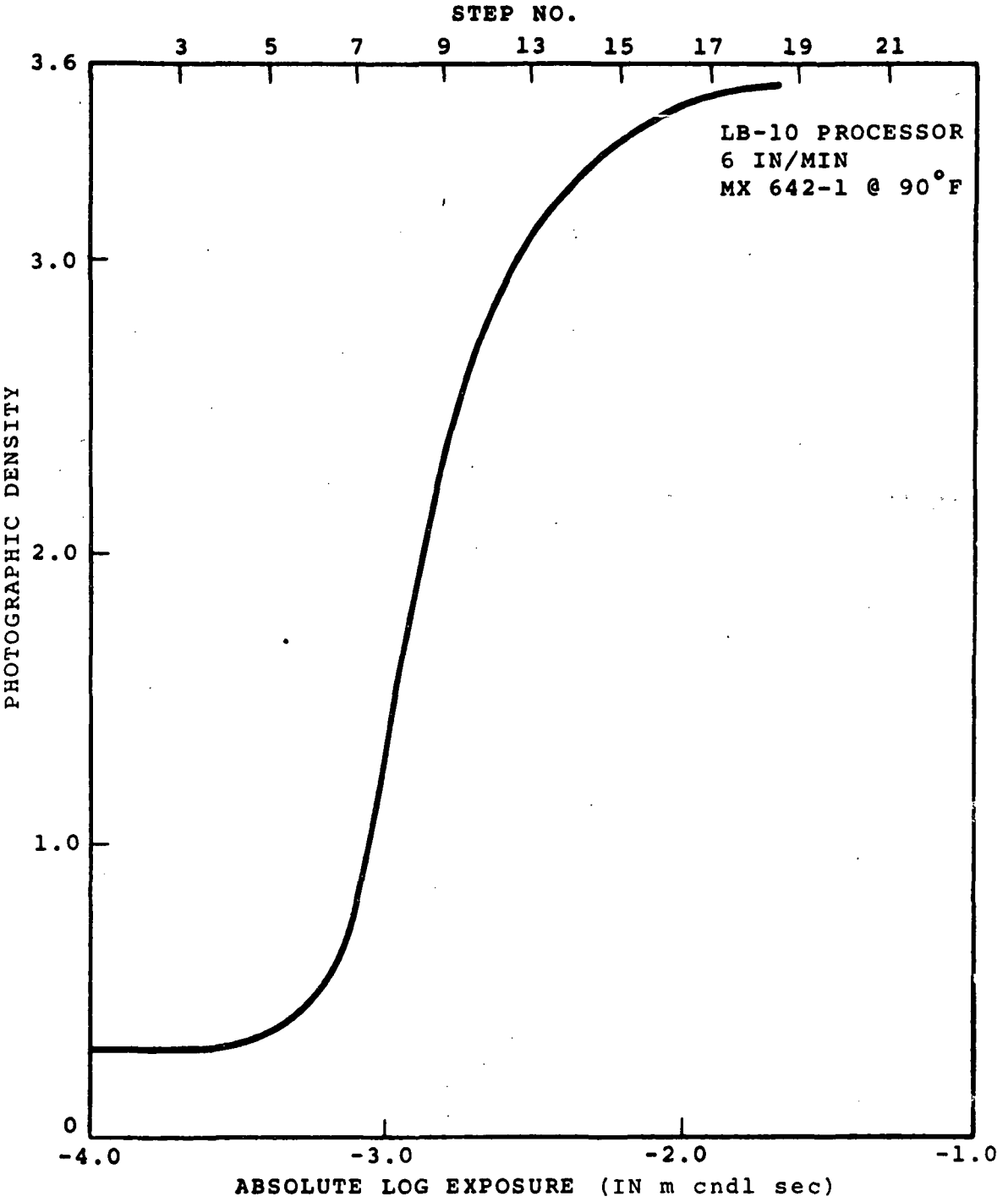
STEP NO.
3
5
7
9
13
15
17
19
21
3.6
3.0
2.0
1.0
0
LB-10 PROCESSOR
6 IN/MIN
MX 642-1 @ 90°F
PHOTOGRAPHIC DENSITY
-4.0
-3.0
-2.0
-1.0
ABSOLUTE LOG EXPOSURE (IN m cndl sec)

FIGURE 10

FIGURE 11

TYPICAL PHOTON DENSITY vs. RADIUS FROM TRACK

Photon density curves corresponding to several charge values for the case of normal incidence are plotted against the radial distance from the track impact point. The maximum sensitivity of the Eastman Kodak 2485 film is also plotted, and all of the radii for which the photon densities are above the film limit, would cause an exposure of the film.

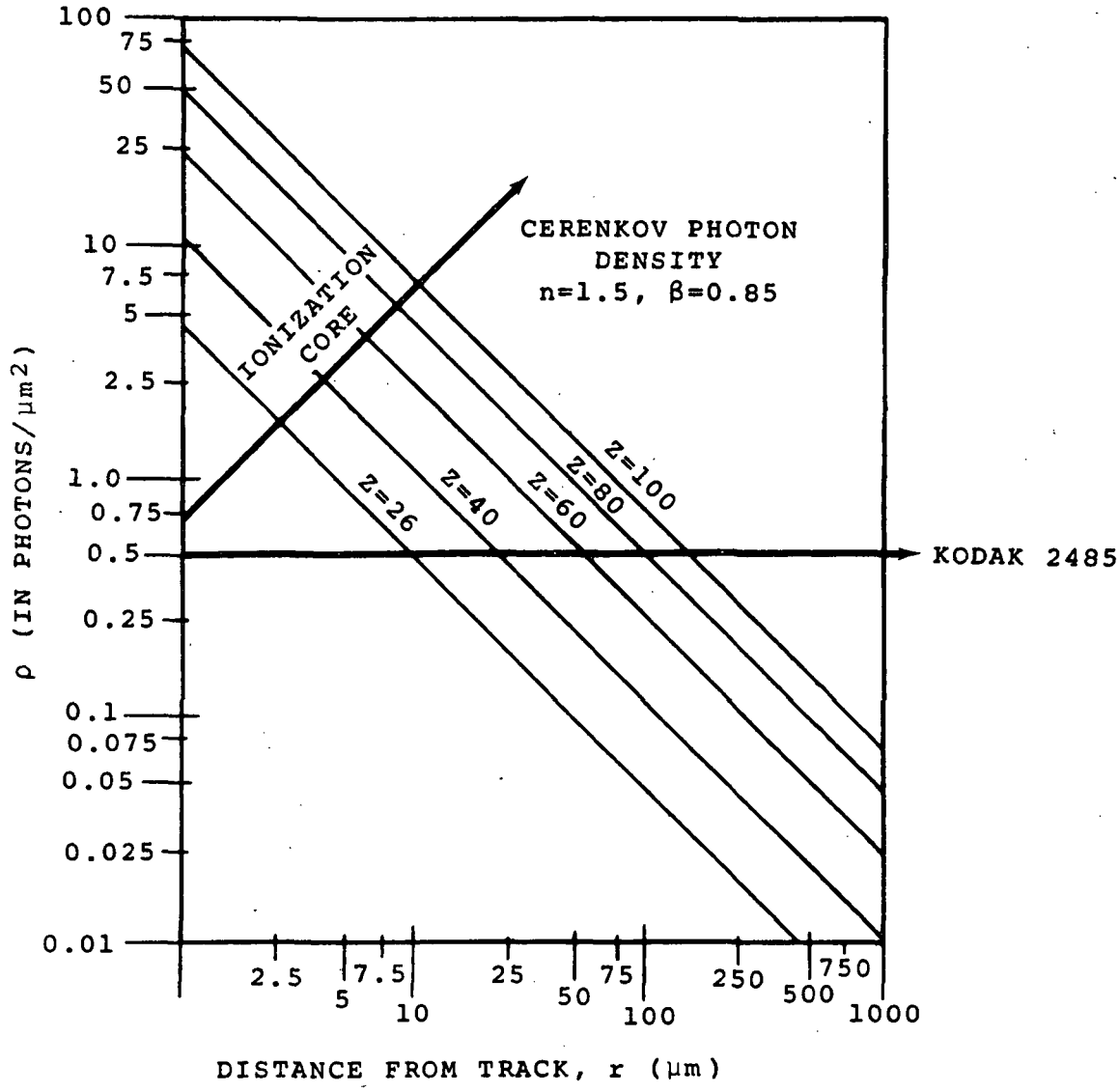
100
75
50
25
10
7.5
5
2.5
1.0
0.75
0.5
0.25
0.1
0.075
0.05
0.025
0.01
ρ (IN PHOTONS/μm2)
CERENKOV PHOTON
DENSITY
n=1.5, β=0.85
IONIZATION
CORE
Z=100
Z=80
Z=60
Z=40
Z=26
KODAK 2485
2.5
5
7.5
10
25
50
75
100
250
500
750
1000
DISTANCE FROM TRACK, r (μm)

FIGURE 11

The next chapter presents the experimental and data reduction techniques, along with the results obtained from fast film trans-iron Cerenkov detectors that were exposed on high altitude balloon flights.

CHAPTER III

DATA REDUCTION PROCEDURES AND EXPERIMENTAL TECHNIQUES

1. INTRODUCTION

This chapter deals with the experimental techniques used to fly the detectors, process them, scan them, and then measure the events. The methods employed to evaluate the measurements and make error assignments are discussed; followed by an evaluation of the performance of the fast film Cerenkov detectors.

2. EXPERIMENTAL CONSIDERATIONS

A. Balloon Flight Operations

As indicated in Chapter I, the trans-iron cosmic ray detectors are exposed through the use of high altitude balloons. These balloons have become reliable methods of lifting moderately heavy payloads (1000-2000 lbs.) to pressure altitudes of around 2 to 3 milibars ($\sim$ 2.5 gm/cm^2 remaining atmosphere).

The entire ascent requires $\sim$ 2-3 hours, of which the last 10 milibars require $\sim$ 30 minutes. Thus it is possible to record a number of events that have passed through a significantly greater amount of air (in gm/cm^2) than is present at the final float altitude. To disallow these tracks from the analysis, one

provides for a layer of the stack to shift with respect to the rest of the stack, upon reaching float altitude. Then, the criteria for acceptance of an event is that the tracks all align with the shifted stack in the "altitude" position. No shift is required prior to descent on a normal flight, since it only takes a few minutes for the parachute to reach the more dense atmospheric levels.

So far, fast film Cerenkov detectors have been flown as part of trans-iron cosmic ray detector stacks on 4 balloon flights. The parameters of these flights are given in Table 1.

B. Scanning

CREPE II has provided the data discussed in this Chapter. The stack configuration flown on CREPE II is shown in Figure 12. The shifted layer consisted of 5 sheets of 0.01" lexan and was located above the main stack. The shift of 1" relative to the main stack was accomplished by the use of 48 pyrotechnic actuators. All of the actuators functioned properly and the shift occurred without incident. However, since the balloon became a derelict and came down slowly, the shifted layer was only able to eliminate those tracks acquired during the ascent and not those gathered on the much longer descents.

The main stack consisted of 5 sheets of 0.01" thick lexan (and some Cellulose Triacetate), followed by the fast film Cerenkov

detectors, then, 5 more sheets of lexan, a sheet of 200 micron Ilford G5 nuclear emulsion, and finally $\sim$ 40 sheets of lexan.

After the detector was recovered and the stack disassembled, the nuclear emulsion was processed and several layers of the plastic were etched. Then both the emulsions and the plastics were independently scanned for trans-iron candidates. Table 2 lists estimated scanning efficiencies for the various charge and energy regions.

The emulsion scanning was accomplished with low power stereo microscopes. The efficiency of such scanning is a function of both dip angle and energy. The tracks corresponding to slower particles have denser cores and are more easily recognizable than the tracks of relativistic particles. For steep tracks ($\delta \gtrsim 75°$) the scanning efficiency is somewhat less than for flatter tracks because of the difference of the projected size (length) of the track in the microscope field.

The plastics are searched through an ingenious technique.[43] One layer is etched in a manner that causes the pits on each side to connect, forming a hole. The sheet is then fed through an ammonia vapor blueprint machine with some ammonia sensitive paper. The vapor diffuses through the holes and forms spots on the paper. The plastics are then examined under a microscope in the regions of the

TABLE 1

PARAMETERS OF THE BALLOON FLIGHTS

CARRYING FAST FILM CERENKOV DETECTORS

This table lists the parameters of the 4 balloon flights which have carried fast film Cerenkov detectors. Of the 4 flights, only CREPE II has yielded usable data. A detailed account of the flight of CREPE II is contained in Appendix E. The notes appearing on Table 1 are defined here:

a. The fast film Cerenkov detectors were damaged by excessive pressure marking and are unusable.

b. This flight provided the only usable fast film Cerenkov detector data obtained so far. Details of this flight are presented in Appendix E.

c. Only $\sim$ 21 hours of the flight were at altitudes < 4.7 gm/cm^2. The remainder of the flight was at $\gtrsim$ 10 gm/cm^2. The fast film Cerenkov detectors suffered a loss of film speed due to modifications in the detector design and have not yielded any events.

d. This entire gondola was lost at sea on May 27, 1971.

TABLE I

PARAMETERS OF THE BALLOON FLIGHTS CARRYING FAST FILM CERENKOV DETECTORS

NAME	PLACE OF LAUNCH	DATE OF LAUNCH	FLIGHT DURATION	ARRAY AREA	DETECTORS OTHER THAN CERENKOV	# OF Z>50 EVENTS	MEAN VERTICAL CUT-OFF
CREPE I[a]	Palestine, Texas	May 5, 1970	38 hours	$4m^2$	1 200 μm ILFORD G-5 (nuclear emulsion)	4	4.5 GV
CREPE II[b]	Minneapolis, Minnesota	Sept. 4, 1970	14½ days	$23m^2$	1 200 μm ILFORD G-5 $\sim$1.5 gm/cm^2 Lexan plastic	64	1.6 GV
LAPE II[c]	Alamogordo, New Mexico	May 15, 1971	$\sim$3 days	$30m^2$	1 (diluted) 200 μm ILFORD G-5 $\sim$1 gm/cm^2 of assorted plastic	Evaluation Incomplete	6 GV
CREPE III[d]	Palestine, Texas	May 25, 1971	48 hours	$75m^2$	plastic and nuclear emulsion	---	4.5 GV

FIGURE 12

CREPE II STACK CONFIGURATION

The shifted stack consisted of five 0.01" lexan sheets. The main stack had the Cerenkov detector on top with 5 more sheets of 0.01" lexan directly underneath. The 200 μm Ilford G5 nuclear emulsion was next, and finally forty 0.01" lexan sheets. The total stack thickness was $\sim$ 2 gm/cm^2 and the basic module size was 12" x 12".

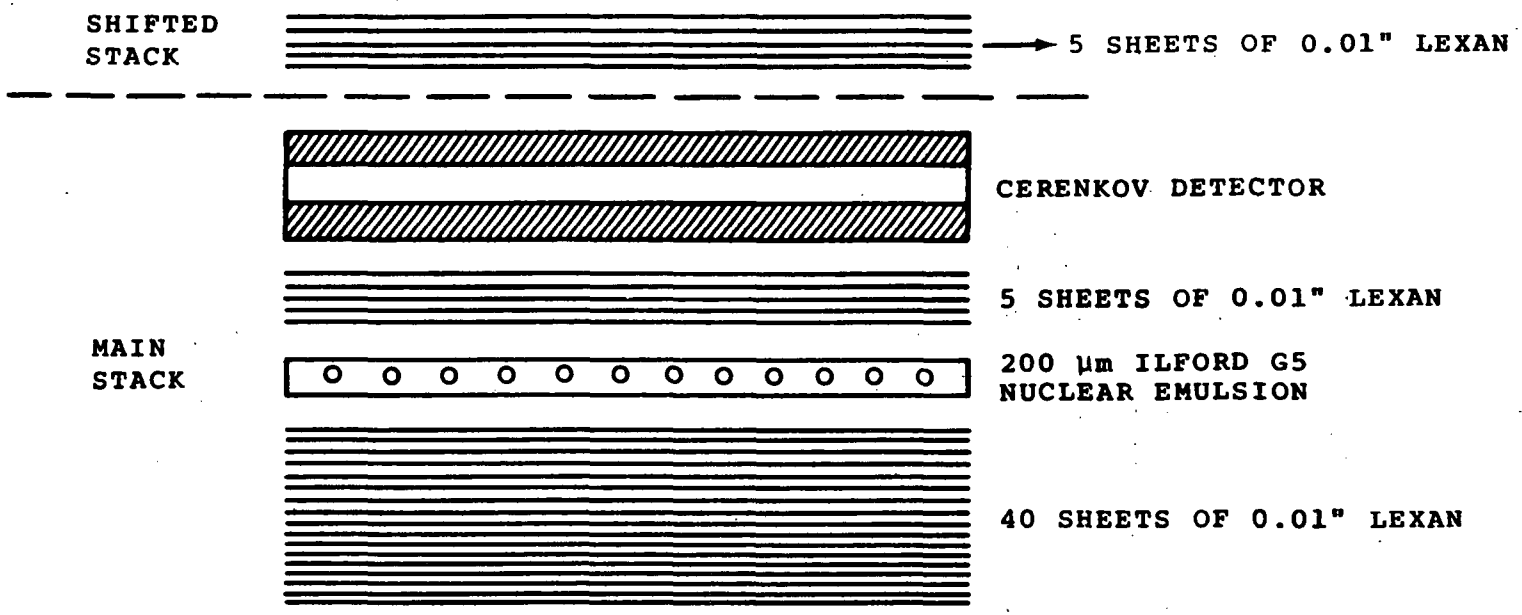
SHIFTED
STACK
5 SHEETS OF 0.01" LEXAN
CERENKOV DETECTOR
5 SHEETS OF 0.01" LEXAN
MAIN
STACK
200 μm ILFORD G5
NUCLEAR EMULSION
40 SHEETS OF 0.01" LEXAN

FIGURE 12

TABLE 2

SCANNING EFFICIENCIES

The scanning efficiencies are broken down by charge and velocity. Due to the small number of events, the values listed are estimates based on selective rescanning and remeasuring. Some events were found and incorrectly identified in one detector layer, and then "rediscovered" in another layer. This has been folded into the estimated limits on the scanning efficiency listed on this table.

TABLE 2

SCANNING EFFICIENCIES

Charge	Velocities		
	Relativistic $\beta > 0.6$	Slowing $0.6 \geq \beta \geq 0.4$	Stopping $\beta < 0.4$
$Z > 80$	$> 90\%$	$\sim 100\%$	$\sim 100\%$
$80 \geq Z > 65$	$> 80\%$	$> 90\%$	$> 90\%$
$65 \geq Z > 50$	$\gtrsim 75\%$	$\gtrsim 80\%$	? 80%
$Z \leq 50$	$\gtrsim 50\%$	?	?

spots. The drawback of this procedure is that relativistic particles etch at a much lower rate than slow particles. As a result, the scanning efficiency is a strong function of velocity, and in fact, relativistic $Z \lesssim 50$ particles are probably not found by this procedure. A further drawback of this method is that it is also a direct function of the dip angle. The flatter the track, the longer the etch path for hole formation. Because of these problems, the plastics are also scanned under stereo microscopes similar to the emulsions. The scanning of the two detectors compliment one another in that the emulsions are better for flat tracks whereas the plastics are best for vertical tracks. The efficiency estimates given in Table 2 represent the combined values for both plastics and emulsions.

C. Event Identification in Fast Film Cerenkov Detectors

Processing of the fast film Cerenkov detectors was begun by stripping the plastic gel from the film in an inert conducting solution (3.0 N $NaNO_3$). The conducting solution precluded any static electric arcing, but the physical act of separation did cause some pressure marking, so a different method of separation was tried. The final procedure adopted was to cut out $\sim$ 6" x 6" squares of the fast film Cerenkov detector, with the candidate events from the emulsion and plastics located approximately in the center. These squares were then mapped with electronic micrometers to obtain total thickness measurements. These measurements would later yield

radiator thicknesses at the event locations. After the mapping, the squares were soaked in acetone to dissolve the radiator and the film was subsequently processed. The film speed was not effected by these procedures (which were, of course, carried out in total darkness). This was verified by reading calibrated step wedges that had been exposed on every tenth film sheet before fabrication.

The lower sheet was then scanned in the location of the emulsion and plastic candidates. Identification was made not only by proper location of the Cerenkov spot, but also by locating the corresponding ionization spot in the upper sheet and verifying the proper dip and azimuthal angles for the event; where the film was undamaged, the fast film Cerenkov detectors have yielded images for all of the obviously fast events with $Z \gtrsim 55$ based on emulsion charge estimates.

The ionization spots were small, as expected ($\sim$ 5 μm in diameter), and there was no evidence of any scintillation, or exposure from the base side in either sheet. Since the ionization spots contain so few grains, very little usable charge or velocity information can be obtained from them. A photomicrograph of a Cerenkov image and it's accompanying upper sheet ionization spot is included in Appendix F.

3. MEASUREMENT AND ANALYSIS OF THE EVENTS

A. Automated Microscope Image Dissector

After an event has been located and identified through the scanning efforts described in the previous section, the Cerenkov image is measured by a device known as an Automated Microscope Image Dissector (AMID).[44] AMID was designed to measure nuclear emulsion tracks, and is in essence a sophisticated precision programmable scanning microdensitometer. It consists of an oil immersion microscope which is viewed by a programmable image dissecting television camera. The image dissector scans a square field that, with a 12x objective, is $\sim$ 540 μm on a side. The scan is not continuous, but rather is composed of 1024 x 1024 individual cells. The image dissector tube can be directed to any of the cells in the field at will, and the integration time that it spends observing a given cell is also programmable. The response of the tube is fixed and the output for each cell, which corresponds to the time integrated light intensity, is an octal level between 0 and 377_8. The absolute noise level is only weakly dependent upon the integration time, and thus one can select a general integration time that will yield a high output to noise ratio, even for very dark fields. For example, if an image is scanned with a cell integration time of 10 μsec, and yields an average cell output level $\sim 100_8$; one can increase the integration time to 30 μsec, which will then raise the average cell output to $\sim 300_8$. Since the noise is approximately independent

of the integration time ($\sim \pm 3_8$ in most cases), the signal to noise ratio will be considerably improved. The tube is calibrated for variations in sensitivity across the field, by scanning a blank field through the microscope optics; and then programming slight changes in the individual cell integration times to correct for any nonuniformities discovered. The illumination lamp and the image dissector tube are allowed to stabilize before any measurements are made, and fluctuations are guarded against by selective remeasuring.

For the Cerenkov images, the raw scans are made by selecting every fifth cell forming a regular grid of 205 x 205 cells, which uniformly covers the entire field (i.e., 540 μm x 540 μm). This grid is further reduced by averaging the levels of the 8 cells immediately adjacent to each cell, and then taking every other of these summation cells to form a 102 x 102 grid. Figure 13 depicts this grid structure. Finally, this grid is extracted and placed on magnetic tape for analysis. Thus, the AMID system yields a detailed photographic density map of the Cerenkov image which has been slightly smoothed to remove local nonuniformities.

The resolution obtained with this 102 x 102 grid ($\sim$ 5 μm which is slightly greater than the developed grain size), has proven sufficient to provide all of the required details of the observed images.

FIGURE 13

AMID SCANNING FIELD

a) The basic AMID field consists of 1024 x 1024 cells. For measuring the Cerenkov images, AMID is programmed to scan every fifth cell forming a 205 x 205 data matrix.

b) The 205 x 205 data matrix is reduced to a 102 x 102 data matrix for final analysis by averaging the levels of the 8 points adjacent to every other of the 205 x 205 data matrix points. This provides first order smoothing as well as a factor of 4 reduction in the size of the final data matrix. In the averaging of the 9 adjacent points, the center point is given full weight, the laterally adjacent points ½ weight, and the diagonally adjacent points ¼ weight. Thus in the final 102 x 102 matrix, each of the original 205 x 205 points has the same weight.

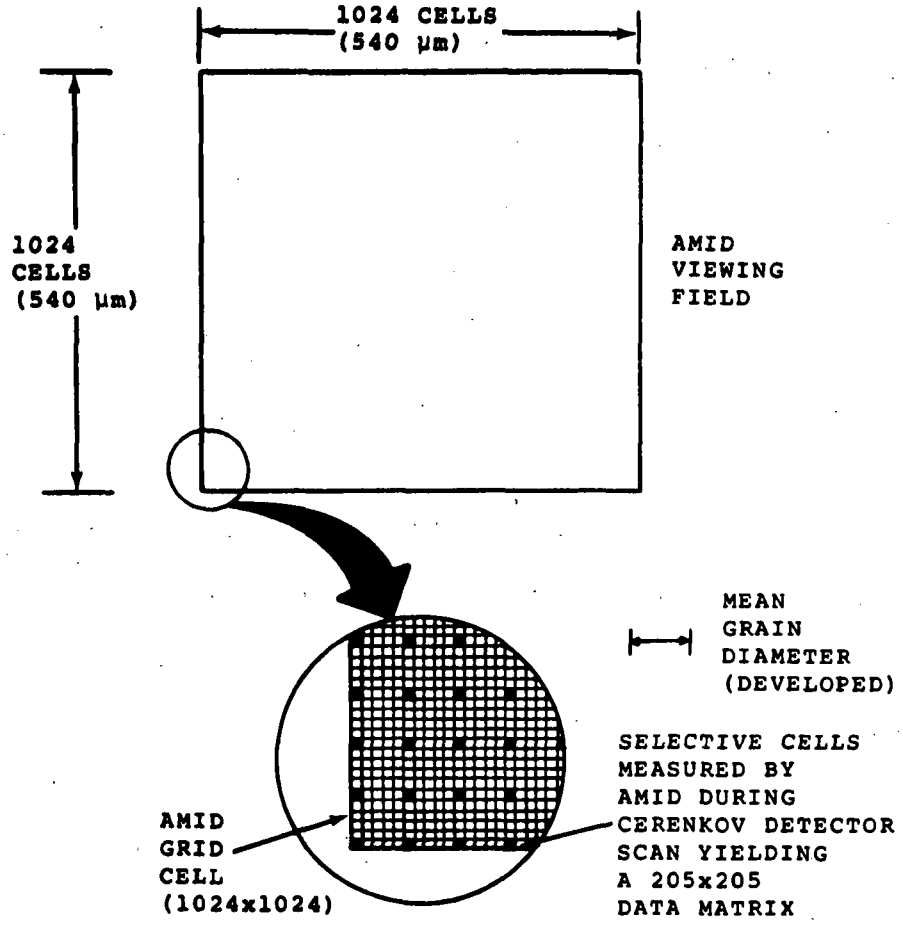

a. SELECTIVE CELLS SCANNED

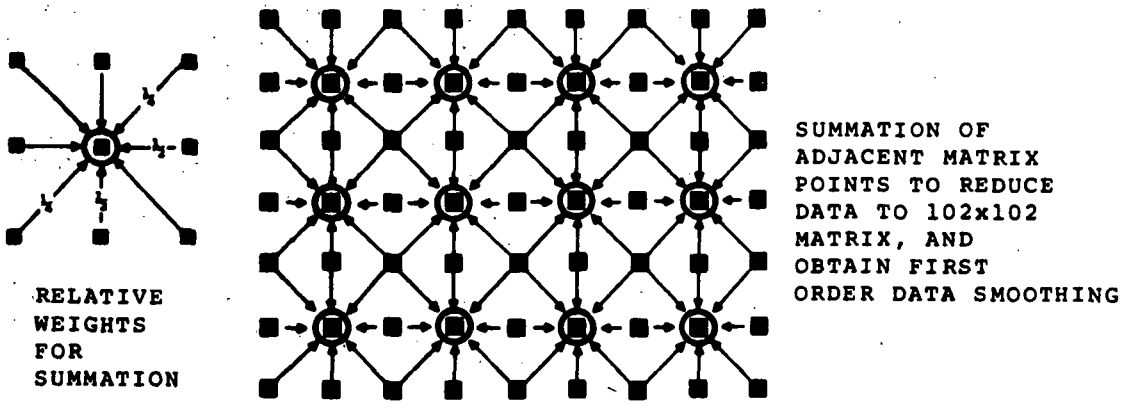

b. FIRST ORDER SMOOTHING

FIGURE 13

B. Analysis of the Images

As pointed out in Chapter II, the edge of the photographic image will be determined by one of two limits. If the film is sufficiently sensitive, the edge of the observed image will be the edge of the actual conic section. However, if the Cerenkov photon density at some places along the conic section edge is below the film sensitivity threshold, then at those places the observable image edge will be an iso-density curve, and the resulting shape will be the composite of the two curves, which is given by equation (30). We wish to find the theoretical shape that best fits the observed image edge.

The analysis of the image loaded on tape by AMID then proceeds in the following manner:

1. The 102 x 102 grid is scanned for the center of the image by finding the region of maximum photographic density, (relative photographic density $\propto$ log (1/AMID level)). Because of the films' saturation characteristics, it is not possible to directly locate the track impact point. Rather, this step provides the approximate region in which the track impact point is located. This step also provides a photographic density level which is clearly internal to the image, from which one can begin the search for the image edge.

2. The search for the image edge is begun by forming concentric rings of successively lighter photographic density about the central dense region located in the previous step.

These rings are formed in a manner such that each ring contains $\sim$ 100 grid points. Figure 14 demonstrates this ring formation for a typical event. After each ring is formed, the points are broken down by octants, and the radial deviation from the mean, S_j, is calculated for each octant (i.e., j = 1, 8):

$$S_j^2 = \sum_{i=1}^{n_j} \frac{(f_i - m_i)}{n_j} \quad , \tag{32}$$

where n_j is the number of points contained in the j^{th} octant, f_j is the radius of the i^{th} point, measured from the center of the region located in Step 1, and m_j is the mean radius for all of the points in the j^{th} octant. In the ideal case, S_j will be $\sim$ 0, only if the image is a circle. However, the total combined deviation for the entire ring:

$$S = \left(\sum_{j=1}^{8} S_j^2 \right)^{\frac{1}{2}} \quad , \tag{33}$$

will, for all shapes change only slightly from ring to ring until the edge is reached. When the edge is reached, S increases in most cases by a factor of > 5 between the last image ring and the first background "ring". For our purposes, the edge is defined as the ring which is followed by an increase in S, by a factor of at least 3. Efforts to discriminate the edge ring in greater detail result in virtually no difference in the final fit described in Step 7 below.

3. At this point, the $\sim$ 100 points from the edge ring, found in Step 2, are examined by eye. Usually, there are a few ($\lesssim$ 20) points which are clearly background. These background points always lie randomly distributed, and clearly outside of the edge ring as shown in Figure 14. Those background points whose radii are > 1.5 times the apparent image radius are removed. If any doubt as to the validity of a point exists, the point is not removed. This step is not required, as these points would be automatically removed in Step 6 or 7 below. The sole purpose of this step is to materially reduce the amount of computing time required to reduce an event.

4. In order to fit the edge ring to one of the curves given by equation (30), we first require a starting guess. If this guess is poor, it is possible to trap the least squares fitting program in a local relative minimum, far from the actual minimum. The variance, V (equation (34) below), is calculated for a 3 dimensional matrix of parameter values. The

FIGURE 14

FORMATION OF CONCENTRIC
RINGS FROM THE DATA MATRIX

This figure demonstrates the method of concentric ring formation from the data matrix obtained by the AMID scan of the image.

a) First, the region of maximum photographic density is located by accepting the matrix points with the lowest 100 levels. The track impact point should be located in this region.

b) This represents one of the typical iso-density rings, concentric to the central region but still interior to the image edge. It contains 75-100 matrix points. An average event will have 15-20 such interior rings before reaching the edge. There is virtually no background for these internal rings.

c) When the edge is reached, background points appear causing a rapid degradation in the dispersion of the points. This shows such an edge ring.

d) Background points are present in increasing proportion in the last few rings, until the ring structure disappears entirely leaving a random distribution of points surrounding a completely void central region, as depicted.

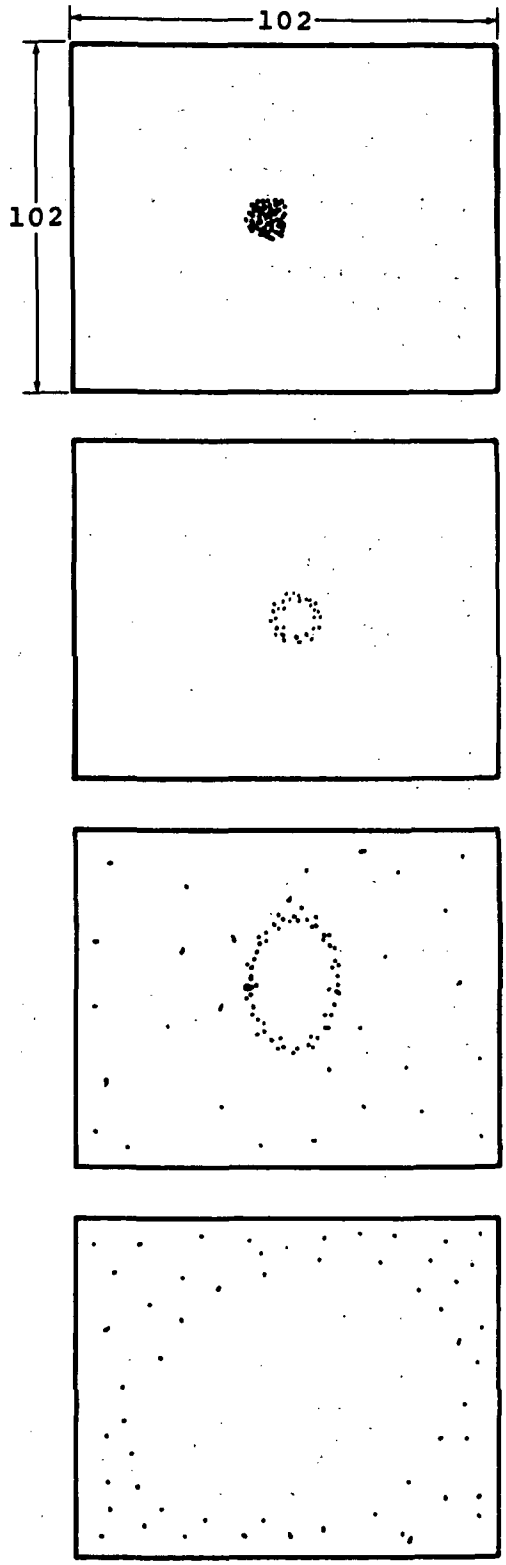
102
102
a. CENTRAL DENSE REGION
b. CONCENTRIC RING INTERIOR TO THE EDGE
C. EDGE RING LEVEL
d. BACKGROUND

FIGURE 14

3 parameters are: 1) θ, the Cerenkov angle, 2) $p/2\pi\rho_c$, as a single parameter from equation (29), where $p=2\pi\alpha Z^2 f_{detector}$ from equation (5), and ρ_c, the photon iso-density, represents the limit of the film's sensitivity in photons/μm^2, and 3) is the location of the track impact point. θ is varied in steps of 0.1 from 0.1 to 0.7; $p/2\pi\rho_c$ is varied in steps of 100 from 50 to 1250; and the location of the track impact point is varied over a 25 point square grid (5 x 5), centered on, and completely covering the central region located in Step 1. V is given by:

$$V = \sum_{i=1}^{n} \frac{(f_i - F_i)^2}{n} \quad , \tag{34}$$

where n is the number of points in the ring, f_i is the i^{th} radius measured from the track impact point, and F_i is the theoretical radius computed from equation (30). The dip angle of the track, δ, and the azimuthal orientation (direction of $\phi'=0$), are both known from the plastics and emulsions, and the radiator thickness, T, is measured as described in Section 2.

5. With the parameters corresponding to the smallest value of V found in Step 4 used as a starting "guess", the data are then subjected to a fitting program which minimizes V.

6. The parameter values found in Step 5 are then used to eliminate data points greater than 4 standard deviations from the calculated image. (The standard deviation $=\sqrt{V}$)

7. The parameters are fitted again and the data further conditioned, this time to 3 standard deviations; and then fit a final time.

8. The errors are assigned by allowing the fitting program to evaluate chi squared in the region of the final minimum. In addition, error estimates are also calculated using the standard form:

$$S_e = \frac{\sum_{i=1}^{n} (f_i - F_i)^2}{n - k} \quad , \tag{35}$$

where k=4, is the number of parameters (the location of the track impact point actually counts as two parameters), and n-k is the number of degrees of freedom. The least square error estimates of equation (35) usually correspond with the empirical chi squared limits found by the minimizing program.

Several dummy data sets were subjected to this analysis and the parameters were generally fit within the error limits. In addition to the edge ring, several of the outer most concentric rings may also be fit by this process. However, the errors from these internal fits tend to be greater than those from the edge fits, and the number of usable rings is small, due to saturation in the film response.

4. RESULTS FROM CREPE II

The scanning of the nuclear emulsions and the plastics flown on CREPE II yielded 64 events with $Z > 50$. These events are listed in Table 3 in order of decreasing charge estimate (as assigned by the plastic).[45] Also included in Table 3 are, 1) β_p at the detector, as determined from the change in radiation damage rate in the plastic, 2) δ, the dip angle of the track as measured in the plastic, 3) β_{ffCd} (or limits on β) for those 27 events where the fast film Cerenkov detector was used to evaluate the velocity, and 4) E_{top}, the kinetic energy at the top of the atmosphere (in MeV/nuc), calculated as described in Chapter IV. For 18 of the events in Table 3, the emulsion and plastic measurements are not yet complete, and only limits on the charge and velocity have been listed. Therefore, subsequent discussions of the emulsion and plastic data will be confined to an evaluation of the 46 events, for which final

TABLE 3

CREPE II Z>50 DATA

This table lists the CREPE II Z>50 data in order of decreasing charge estimate as assigned by the plastic track detectors. Also included is the value of β assigned based on the emulsion and plastic range measurements from the CREPE II stack. The results from the fast film Cerenkov detectors are listed along with the dip angle of the track, and the kinetic energy per nucleon at the top of the atmosphere (as discussed in Chapter IV). The notes listed on the table are given here:

a. The kinetic energy corrections were computed for 3.0 gm/cm^2 of residual atmosphere.

b. The fast film Cerenkov detector was damaged in processing and no event was discernible in the detector.

c. The fast film Cerenkov detector was damaged in flight and was unusable.

d. The fast film Cerenkov detector was not processed because the event was not found before the radiator thickness measuring equipment was dissassembled. Further, by the time the event was identified, the film was unusable at the speed required.

e. Possible ionization spots located in both sheets but no Cerenkov image.

f. No event found in the fast film Cerenkov detector.

g. This event missed the fast film Cerenkov detector.

* This event <u>was not</u> included in the charge data evaluation

† This event <u>was</u> included in the compilation of the energy spectrum for $600 \leq E \leq 1400$ MeV/nuc.

TABLE 3

CREPE II Z>50 DATA

	Z From plastic track detector measurements	β_p At the detector from plastic and emulsion range measurements	β_{ffCd} At the detector from fast film cerenkov detector analysis	δ Dip angle of the track in degrees	E_{top} [a] Kinetic energy at the top of the atmosphere MeV/nuc	
1.	91±1	> .9	b	38	>1500	
2.	90±3	.70±.01	.720+.013-.010	36	810±50	†
3.	82±5	.74±.04	c	57	762±80	†
4.	80±8	.76±.05	.701±011	51	716±30	†
5.	80±3	.56±.01	<.68	90	501±30	
6.	80±1	>.9	d	57	>1500	
7.	79±1	>.9	g	63	>1500	
8.	78±2	.81±.025	b	43	986±66	†
9.	77±2	.84±.015	d	70	1009±65	†
10.	76+6-4	.89+.03-.04	b	62	1346+425-236	†
11.	76+3-2	.85+.035-.025	b	57	1087+182-96	†
12.	76±2	.79±.01	.829±.011	33	969±46	†
13.	76±2	.92±.03	b	63	1669+388-324	
14.	74±6	.72+.04-.05	.741+.028-.022	50	726±74	†
15.	73±1	>.9	b	64	>1500	
16.	70±4	.75±.01	b	38	824±66	†
17.	70±1	.78±.01	d	36	909±51	†
18.	69±4	0.0	b	38	516±20	
19.	69±2	.87±.02	d	72	1153±163	†
20.	69±2	.78±.02	b	43	856±45	†
21.	69±1	.70±.03	<.68	42	711±36	†

TABLE 3 (CONTINUED)

	Z From plastic track detector measurements	β_p At the detector from plastic and emulsion range measurements	β_{ffCd} At the detector from fast film cerenkov detector analysis	δ Dip angle of the track in degrees	E_{top}[a] Kinetic energy at the top of the atmosphere MeV/nuc	
22.	68±7	.70±.03	<.68	66	630±36	†
23.	67±2	.81±.03	b	67	885±93	†
24.	66±2	.79±.04	d	72	796+125-66	†
25.	66±6	.60±.02	<.68	36	633±60	†
26.	66±4	.65±.03	b	30	730±39	†
27.	65±2	.84±.03	b	64	1011±112	†
28.	65±4	.78±.03	d	41	855±90	†
29.	65±3	.60±.05	<.68	48	600±30	†
30.	* >65	>.6	<.68	64	∿650	
31.	64±6	.74±.04	<.68	51	725±65	†
32.	64±6	.64±.035	c	29	722±33	†
33.	63±3	.70±.05	<.68	49	666±67	†
34.	63±2	.63±.04	<.68	36	647±32	†
35.	62+2-1	.85+.03-.01	d	78	1025±158	†
36.	61+4-3	.74±.03	d	45	733±62	†
37.	* >60	>.65	.684±.005	50	632±30	†
38.	* >60	>.75	.793 .005	77	800±20	†
39.	* >60	>.7	.717+.038-.026	74	631±77	†
40.	* >60	>.7	>.95	76	>2000	
41.	* >60	>.75	>.95	82	>2000	
42.	60±4	.69±.02	<.68	81	581±30	
43.	58±5	.63±.03	d	40	601±40	
44.	58±3	.58±.02	<.68	60	483±20	
45.	57±7	.75±.03	e	65	691±50	
46.	56±2	.53±.02	<.68	61	452±20	

TABLE 3 (CONTINUED)

	Z From plastic track detector measurements	β_p At the detector from plastic and emulsion range measurements	β_{ffCd} At the detector from fast film cerenkov detector analysis	δ Dip angle of the track in degrees	E_{top}[a] Kinetic energy at the top of the atmosphere MeV/nuc
47.	55±1	.58±.02	b	78	471±20
48.	55±5	.63±.03	<.68	41	489±20
49.	54±6	.67±.03	f	58	616±50
50.	52±3	.52±.02	f	76	406±20
51.	51±2	.58±.01	f	45	509±20
52.	50±4	.55±.02	f	81	412±30
53.	* >50	>0.7	.810+.123-.075	77	854+1000-190
54.	* >50	>0.6	f	71	---
55.	* >50	>0.5	f	73	---
56.	* >50	>0.5	f	69	---
57.	* >50	>0.5	<.68	50	---
58.	* >50	>0.5	<.68	74	---
59.	* >50	>0.4	b	58	---
60.	* >50	>0.5	b	55	---
61.	* >50	>0.5	<.68	44	---
62.	* >50	>0.5	f	39	---
63.	* >50	>0.5	b	33	---
64.	* >50	>0.5	f	77	---

measurements are available (the excluded events are indicated by an *). Table 4 is a synopsis of the data for the 10 events which had Cerenkov images. There were also 139 trans-iron events with $Z \lesssim 50$ and even though they contained a few relativistic events none of them had a discernable Cerenkov image. An evaluation of the film sensitivity and the measured events yielded an estimate of the usable charge threshold for the fast film Cerenkov detectors of $Z \sim 55$. Further, an examination of the physical limitations discussed in Chapter II, and the observed images, indicates that the velocity threshold for the detectors to be useful is $\beta \sim .68$.

5. EVALUATION OF THE FAST FILM CERENKOV DETECTOR PERFORMANCE

The velocity comparisons of Table 4 generally agree within the error estimates as indicated by the scatter plot in Figure 15. It should be pointed out that the ability of the plastics and emulsions to assign precise velocities for $\beta \gtrsim .68$ is not as good as the fast film Cerenkov detectors (which is reflected by the relative errors). The plastics and the emulsions can however, readily distinguish between slow and relativistic particles. The important feature of Table 4 is that all of the events with Cerenkov images are known from the plastics and emulsions to have $\beta > 0.7$. Further, no definitely fast ($\beta > 0.7$) events with $Z \gtrsim 55$ for which the fast film Cerenkov detectors were usable, have failed to yield Cerenkov images. These results establish the fast film Cerenkov detectors

as a viable method for determining the velocities of $Z \gtrsim 55$, $\beta \gtrsim 0.68$ particles.

The fast film Cerenkov detectors are not, however, very accurate charge measuring devices at present. The values and confidence limits for the parameter $p/2\pi\rho_c$ are also listed in Table 4. The uncertainty in photometry makes the estimate of $\rho_c \sim \pm 20\%$. As such, the uncertainty in the charge assignments by the fast film Cerenkov detectors are at least ± 20%. Figure 16 is a plot of $\sqrt{p/2\pi\rho_c}$ vs. Z for the events in Table 4.

The next Chapter deals with astrophysical corrections to the data.

TABLE 4

SYNOPSIS OF THE EVENTS WITH CERENKOV IMAGES

This table lists the 10 events from Table 3 which had Cerenkov images, and in addition to the information contained in Table 3, the value of θ, $p/2\pi\rho_c$, and the actual maximum and minimum limits on β from the fast film Cerenkov detectors have been included.

TABLE 4

SYNOPSIS OF THE EVENTS WITH CERENKOV IMAGES

Table 3 event	Z_p	β_p	Cerenkov angle θ (rad)	$p/2\pi\rho_c$	β_{ffCd}	Upper limit on β	Lower limit on β	δ	E_{top} (MeV/nuc)
2	90±3	.70±.01	.359±.045	2245±521	.720	.733	.708	36^o	844±20
4	80±8	.76±.05	.279±.031	1937±270	.701	.712	.690	51^o	716±30
12	76±2	.79±.01	.622±.019	310±20	.829	.841	.818	34^o	1075±50
14	74±6	.72+.04-.05	.429±.075	568±283	.741	.769	.718	50^o	737±60
37	>60	>.65	.171±.043	791±466	.684	.689	.679	50^o	632±30
38	>60	>.75	.556±.010	214±81	.793	.798	.788	77^o	800±20
39	>60	>.7	.348±.123	409±117	.717	.756	.691	74^o	631±77
40	>60	>.7	$\gtrsim$.73	---	>.95	1.00	.95	76^o	>2000
41	>60	>.75	$\gtrsim$.73	---	>.95	1.00	.95	82^o	>2000
53	>50	> .7	.589±.175	236±84	.810	.934	.736	77^o	854^{+1000}_{-190}

FIGURE 15

PLASTIC AND EMULSION VELOCITIES
vs.
CERENKOV DETECTOR VELOCITIES

The velocities assigned by the Cerenkov detector are plotted for those events included in Table 4 versus the velocities assigned by the plastics and emulsions. The errors are indicated for each event. The correlation between the two velocity assignments is very good.

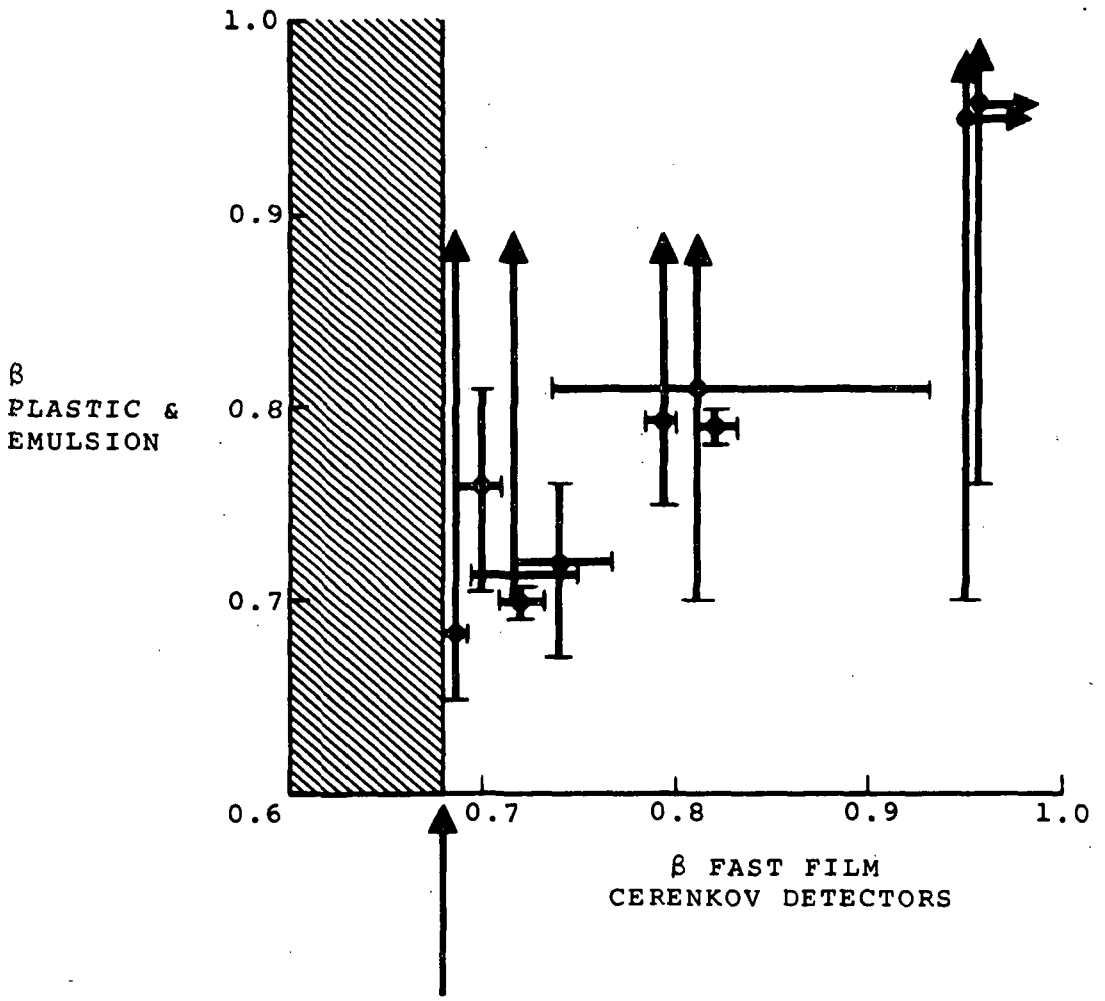
1.0
0.9
0.8
0.7
0.6
β
PLASTIC &
EMULSION
0.6
0.7
0.8
0.9
1.0
β FAST FILM
CERENKOV DETECTORS
CERENKOV DETECTOR
MEASUREMENT
THRESHOLD

FIGURE 15

FIGURE 16

$\sqrt{p/2\pi\rho_c}$ vs. Z_p

Z_p, the charge assignment in the plastic is plotted versus $\sqrt{p/2\pi\rho_c}$ which varies linearly with the charge of the particle. The values plotted are from Table 4, and the errors are indicated by the brackets surrounding each event.

This plot indicates a good correlation between the two measurements but the uncertainties in the fast film Cerenkov detector measurements render them generally unuseful as sensitive charge measuring devices.

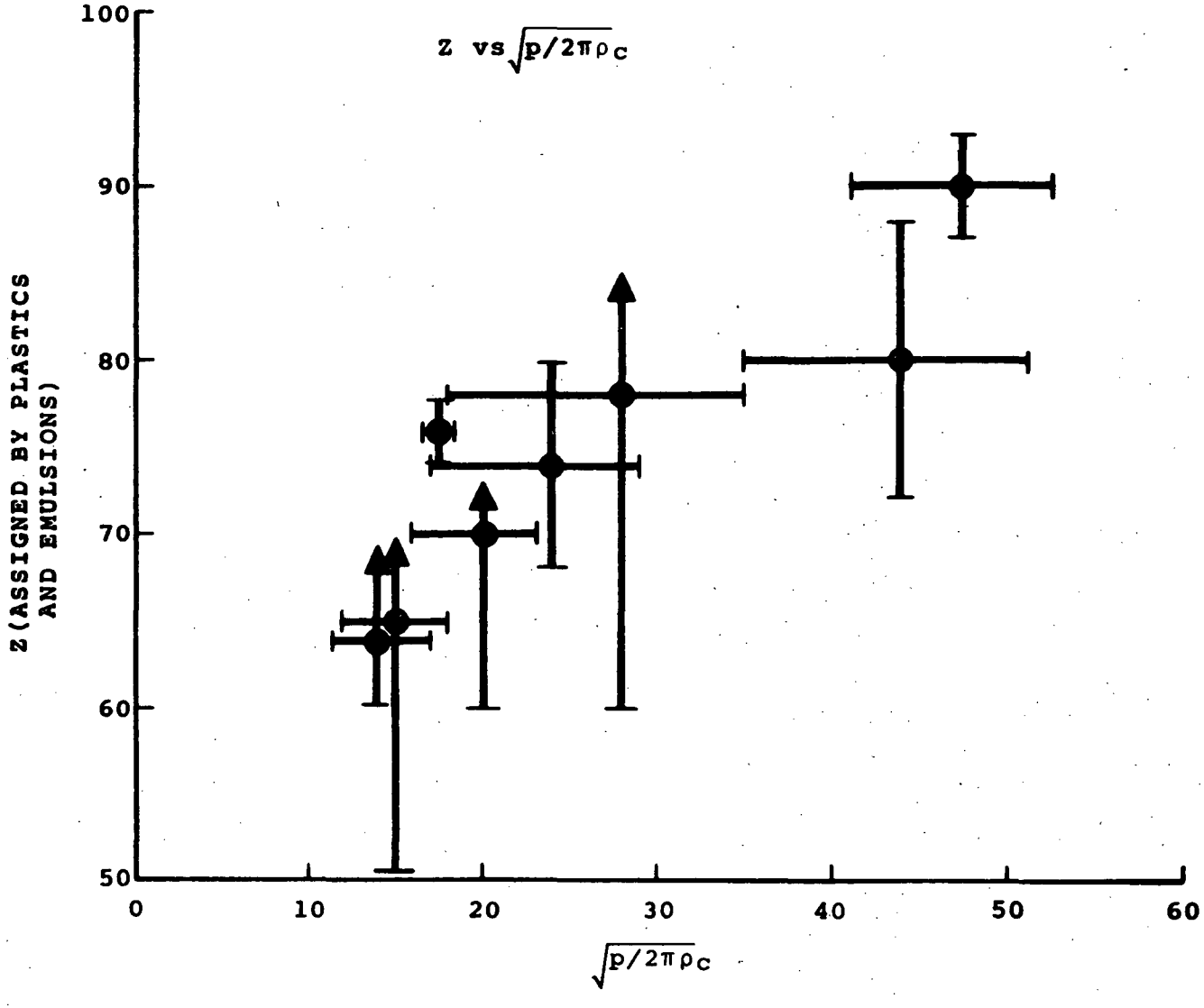
Z vs $\sqrt{p/2\pi\rho_c}$
Z(ASSIGNED BY PLASTICS AND EMULSIONS)
100
90
80
70
60
50
0
10
20
30
40
50
60
$\sqrt{p/2\pi\rho_c}$

FIGURE 16

Page intentionally left blank

CHAPTER IV

CORRECTIONS TO THE DATA

1. INTRODUCTION

Before the data presented in the last chapter can be compared with an interstellar propagation model, they must be corrected for the effects suffered during penetration of the solar cavity, the geomagnetic field, and finally the residual atmosphere that was traversed before reaching the detectors. Since these perturbations occur more or less sequentially, the corrections are applied in the same sequence. The raw data are corrected first to the top of the atmosphere, then to the "edge" of the geomagnetic field, and finally to interstellar space, outside of the solar cavity. After the correction factors are discussed, the corrected CREPE II charge spectrum is compared with the results from previous experiments. The chapter is concluded with a discussion of the trans-iron cosmic ray energy spectrum.

2. CORRECTING THE DATA TO THE TOP OF THE ATMOSPHERE

Correcting the measured fluxes for atmospheric interactions constitutes a small propagation problem by itself. Table 5 lists the mean free path in air (and also in interstellar hydrogen) for

TABLE 5

INTERACTION MEAN FREE PATH LENGTHS

This table lists the interaction mean free path lengths in gm/cm^2 for several primary charge values. The values for both air and hydrogen are given.

TABLE 5

INTERACTION MEAN FREE PATH LENGTHS (IN gm/cm^2)

	Primary Charge						
	26	40	50	60	70	80	90
Air	11.70	8.83	7.63	6.77	6.06	5.54	5.06
Interstellar Hydrogen	1.58	1.08	0.09	0.77	0.67	0.60	0.54

Fe, and several trans-iron nuclei. The total (inelastic) interaction cross section is given by;[46]

$$\sigma_{int} = 49.8\ (A^{\cdot 38} + A'^{\cdot 38} - 1)^2 \text{ mb} \quad , \tag{36}$$

where A is the nucleon number of the primary, and for air, A' = 14.7 (the mean atomic weight of air). Equation (36) is just an extension of the nucleon-nucleus interaction cross section:[47]

$$\sigma_{int} = 49.8\ A^{\cdot 76} \text{ mb} \quad . \tag{37}$$

One finds the mean free path length in gm/cm^2 by substituting equation (36) in the expression:

$$\lambda_{int} = \frac{1674A'}{\sigma_{int}(\text{mb})} \quad . \tag{38}$$

Since the flight altitude was between 2-4 gm/cm^2, the decrease in flux due to the passage through air of primary $Z \gtrsim 50$ nuclei is considerable. Because the dip angles are known, one can compute the exact path length in air, and thus apply a correction for atmospheric attenuation to each event. Here, we are treating each event as part of a flux of particles with the same initial parameters. In this manner, one can speak of the "mean free path length", and compute a meaningful average correction. The path length in air, X_{air}, as a function of the dip angle, δ and the vertical depth X_v, is given by the "flat-earth approximation" which is valid for all dip angles likely to be of interest:

$$X_{air} = \frac{x_v}{\sin\delta} \quad , \tag{39}$$

The resulting factor to be applied to each event is of the form:

$$f_{air} = \exp(X_{air}/\lambda_{int}) \quad . \tag{40}$$

f_{air} accounts for the interaction losses in the atmosphere, but there still remains the problem of enhancement of lower Z particles due to the spallation of heavier particles. Unfortunately, partial cross sections for trans-iron primaries interacting with air have not been measured. The only available estimates are those calculated from the semi-empirical formula of Rudstam.[48] This formula has been slightly modified in recent years and yields the approximate cross section for production of A, Z nuclei by spallation of A', Z' nuclei:[49]

$$\sigma_{A'Z',AZ} = \frac{\sigma_{int}\, f_1(A')\, P_\sigma\, d'^{2/3}\, A'^{-3e'/S}}{1.79\left[(\exp(P_\sigma A') - 1)\left(1 - \frac{2e'}{3P_\sigma A'}\right) + \frac{2e'}{3P_\sigma A'}\right]} \times$$

$$\exp(P_\sigma A - R_\sigma(A)\,|Z - Z_p(A)|^{3/2}) \quad , \tag{41}$$

where :

$$f_1(A') = \exp(-gT'hA') \quad , \tag{42}$$

$$R_\sigma(A) = d'A^{-e'} \quad , \tag{43}$$

$$Z_p(A) = SA\ T'A^2 \quad , \tag{44}$$

and $P_\sigma = 0.056$, $d' = 11.8$, $e' = 0.45$, $S = 0.486$, $T' = 1.111138$, $g = 0.25$ and $h = 0.0074$. However, before one can calculate the enhancement of lower Z particles, some estimate of the abundance of heavier contributing primaries must be available. At this point the method adopted is to lump all of the available data into the various charge groups shown in Table 6. Then one can calculate the percentage enhancement of a particular charge group due to the spallation of the primaries in heavier charge groups. Neglecting energy loss, the relative enhancement of charge group i, f_{spal}, is given by:[50]

$$f_{spal} = \int_0^{X_{air}} \exp(-X/\lambda_i) \left[\sum_{j \geq i} \frac{A' \sigma_{ji}}{1674} S_j \int_0^X \exp\left(-X_j \left(\frac{1}{\lambda_j} - \frac{1}{\lambda_i}\right)\right) dX_j \right] dX \quad , \tag{45}$$

where $\sigma_{j,i}$ is calculated with equation (41) by averaging over A', Z' for group j and summing over A, Z for group i. The calculated values of $\sigma_{j,i}$ also are included in Table 6. Since i and j represent groups of nuclei λ_{int} is replaced by $\frac{\lambda_{int}}{1-(\lambda_{int}\, \sigma_{ii}\, A'/1674)}$, and S_i is the ratio of the estimated intensity of group j nuclei divided by the estimated intensity of group i nuclei at the top of the atmosphere. Contributions to a charge group from itself are included. In this case σ_{ij} is, of course, replaced by σ_{ii}.

The final atmospheric corrections needed are those which are to be applied to the measured energy for each event in order to obtain the energy of the primary at the top of the atmosphere. The range of the primary at the detector can be written in an approximate form:

$$R_{Z,A}(E) = \frac{A}{Z^2} R_p(E) \quad , \tag{46}$$

where, R (E) is the range (in gm/cm^2) of a proton with kinetic energy per nucleon, E. R_p (E) has been tabulated by Barkas and Berger;[51] however R_p (E) in air can be approximated for intermediate energies (400 MeV < E < 5000 MeV) in the form:

$$R_p(E) = 0.01163\ E^{3/2}\ gm/cm^2 \quad . \tag{47}$$

The range of the primary at the top of the atmosphere is:

$$R_{Z,A}(E') = R_{Z,A}(E) + X_{air} \quad , \tag{48}$$

where E' is the kinetic energy per nucleon in MeV at the top of the atmosphere. Then, using equations (46) and (47), equation (48) can be solved for E' as a function of E.

$$E' = \left(E^{3/2} + \frac{Z^2\ X_{air}}{0.01163A}\right)^{2/3}\ MeV/nuc \quad . \tag{49}$$

TABLE 6

AVERAGE CROSS SECTIONS (IN mb)
FOR INTERACTIONS IN AIR

This table lists in matrix form the approximate values of the partial cross-sections for the production of an i^{th} group nucleus from the interaction of a j^{th} group nucleus in air, σ'_{ji}, calculated from Rudstam's formula. One computes these group values of σ'_{ji} by averaging for the j^{th} group and summing over the i^{th} group. σ'_{ii} represents the partial inelastic cross-section for production of an i^{th} group nucleus from an i^{th} group nucleus.

TABLE 6

AVERAGE PARTIAL CROSS SECTIONS (IN mb) FOR INTERACTIONS IN AIR

TARGET	96 ≥ Z ≥ 88	84 ≥ Z ≥ 80	79 ≥ Z ≥ 74	73 ≥ Z ≥ 74	59 ≥ Z ≥ 50
96≥Z≥88	300	100	100	200	1200
84≥Z≥80		200	100	100	300
79≥Z≥74			200	200	800
73≥Z≥60				300	800
59≥Z≥50					200

The corrected energy is listed for each event in Table 4 of Chapter II.

Since there is some doubt as to the residual atmospheric profile for CREPE II (as discussed in Section 5 below), it is important to examine the ramifications of using too small a value for X_v in equation (39).

1. From equation (40) one finds that the percentage error in the absolute flux value assigned to a charge i, would be given by $\Delta X/\lambda_i$, where ΔX is the error in the residual atmosphere.

2. Since the percentages from Table 7 for atmospheric enhancement to each group are moderately small; the relative abundances would be slightly incorrect, but the general features would survive.

3. Correction to the top of the atmosphere tends to steepen a given power law energy spectrum. Thus, insufficiently corrected data would possess an energy spectrum that was flatter than the actual primary spectrum.

3. CORRECTIONS FOR THE GEOMAGNETIC FIELD

It was first pointed out by Fermi[52] that since a static magnetic field does no work, Liouville's theorem predicts that the flux density of particles with a given rigidity, reaching some point in a region of space containing such a field, is unchanged by the presence of the field. Thus, if we consider the earth's magnetic field and observations made at some geomagnetic latitude, we have the well known result that all primaries with rigidities below some threshold value, R_c, will be deflected away. Above R_c, there is a penumbral

zone extending up to some value R_p. In this penumbral zone there exist bands of rigidities for which the particles are still deflected away, but all primaries with rigidities above R_p will reach that geomagnetic latitude. Further, the flux density of all the particles with rigidities sufficient to reach that latitude, will be the same as the primary flux density of those rigidities. This threshold rigidity, R_c, is commonly referred to as the "cut-off" rigidity, which has been mentioned previously.

Rigidity, R_m is defined as the momentum of a particle, divided by its charge, and it can be written in the form:

$$R_m = \frac{(W^2 - M^2c^4)^{\frac{1}{2}}}{Z} \text{ MV}, \tag{50}$$

where W is the total energy of the particle in MeV ($W = AE + Mc^2$ where E is the kinetic energy per nucleon) and M is it s total rest mass. Let w be the total energy per nucleon in MeV/nuc, ($w = \frac{W}{A}$), and m_{nuc} be the rest mass per nucleon ($m_{nuc} = \frac{M}{A} \sim 931.1 \text{ MeV}/c^2$).[53] Then,

$$R_m = (\frac{A}{Z}) \ (w^2 - m^2_{nuc}c^4)^{\frac{1}{2}} \text{ MV}, \tag{51}$$

and solving for w,

$$w = ((\frac{Z}{A} R_m)^2 + m^2_{nuc} \ c^4)^{\frac{1}{2}} \text{ MeV}, \tag{52}$$

one obtains an expression for w as a function of R_m. From equation (52), it can be seen that the total energy per nucleon at a given cut-off rigidity is a function of A/Z, and that nuclei with a small A/Z ratio have a higher cut-off total energy per nucleon. Hence, in determining abundance ratios above a given total energy per nucleon, between elements of differing A/Z ratios from data collected on a flight at some fixed cut-off rigidity, one must normalize the individual abundances to some reference A/Z ratio.

To accomplish this normalization, we require an assumption about the form of the energy spectrum. As discussed in Section 6, the data suggest that the integral energy spectrum at the top of the atmosphere can be best approximated by a power law in total energy. The integral energy spectrum with index $-\nu+1$ (where $-\nu$ is the index of the differential power law spectrum), can be written:

$$N_i(>w_c) = K_i \ (A_i w_c)^{-\nu+1} \quad . \tag{53}$$

The data further indicate that ν is $\sim$ 6.5, rather than the value of 2.6 which is accepted for the sub-iron ($Z < 26$) cosmic ray nuclei. For the purposes of calculating the geomagnetic normalization factor, the value of $\nu = 6.5$ has been assumed. The geomagnetic

normalization factor, f_{gm} is given by:

$$f_{gm} = \frac{N_{A=2Z}(>w(R_c))}{N_{A_i,Z_i}(>w(R_c))} \tag{54}$$

Using equations (52) and (53), f_{gm} can be put in the form:

$$f_{gm} = \left(\frac{2Z_i}{A_i}\right)^{-\nu+1} \left[\frac{\left(\frac{R_c}{2}\right)^2 + m_{nuc}^2 c^4}{\left(\frac{Z_i}{A_i} R_c\right)^2 + m_{nuc}^2 c^4} \right]^{\frac{-\nu+1}{2}} , \tag{55}$$

where, for CREPE II, $R_c \sim 1.6$ GV (i.e., 1600 MV).

At any point near the earth's surface, the cut-off rigidity is a function of both the dip and the azimuthal angles. Along the flight path traversed by CREPE II, this dependence varies only slightly for dip angles > 40°, and since $\lesssim$ 20% of the tracks have dip angles < 40°, the correction factor (54) is still a good approximation when applied to the CREPE II data.

4. SOLAR MODULATION EFFECTS

The modulation of the interstellar cosmic ray flux by the solar wind and the accompanying magnetic field has been the subject of extensive investigations over the past few 11 year solar cycles. Parker[54] suggested a model for the modulation of cosmic rays where irregularities in the magnetic field which propagates outward from the sun along with the solar wind, act as scattering centers which the cosmic rays must diffuse through to reach the

earth. Parker did not include the effects of the adiabatic deceleration of cosmic ray particles by the radially diverging solar wind in his original diffusion calculation. The effects of an adiabatic decleration have been recently examined by Goldstein, Ramaty and Fisk[55], and from their calculations one finds that the inclusion of adiabatic deceleration does not significantly alter the correction factor for rigidities greater than 0.5 GV. Thus, in correcting the CREPE II data, the effects of adiabatic acceleration will be ignored. Silberberg[56], concluded that for rigidities between 1.5 and 15 GV (the region of interest for CREPE II), the solution of the diffusion equation (neglecting adiabatic deceleration) that best fit the proton and He data, implies a decrease in the interstellar flux by a factor of $\exp\left[-K(t)/R_m\beta\right]$ when observed at the earth (where the coefficient K(t) contains the entire time dependence of the modulation). Bhatia, et. al.,[57] have recently concluded that the $10 < Z < 28$ cosmic ray nuclei appear to be modulated in the same manner. We will therefore assume that the trans-iron nuclei are also modulated in a similar fashion. Thus to obtain the flux in interstellar space, one applies a correction to the data at the top of the atmosphere which is of the form:

$$f_{sol} = \exp(K(t)/R_m\beta) \quad . \tag{56}$$

Using equation (50), f_{sol} can be written:

$$f_{sol} = \exp\left[\frac{K(t)Z}{A}\left(\frac{E}{m_{nuc}c^2} + 1\right)\left[\frac{E}{m_{nuc}c^2}\left(\frac{E}{m_{nuc}c^2} + 2\right)\right]^{-1}\right], \tag{57}$$

K(t) has been evaluated by Rao[58] from the available cosmic ray data. The last solar minimum occurred in 1965, for which Rao assigns K(t) $\sim$ 0.4 GV. (The uncertainty in K(t) at solar minimum is such that values as high as 0.6 GV may be correct.) Based on the data from the previous half cycle (1958 - 1965), K(t) was found to vary by $\sim$ 3.1 GV between maximum and minimum, which implies K(t) $\sim$ 3.5 GV at solar maximum. Figure 17 is Rao's plot of the variation of K(t) as a function of the observed decrease in the Climax, Colorado neutron monitors rates. During the flight of CREPE II, the Climax neutron monitor rate ($\sim$ 3800/hr.) was $\sim$ 13% below the ($\sim$ 4350/hr.) rate at solar minimum. From Figure 17, this implies that K(t) $\sim$ 1.8 GV. If one assumes that K(t) was $\sim$ 0.6 GV at solar minimum, then the corresponding value during the CREPE II flight would have been $\sim$ 2.2 GV. For our purposes we will use the value of K(t) = 1.8 GV to compute the solar modulation corrections.

Table 7 illustrates the relative effects of the various corrections discussed in this chapter, on the abundances contained in the various charge groups.

5. COMPARISONS WITH THE RESULTS OF PREVIOUS FLIGHTS

Chapter 5 deals with astrophysical implications of the data presented above; but before proceeding to these discussions, it is interesting to consider the characteristics of the corrected data from the CREPE II balloon flight, with respect to the corrected data from previous trans-iron balloon flight experiments.

FIGURE 17

SOLAR MODULATION COEFFICIENT
vs.
PERCENT DECREASE IN THE CLIMAX NEUTRON MONITOR RATES

This graph was taken from Rao,[59] and indicates how the solar modulation coefficient, K(t), varies with the decrease in the Climax, Colorado neutron monitor rates from those measured at solar minimum. The rate during CREPE II was $\sim$ 13% below the solar minimum rate and the corresponding value of K(t) is $\sim$ 1.8. The solar modulation correction factor is given by: $f_{sol} = \exp[K(t)/R_m\beta]$.

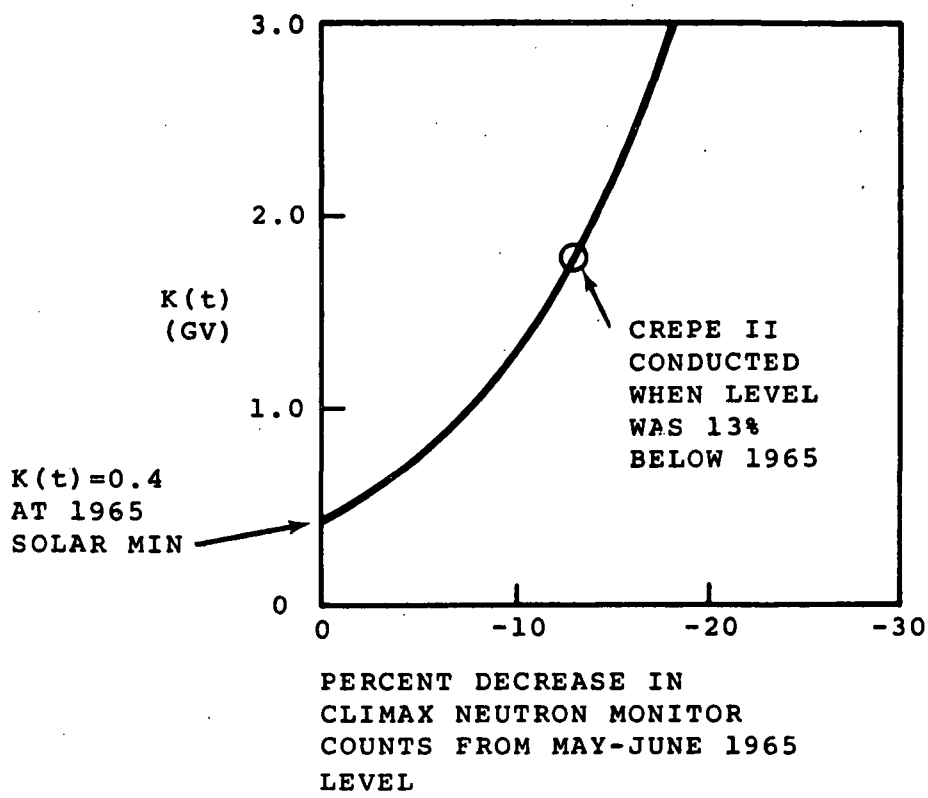
3.0
2.0
1.0
0
K(t)
(GV)
K(t)=0.4
AT 1965
SOLAR MIN
CREPE II
CONDUCTED
WHEN LEVEL
WAS 13%
BELOW 1965
0
-10
-20
-30
PERCENT DECREASE IN
CLIMAX NEUTRON MONITOR
COUNTS FROM MAY-JUNE 1965
LEVEL

FIGURE 17

TABLE 7

RESULTS OF THE CORRECTIONS OF THE DATA

This table presents the results of the atmospheric, geomagnetic, and solar modulation corrections to the CREPE II data. The data have been arranged in various charge groups, and the solar modulation and geomagnetic correction results have been renormalized to the $Z > 84$ group.

TABLE 7

RESULTS OF THE CORRECTIONS OF THE DATA

Charge group	CREPE II events at detector	# of observed events that were probably atmospheric secondaries	# at the top of the atmosphere for different X_v (gm/cm^2)			Outside of the geomagnetic field (renormalized to Z>84 for X_v = 4.0)	Outside of the solar cavity (renormalized to Z>84 for X_v = 4.0)
			3.0	4.0	4.5		
Z>84	2	0	4	5	6	5	5
84≥Z≥80	4	0	8	10	12	10	10
79≥Z≥74	8	<1	15	18	20	16	17
73≥Z≥60	22	6	27	33	37	29	30
59≥Z≥50	10	6	7	8	9	6	6

Figure 18 presents the $Z > 50$ CREPE II charge spectrum in histogram form, by individual charge, corrected to outside of the solar cavity. It is compared with the corrected data from Fowler's 4 balloon flights conducted over Palestine, Texas, ($R_C \sim 4.5$ GV) during the period from 1967 to 1969.[60] The data from a lower geomagnetic cut-off experiment (Sioux Falls, 1969,[61] $R_C \sim 1.75$ GV) is also included. The Sioux Falls detector array had an area of $\sim 4\ m^2$, of which only $\sim 1\ m^2$ has been scanned. This $\sim 1\ m^2$ recorded a total of 5 events with $Z > 50$ after having been flown twice, once at ~ 6 gm/cm^2 of residual atmosphere for 40 hours, and then for another 40 hours at $\sim 3\ gm/cm^2$ of residual atmosphere. This time-altitude profile is very similar to estimated effective time-altitude profile for the CREPE II flight as indicated in Table 1.

The CREPE II data possess two discrepancies when compared to the other results. First, the $58 \geq Z \geq 50$ data from CREPE II is extremely deficient when compared to the Palestine data. This may be explained by the existence of a large number of as yet unmeasured events which have tentatively been assigned charge values of $50 \geq Z \geq 45$. When detailed measurements of these events are completed, it is possible that many of these events will have final charge assignments in the range $58 \geq Z \geq 50$. Due to this deficiency the remaining discussion of the CREPE II data will be confined to the $Z > 60$ events. The second discrepancy is that the $Z \gtrsim 60$ flux from the Sioux Falls flight ($0.088/m^2$ hr), is a factor of ~ 2 greater than the flux from CREPE II ($0.039/m^2$ hr). Similarly, if

one considers only those events from CREPE II which are of a high enough rigidity to be compared with the fluxes from the 4 Texas flights (11 events); the CREPE II fluxes are again a factor of $\gtrsim 2$ too low, even when solar modulation corrections are applied. Finally, the limits for scanning efficiency listed in Table 2 of Chapter II still do not come close to explaining this discrepancy.

To investigate this further, a selective scan of the plastics and emulsions was made to estimate the total number of Fe group events recorded by CREPE II. A partial rescan indicates that the scanning efficiency for the Fe group nuclei was $\sim$ 75%. The estimate of the number of CREPE II iron group events is $\sim 4 \times 10^6$, which is also about a factor of ~ 2 too low when compared with the Texas I-IV data, assuming the Fe differential energy spectrum has an index of -2.6. Clearly, the scanning efficiency is incapable of accounting for this discrepancy.

There are three possible explanations (besides a gross undiscovered scanning inefficiency) for the total flux discrepancy experienced in the CREPE II data.

First, since the balloon became a derelict after 40 hours, the altitude for the remaining portion of the flight can only be estimated. The first 40 hours were at altitudes corresponding to

FIGURE 18

A COMPARISON OF THE CREPE II CHARGE DATA WITH THE RESULTS FROM PREVIOUS EXPERIMENTS

The CREPE II flux, corrected to outside of the solar cavity is compared with the results from Sioux Falls and the Texas I-IV flights. These plots have been rounded off to the nearest whole charge and the solar modulation corrections have been renormalized to the U-group at the top of the atmosphere.

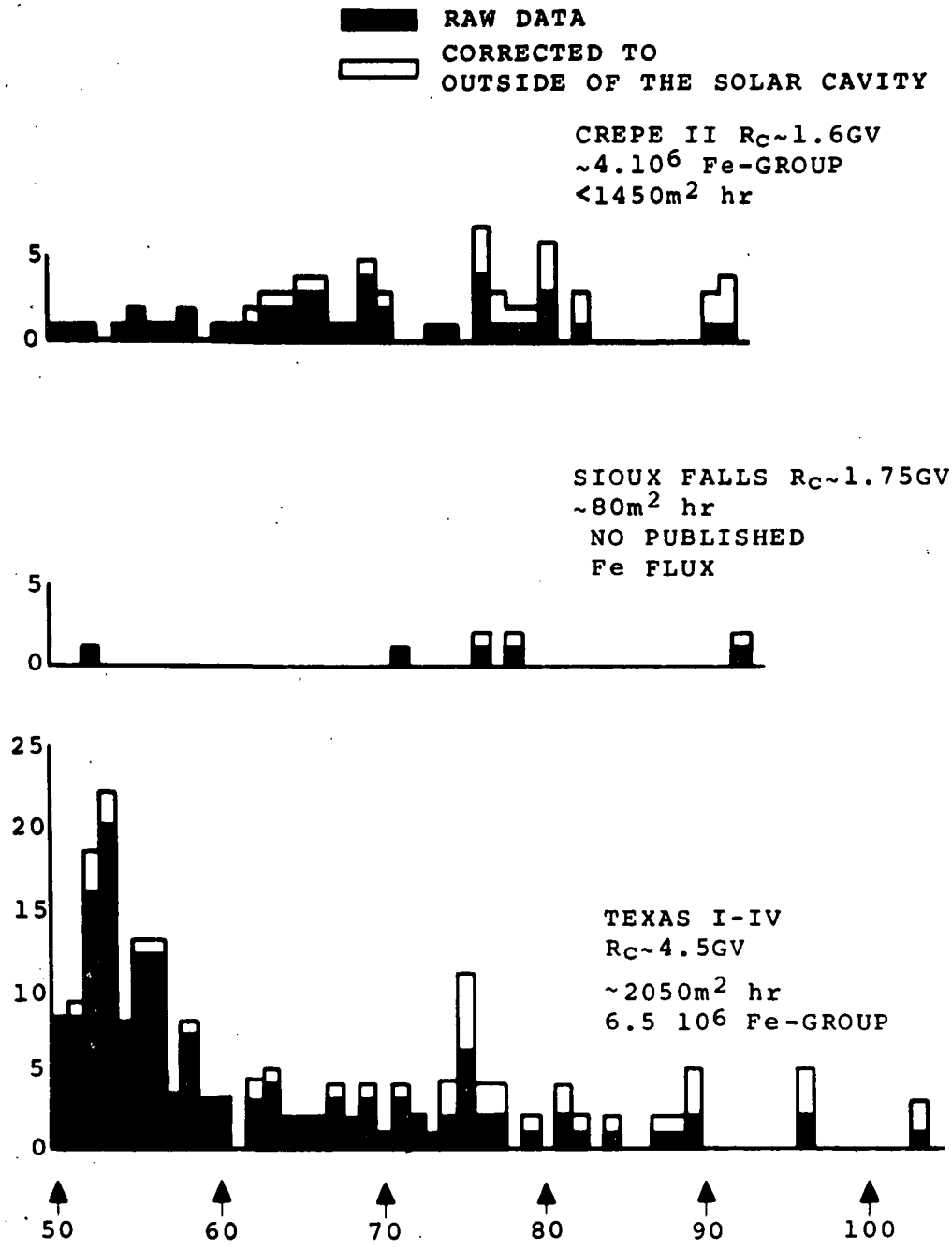
RAW DATA
CORRECTED TO
OUTSIDE OF THE SOLAR CAVITY
CREPE II Rc~1.6GV
~4.10^6 Fe-GROUP
<1450m^2 hr
5
0
SIOUX FALLS Rc~1.75GV
~80m^2 hr
NO PUBLISHED
Fe FLUX
5
0
25
20
15
10
5
0
TEXAS I-IV
Rc~4.5GV
~2050m^2 hr
6.5 10^6 Fe-GROUP
50
60
70
80
90
100

FIGURE 18

$\lesssim$ 2.5 gm/cm^2 of residual atmosphere. It is estimated from visual triangulation and theoretical interpolation that an additional $\sim$ 40 hours at altitudes with less than 6 gm/cm^2 of air remaining, were obtained during the latter 12 days of the 14½ day flight (see Appendix E). If the altitude estimate for this second $\sim$ 40 hours of exposure is grossly incorrect, and the total effective exposure was actually confined to the first $\sim$ 40 hours of the flight; that would then account for almost a factor of 2 discrepancy. If this is the case, then, the atmospheric corrections may have been calculated with too small a value for X_v.

The second possible explanation is a significant increase in solar flare activity. This can cause a corresponding decrease in the primary cosmic ray intensity observed at the earth in addition to normal solar modulation. These Forbush decreases, as they are called, have been known to result in reduction of up to 40% in the local primary cosmic ray intensity. The usual method employed to measure the relative magnitude of the decrease, is to compare the rates reported by the neutron monitors operating around the world. However, no significant variations in the neutron fluxes were observed during the flight of CREPE II, and no other data available suggests that there was any general decrease in the over-all cosmic ray primary flux.

The final possibility is that the decrease experienced by CREPE II was a real feature of the Fe and trans-iron primary cosmic ray flux. The fact that the neutron monitors did not record any variations, implies that the decrease would have to be limited to only Fe group and heavier nuclei. If any lower charges were effected, it would have shown up in the neutron counts. Unfortunately, the background on the emulsions is extreme, due to the slow, 12 day descent. This makes it virtually impossible to obtain valid proton or light nuclei track counts, and as such, a direct verification of a decrease in the Fe and trans-iron flux relative to the lighter nuclear cosmic rays is not available.

Thus, at present, it is not possible to uniquely determine the source of the discrepancy between the CREPE II absolute fluxes and those from previous flights. The validity of the relative abundances from the CREPE II data is not significantly effected by these discrepancies.

These general flux discrepancies in no way change the conclusion of the previous chapter, that the fast film Cerenkov detectors have demonstrated their capability to assign velocities for $\beta \gtrsim 0.68$ and $Z \gtrsim 55$. The next chapter considers possible sources for the trans-iron cosmic ray nuclei, and their propagation through interstellar space.

6. THE TRANS-IRON COSMIC RAY ENERGY SPECTRUM

CREPE II was the first flight with energy resolving capabilities conducted at a low enough geomagnetic cut-off, and with a large enough time-area exposure (as mentioned in the previous section, the Sioux Falls experiment reported only 5 events) to allow an evaluation of the trans-iron cosmic ray energy spectrum.

Figure 19 is a plot of the integral energy spectrum (versus kinetic energy per nucleon) compiled from the CREPE II emulsion, plastic and fast film Cerenkov detector $Z \geq 60$ data, corrected to the top of the atmosphere. The data points based on just the fast film Cerenkov detector measurements, corrected to the top of the atmosphere and normalized to the combined data at 1000 MeV/nuc, are also indicated. A maximum likelihood calculation (the details of which are presented in Appendix C, along with a discussion of the error estimates) indicates that the differential energy spectrum from the CREPE II $Z \geq 60$ data, for kinetic energies between 600 and 1400 MeV/nuc at the top of the atmosphere, is best fit by a power law in total energy with spectral index -6.5 ± 1.7 (i.e., $dN(E) \propto (E + m_{nuc})^{-\nu} dE$, where $\nu = 6.5 \pm 1.7$, and the integral spectrum, $N(>E) \propto (E + m_{nuc})^{-\nu+1}$). The effects of solar modulation on the integral spectrum are indicated by the dotted line in Figure 19, which represents the integral spectrum corrected to outside of the solar cavity. The integral

spectrum corresponding to $\nu = 2.6$, normalized to the CREPE II data at 600 MeV/nuc, is also plotted. From these plots and from the likelihood calculation of Appendix C, it is clear that the $Z > 60$ data recorded during the CREPE II flight, do not agree with the $\nu \sim 2.6$ spectra generally attributed to the sub-iron cosmic rays. This general disagreement with $\nu \sim 2.6$ can be observed from the fast film Cerenkov detector data alone, as indicated by the appropriate error bars in Figure 19. A maximum likelihood calculation based on the fast film Cerenkov detector data for the events with kinetic energies between 600 and 1400 MeV/nuc, yield a value of $\nu \sim 8.8^{+3.9}_{-3.5}$. The likelihood calculations were done with the principle values of the energies at the top of the atmosphere as listed in Table 3. These calculations did not take the uncertainties in these energies into account. The effect of the uncertainties in these energies on the likelihood calculations is discussed in Appendix C.

The significance of these results is deferred to Section 4C of Chapter V. Chapter V discusses the astrophysical implications of the corrected data.

FIGURE 19

Z > 60 INTEGRAL ENERGY SPECTRUM FROM CREPE II

This plot contains the integral energy spectrum at the top of the atmosphere based on the CREPE II Z > 60 emulsion, plastic, and fast film Cerenkov detector data. The results from just the fast film Cerenkov detectors corrected to the top of the atmosphere are also plotted. The spectral index, ν ($N(>E) \propto (E+m_{nuc})^{-\nu+1}$) is $\sim$ 6.5 ± 1.7 from the combined data. This steepens slightly for the kinetic energies between 600 - 1400 MeV/nuc to 7.2 ± 2 outside of the solar cavity. The integral spectrum corresponding to ν = 2.6 is plotted, normalized to the CREPE II data at 600 MeV/nuc. The Z > 60 data from CREPE II including the independent fast film Cerenkov detector data, indicate a general disagreement with $\nu \sim 2.6$.

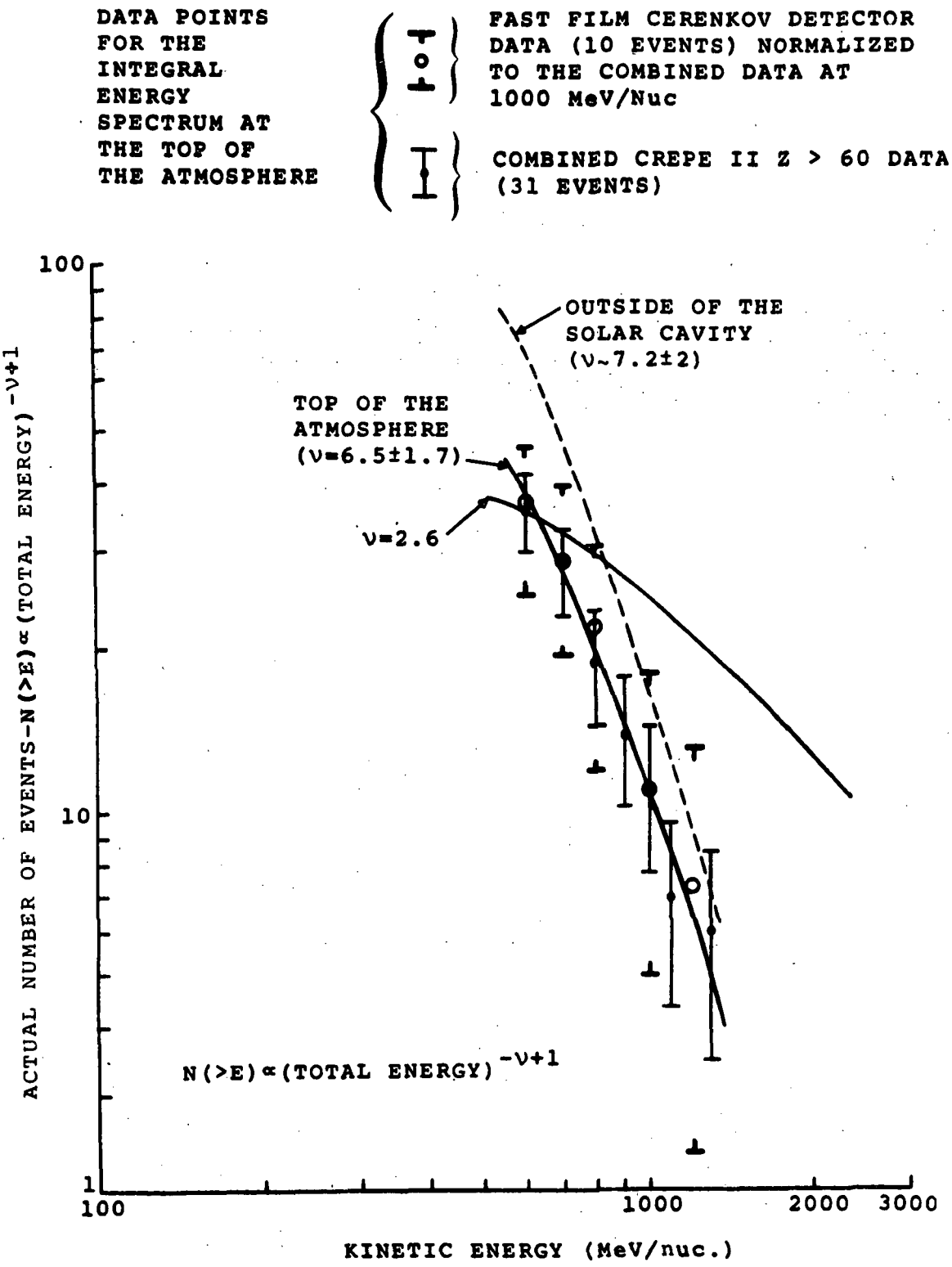
DATA POINTS FOR THE INTEGRAL ENERGY SPECTRUM AT THE TOP OF THE ATMOSPHERE
FAST FILM CERENKOV DETECTOR DATA (10 EVENTS) NORMALIZED TO THE COMBINED DATA AT 1000 MeV/Nuc
COMBINED CREPE II Z > 60 DATA (31 EVENTS)
OUTSIDE OF THE SOLAR CAVITY (ν~7.2±2)
TOP OF THE ATMOSPHERE (ν=6.5±1.7)
ν=2.6
N(>E)∝(TOTAL ENERGY)^-ν+1
ACTUAL NUMBER OF EVENTS-N(>E)∝(TOTAL ENERGY)^-ν+1
100
10
1
100
1000
2000
3000
KINETIC ENERGY (MeV/nuc.)

FIGURE 19

Page intentionally left blank

CHAPTER V

ASTROPHYSICAL IMPLICATIONS OF THE DATA

1. INTRODUCTION

In this chapter, the astrophysical implications of the corrected data will be explored. To begin, we will consider the various possible sources of trans-iron cosmic rays, then proceed to examine the effects that several cosmic ray propagation models have on the abundances characteristic of each of these sources. The data, corrected to outside of the solar cavity as discussed in Chapter IV, will be compared with these calculations, and the astrophysical implications of this will be discussed.

2. POSSIBLE SOURCES OF TRANS-IRON COSMIC RAYS

A. Trans-Iron Nucleosynthesis Processes

There are currently two viable theories of trans-iron nucleosynthesis, and both of these theories require environments which are expected to exist in only a limited number of astrophysical phenomena.

The s-process (s-slow), the first of the two trans-iron nucleosynthesis theories requires that moderate neutron densities $n_n \sim 10^{10}$ neutrons/cm^3 be maintained for long durations ($\sim 10^6$ years), at temperatures of $T_s \sim 1\text{-}2 \times 10^8$ °K, in regions rich in Fe group "seed" nuclei. The seed nuclei (e.g., Fe) absorb neutrons at a slow rate

compared to beta decay times, and thus the s-process proceeds along the chain of beta stability shown in Figure 20. This chain continues up to Z = 83 where the s-process is prevented from climbing any higher by the onset of natural α-decay, and the resulting lack of any long-lived nuclides among the elements with 88 > Z > 83 (trans-Bismuth gap). The most likely source that is able to sustain this s-process nucleosynthesis is found in the interior of the red giant and super giant stars, and these stars are known to undergo mass ejections which could contribute these s-process trans-iron nuclei to the cosmic ray flux. The red giant and super giant contributions will be solely s-process and also predominately low energy at the source, since no obvious acceleration mechanisms are available.

The second theory, known as the r-process (r-rapid), only occurs in an ultra-neutron rich environment ($n_n \sim 10^{20} - 10^{34}$ neutrons/cm^3), and at temperatures of $T_r > 10^9$ °K. In this case, the neutron density is so high, that the neutron rich nuclei do not have sufficient time to beta decay before more neutrons are absorbed. The result is a climb along a path far to the neutron rich side of stability, which continues as long as the neutron density remains high enough. When the neutron density falls, the super neutron rich nuclei beta decay back into the first stable nuclei with the same nucleon number. Typical tracks are depicted in Figure 20.

For the r-process, the proper type of environment is predicted to exist in supernovae and the associated neutron stars. Mechanisms for loss of materials from neutron stars are not yet understood; however, it is clear that during a supernova, vast quantities of matter are expelled from regions which are, or were neutron rich enough to support the r-process nucleosynthesis of trans-iron elements. Further, oscillating electromagnetic fields generated in the immediate vicinity of a neutron star are capable of accelerating the ejected particles to the highest energies observed in cosmic ray primaries at earth.[62] Finally, it should be noted that the pre-supernova phase of stellar evolution is not well understood, and significant quantities of s-process nuclei especially ($Z \lesssim 50$)[63] may be synthesized and ejected into the region immediately surrounding the star, prior to a supernova. Thus, with the possibility of some s-process contamination, we can look to supernovae as the primary source of r-process trans-iron cosmic rays. The specific abundances yielded by the two processes are discussed in Section B.

B. Relative Abundances of r and s Process Sources

Burbidge, Burbidge, Fowler, and Hoyle,[64] presented the first detailed compilation of r-process and s-process abundances. These abundances were subsequently re-evaluated by Seeger, Fowler and Clayton[65] with emphasis on the r-process. The review presented in this section regarding the general r and s-process abundances is based primarily on the work presented in these two references.

FIGURE 20

r AND s - PROCESS NUCLEOSYNTHESIS PATHS

This figure depicts the r and s - process nucleosynthesis paths as originally discussed by Burbidge, Burbidge, Fowler, and Hoyle. The s - process proceeds along the chain of nuclides in the "valley" of β stability. The s - process terminates at Pb ($Z = 82$) because of the onset of natural α - decay for $Z > 83$.

The r - process proceeds along paths far to the neutron rich side of stability with discontinuities at the neutron magic numbers. When the neutron density drops, the neutron rich nuclides along the r - process paths β decay back to a stable configuration as depicted. The r - process is responsible for all of the abundances with $Z > 83$.

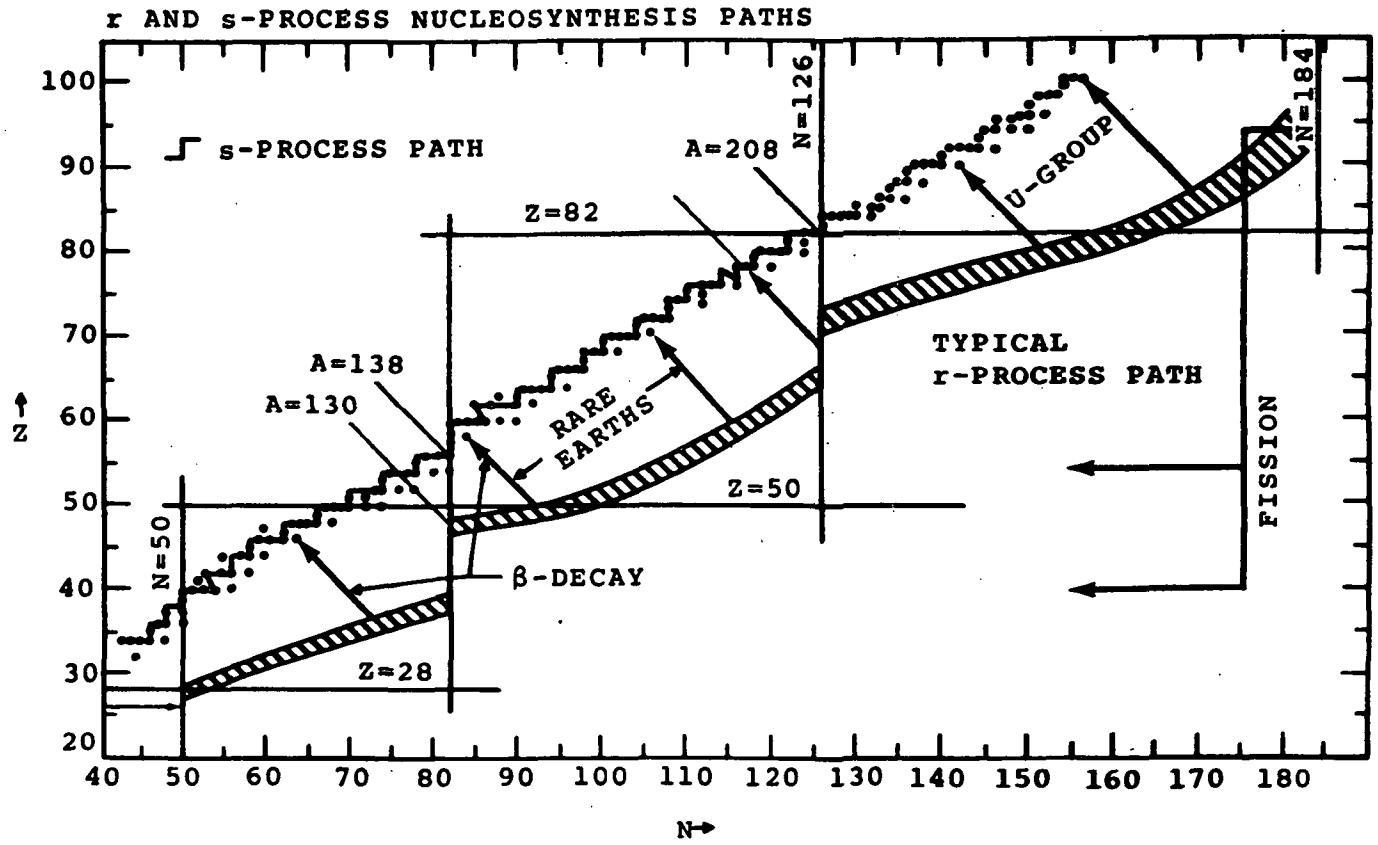
r AND s-PROCESS NUCLEOSYNTHESIS PATHS
s-PROCESS PATH
A=208
N=126
N=184
Z=82
U-GROUP
TYPICAL
r-PROCESS PATH
A=138
A=130
RARE
EARTHS
Z=50
FISSION
N=50
β-DECAY
Z=28
Z
N
100
90
80
70
60
50
40
30
20
40
50
60
70
80
90
100
110
120
130
140
150
160
170
180

FIGURE 20

Figure 21a contains a plot of the s-process relative abundances of Burbidge, Burbidge, Fowler, and Hoyle, which were calculated by evaluating the s-process contributions to the solar system abundances of Suess and Urey.[66] These r-process abundances will be referred to as the "solar system s-process" abundances. They possess a marked odd-even effect, and a characteristic decrease with increasing Z. There is a noticable enhancement around the nuclei with Z or N (neutron number) equal to a magic number (e.g., 50, 82, 126). This enhancement is most dramatic at Pb (doubly magic, Z = 82, N = 126), where the "spike" in the spectrum is known as the Pb-peak. Finally, there are no s-process elements with Z > 83.

The "solar system r-process" relative abundances are shown in Figure 21b. The r-process spectrum possesses three pronounced peaks. The first peak occurs at A $\sim$ 80 (Z $\sim$ 34), and is known as Se-Kr peak. The details of this peak have not been well established due to current uncertainties in the relative contributions to the solar system abundances from these two processes. The second peak at A $\sim$ 130 (Z $\sim$ 52), is due primarily to the r-process isotopic contributions to Te (Z = 52) and Xe (Z = 54), and hence, is known as the Te-Xe peak. The third peak is the most firmly established and is located at A $\sim$ 195 (Z $\sim$ 78). This peak is referred to as the Os-Ir-Pt peak for the three principle elements that comprise it. There may also be a lesser and broader peak at A $\sim$ 164 (Z $\sim$ 67), but this feature has not yet been resolved. Finally, the r-process is

responsible for all of the abundances for $Z > 83$. The region $96 \geq Z \geq 88$ contains all of the long lived nuclides in the $Z > 83$ solar system abundances, and is known as the "U-group".

The relative heights of the three r-process peaks (A_1 = Se-Kr peak, A_2 = Te-Xe peak, and A_3 = Os-Tr-Pe peak) are determined by the temperature and the neutron density present during the nucleosynthesis. If one begins with Fe "seed" nuclei and a neutron density $n_n > 10^{20}$ neutron/cm^3, at some temperature $T_r > 10^9$ °K, then r-process nucleosynthesis will commence, and A_1 and A_2 will be formed first. As A_3 begins to form, A_1 will become partially depleted because the A_1 nuclei will be used as seeds at a greater rate than they are formed. Finally, the U-group elements are populated, and then, in the neutron-rich environment, these nuclei are induced to fission. This fissioning takes place at a rate which doubles the number of nuclei in a characteristic "cycle time", t_2. Seeger, Fowler, and Clayton,[67] have related t_2 to T_r and n_n, as plotted in Figure 22. They also found that if the process continued for a total duration, $\Delta t \geq 2t_2$, the resulting relative abundances were independent of Δt, and were a function of t_2 only. This is reflected in Figure 23, which is a plot of the r-process peak characteristics versus t_2 and Δt. In addition to the relative peak heights for A_1 and A_2, Figure 23 indicates the principle location of the A_3 peak, which also varies with t_2. Longer cycle times shift A_3 toward heavier nuclei and shorter cycle times move the peak toward slightly

FIGURE 21

r AND s - PROCESS SOLAR SYSTEM ABUNDANCES

a. The solar system s - process abundances are plotted (based on Si = 10^6). They possess a charactiustic peak at Pb (Z = 82) and no abundances for $Z \geq 83$.

b. The solar system r - process abundances are plotted (based on Si = 10^6). They exhibit three peaks, labled A_1, A_2, and A_3, and the r - process is responsible for the $Z \geq 83$ abundances. There are no long lived nuclides with $88 > Z > 83$ and this region is known as the "trans-Bismuth gap."

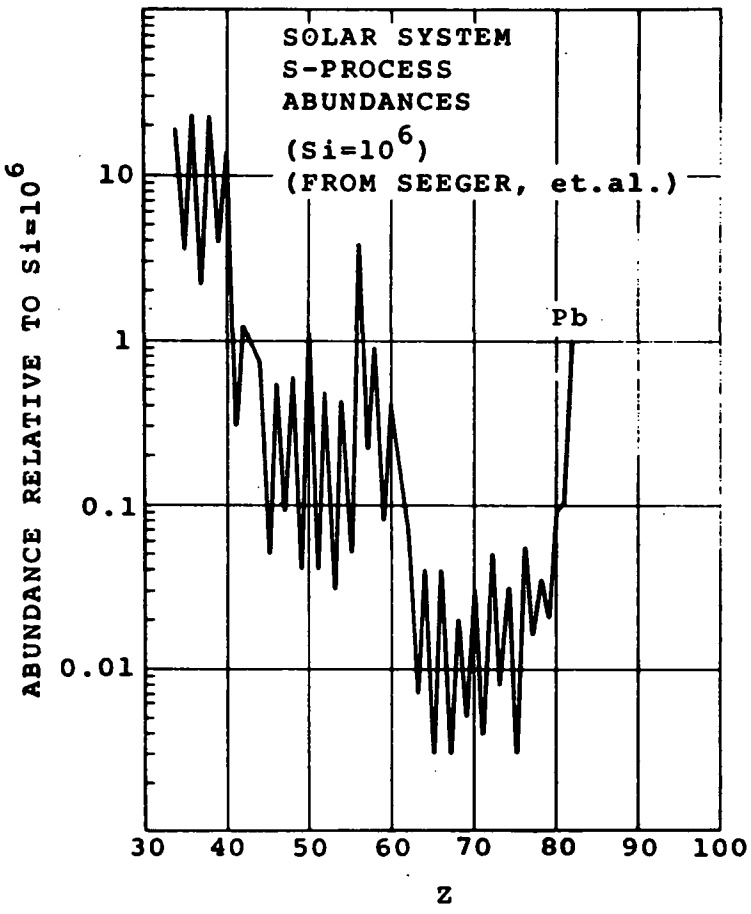
SOLAR SYSTEM
S-PROCESS
ABUNDANCES
(Si=10^6)
(FROM SEEGER, et.al.)
Pb
ABUNDANCE RELATIVE TO Si=10^6
10
1
0.1
0.01
30 40 50 60 70 80 90 100
Z

a.

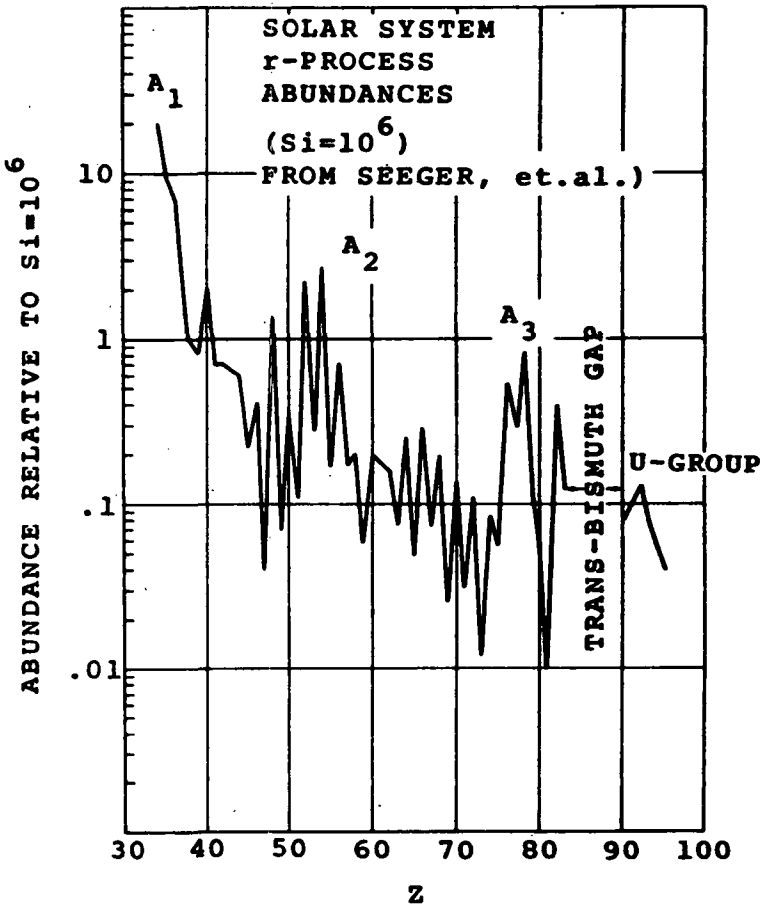
SOLAR SYSTEM
r-PROCESS
ABUNDANCES
(Si=10^6)
FROM SEEGER, et.al.)
A1
A2
A3
TRANS-BISMUTH GAP
U-GROUP
ABUNDANCE RELATIVE TO Si=10^6
10
1
.1
.01
30 40 50 60 70 80 90 100
Z

b.

FIGURE 21

FIGURE 22

CYCLE TIME VERSUS TEMPERATURE AND NEUTRON DENSITY

This plot is from Seeger, Fowler, and Clayton, and represents the cycle time as a function of temperature and neutron density. Temperatures $<<10^9$ ^oK will not support an r-process.

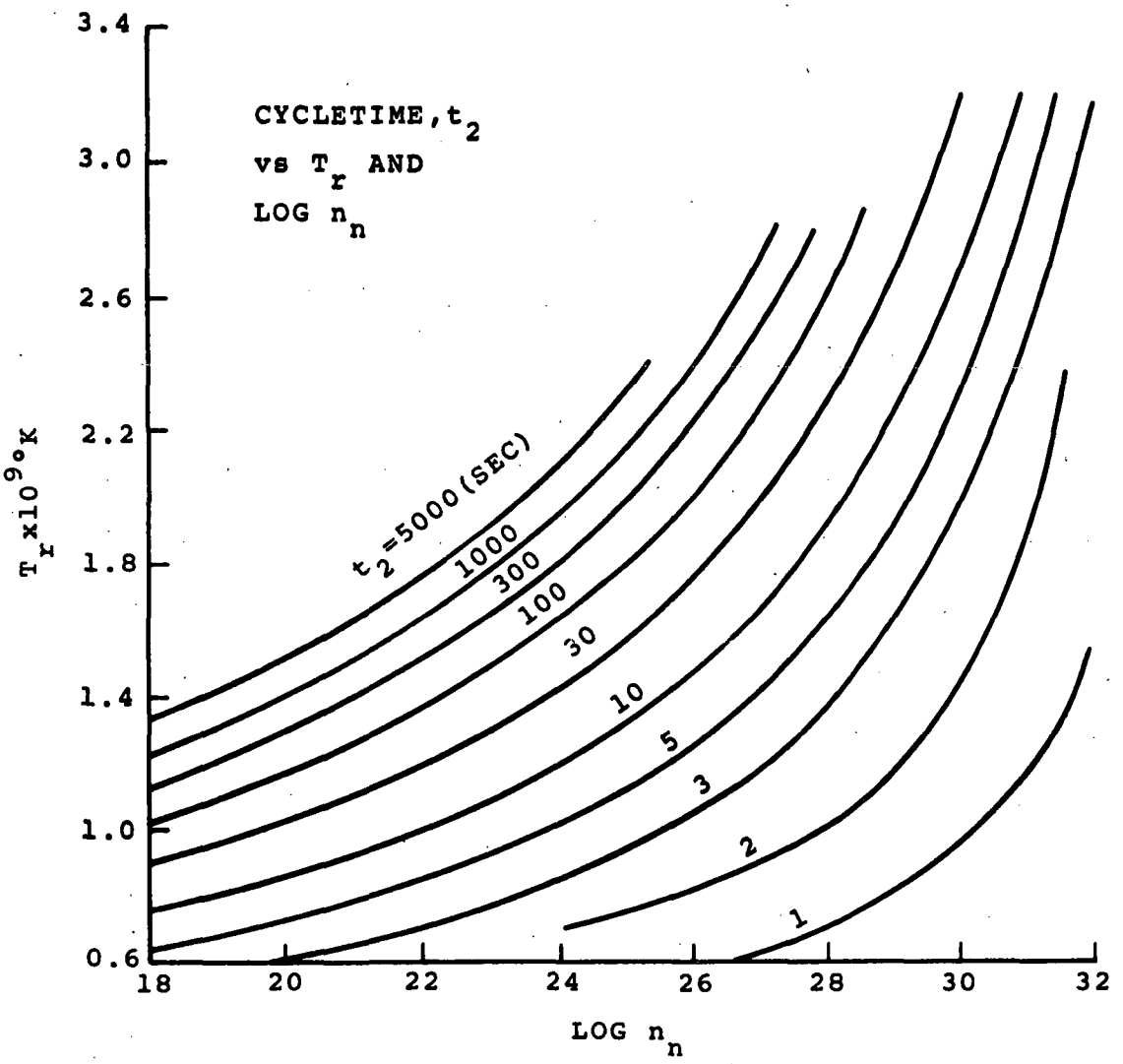
CYCLETIME, t_2
vs T_r AND
LOG n_n
$T_r \times 10^9 °K$
3.4
3.0
2.6
2.2
1.8
1.4
1.0
0.6
t_2=5000(SEC)
1000
300
100
30
10
5
3
2
1
18
20
22
24
26
28
30
32
LOG n_n

FIGURE 22

FIGURE 23

CHARACTERISTICS OF THE r - PROCESS PEAKS VERSUS

THE CYCLE TIME AND THE DURATION

The features of the r - process peaks are independent of duration for durations $\geq$ 2 cycle times. This is indicated by the boundaries of the regions corresponding to different A_1 and A_2 relative peak heights. The location of the A_3 peak is a function of the cycle time as depicted. For an A_3 peak located at Z $\sim$ 76, the corresponding cycle time is $\sim$1 sec.

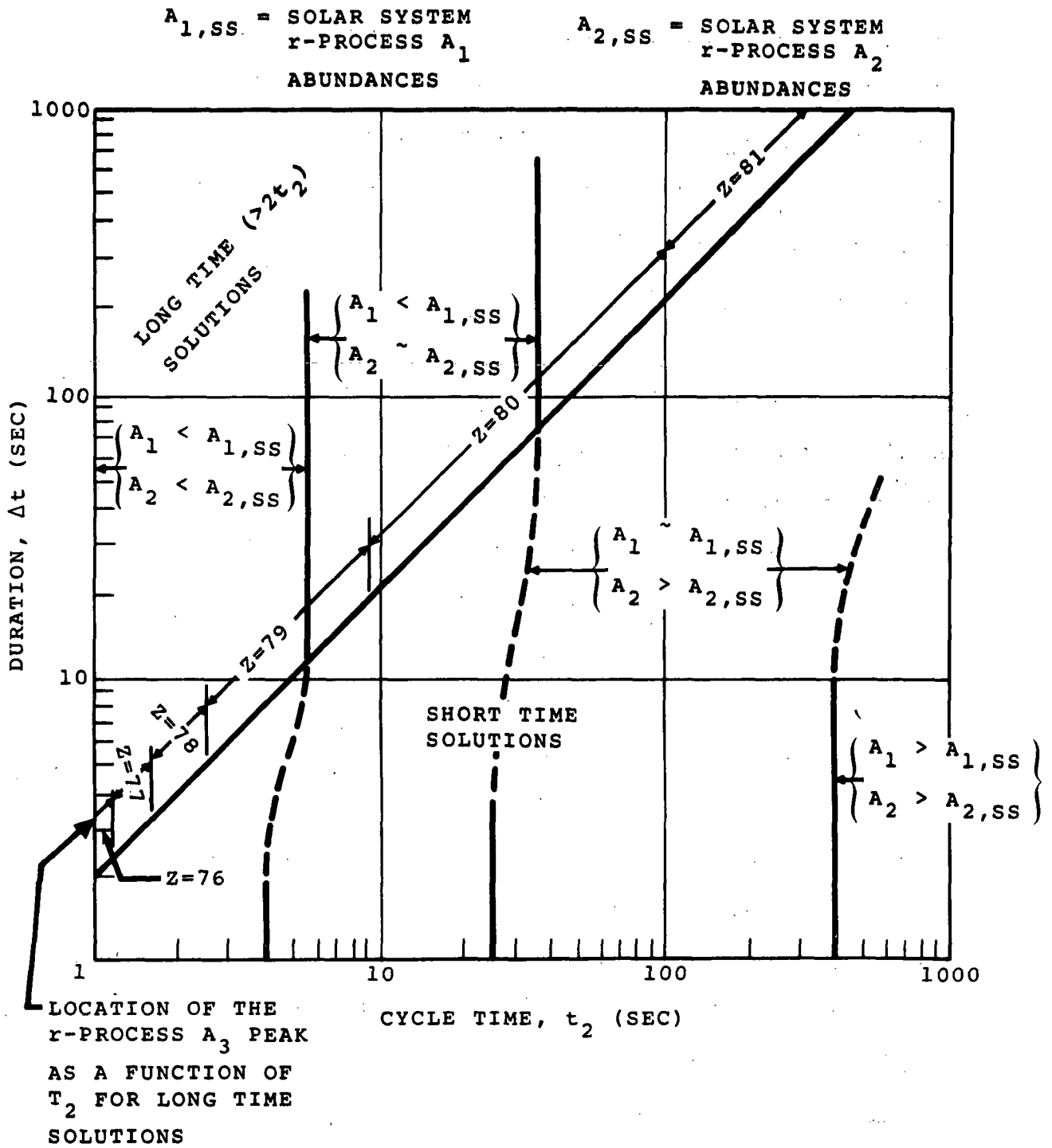
$A_{1,SS}$ = SOLAR SYSTEM r-PROCESS A_1 ABUNDANCES
$A_{2,SS}$ = SOLAR SYSTEM r-PROCESS A_2 ABUNDANCES
1000
100
10
1
DURATION, Δt (SEC)
LONG TIME (>2t2) SOLUTIONS
$A_1 < A_{1,SS}$
$A_2 \sim A_{2,SS}$
$A_1 < A_{1,SS}$
$A_2 < A_{2,SS}$
$A_1 \sim A_{1,SS}$
$A_2 > A_{2,SS}$
SHORT TIME SOLUTIONS
$A_1 > A_{1,SS}$
$A_2 > A_{2,SS}$
Z=81
Z=80
Z=79
Z=78
Z=77
Z=76
1
10
100
1000
CYCLE TIME, t_2 (SEC)
LOCATION OF THE r-PROCESS A_3 PEAK AS A FUNCTION OF T_2 FOR LONG TIME SOLUTIONS

FIGURE 23

lighter nuclei. This makes the location of A_3 a measure of t_2. It is interesting to note that the solar system r-process abundances plotted in Figure 21b do not correspond to a unique value of t_2 in Figure 23. The A_2 location ($Z \sim 78$) implies a $t_2 \sim 8$ second, whereas the A_1 and A_2 peak heights favor a $t_2 \sim 200$ second. This may imply that the contribution to the solar system abundances by r-process nucleosynthesis occurred in two separate events.

The abundance of the U-group relative to the r-process $Z \leq 83$ abundances has not yet been completely determined. The problem lies in the possible effects that the spheroidal deformation of the U-group nuclei may have on the r-process path. The U-group nuclei exhibit relatively large quadrupole moments, indicating that most of the ground states are spheroidal rather than spherical in shape. The r-process solar system abundances plotted in Figure 21b, were calculated assuming that this spheroidal deformation had no effect on the r-process path. Hoyle and Fowler,[68] have shown that the inclusion of spheroidal deformation effects in the calculation of the r-process U-group abundances, can lead to increases of up to a factor of 2, for the U-group abundances plotted in Figure 21b, with respect to the $Z \leq 83$ abundances. It was also shown that the abundances of the individual nuclides within the U-group, relative to each other, were generally unchanged by the inclusion of the spheroidal deformation effect. All references to U-group abundances which include the effects of spheroidal deformation are based on

this work by Hoyle and Fowler[68], and the subsequent paper by Clayton.[69] Thus, we find that the present uncertainty regarding the effect that spheroidal deformation has on the r-process, leads to a considerable latitude in the abundance of the U-group relative to the r-process abundances for $Z \leq 83$.

As a final point on r-process nucleosynthesis, Schramm and Fowler,[70] have examined the possibility that stable superheavy nuclei ($Z \geq 100$) are produced in an r-process environment similar to that which produced the solar system A_3 peak. (i.e., $t_2 \sim 8$ sec., $n_n = 10^{28}$ neutrons/cm^3, $T_r = 1.8 \times 10^9$ °K) They concluded that the most likely candidate with a half life long enough to survive cosmic ray propagation times is Z = 110, A = 184 (half life $\sim 4 \times 10^7$ years). The abundance of this superheavy element resulting from this r-process synthesis would be approximately 6% of that of Uranium.

3. PROPAGATION MODELS

A. Introduction

Assuming that trans-iron cosmic rays are in general ejected from discrete sources such as supernovae or red giants, they must then cross the interstellar distances, passing through, and interacting with the interstellar gas. Thus, when they reach the solar system, some fraction of the original, or primordial particles will

have been eliminated by these interactions, and conversely many of the particles will be surviving fragments from the spallation of heavier primordial nuclei on the interstellar gas. This problem is considerably more complicated than the apparently similar atmospheric correction calculations described in Chapter IV, Section 2. In the case of interstellar propagation, the path lengths are a priori unknown.

The simplest path length approximation is the so called "slab" model, which, as implied by the name, employs a δ-function path length distribution at some "slab" thickness. In the past, attempts were made to explain the observed cosmic ray charge spectrum in terms of a unique slab thickness for all cosmic rays. The slab model was successful in explaining the observed abundance of the L-nuclei (Li, Be, and B) at kinetic energies > 1500 MeV/nucleon, as the fragments resulting from the interaction of heavier M-nuclei (C, N, and O), while passing through a $\sim$ 4 gm/cm^2 slab thickness.[71] However, the slab-model is unable to explain the observed energy dependence of the L/M ratio[72] at kinetic energies below 1500 MeV/nucleon, and this, coupled with other discrepancies, has caused many authors to examine alternative path length distributions. Recently, Shapiro, et. al.,[73] compared various vacuum path length distributions including gaussian, slab, and exponential functions. (The vacuum path length is the path length that would be traversed in the absence of interstellar gas.) They found that

for the cosmic ray data with $Z \geq 26$, the vacuum path length distribution that fit the data best was an exponential of the form e^{-X/λ_e} where λ_e the mean vacuum path length, was ~ 4.34 gm/cm^2.

The slab model will be presented in Section B, and the exponential model will be discussed in Section C.

B. Propagation Calculations

1.) Slab Model

The slab model is similar to the atmospheric correction problem, in that we calculate the effects on a given source spectrum of propagation through a fixed thickness of matter. The diffusion equation for $J_i(E)$, the density of i-type nuclei with kinetic energy per nucleon, E, is given by:[74]

$$\frac{d\,J_i(E,X)}{dX} = -\frac{J_i(E,X)}{\lambda_i} - \frac{J_i(E,X)}{\gamma\rho_H v(E)\tau_i} - \frac{J_i(E,X)}{\lambda_e} + \sum_{j>i}\left(\frac{P_{ji}}{\lambda_j} + \frac{B_{ji}}{\gamma\rho_H v(E)\tau_j}\right)J_j(E,X) - \frac{\partial}{\partial E}\left(J_i(E,X)\left(\frac{dE}{dX}\right)_i\right) \quad , \qquad (58)$$

where λ_i is the mean inelastic interaction length (see Equation (38)), γ is the Lorentz factor, τ_i is the radioactive decay half life for i-type nuclei, $v(E)$ is the velocity of a particle with kinetic energy per nucleon, E, B_{ji} is the radioactive decay branching ratio, and P_{ji} is the fragmentation parameter for the

production of i-type nuclei from j-type nuclei. P_{ji}/λ_j is equivalent to $\frac{N_a}{\rho_H}\sigma_{ji}$, where N_a is the interstellar density in atoms/cm^3, and ρ_H is the mass density of the interstellar gas. For σ_{ji} in mb, $\frac{N_a}{\rho_H} \sim \frac{1}{1674}$, where N_a is taken to be 1 atom/cm^3 and $\rho_H \sim 1.674 \times 10^{-24}$ gm/cm^3 (In addition to H, interstellar gas actually contains $\sim$ 10% He[75] (10% of the number of atoms), however the approximation of pure H causes little uncertainty when compared with the uncertainty in the assumption of $N_a \sim 1$ atom/cm^3).

The first term on the right hand side of equation (58) represents the loss due to interactions in the interstellar gas; similarly, the second term represents the loss due to radioactive decay during propagation, the third term accounts for enhancement in i-type nuclei by fragmentation and radioactive decay of heavier j-type nuclei; and the final term corrects $J_i(E)$ for energy changes, such as ionization losses during the propagation. In this model, kinetic energy changes which occur during interactions are neglected, and only the effects of ionization losses are included.

Due to the experimental data from accelerator runs with protons incident on trans-iron targets, the partial cross-sections, σ_{ji}, for interactions of trans-iron nuclei with Hydrogen are better known than those for interactions with air. Recently, Silberberg and Tsao[76] conducted a very detailed compilation of the data, and used it to perform extensive modifications to Rudstam's original relations. These modifications have yielded the most current and complete values

for the partial cross-sections, and as such, have been used without further modification. These partial cross sections theoretically represent the direct production of i-type nuclei from j-type nuclei. However, it has been assumed that any unstable product nuclei with lifetimes less than 60 sec are included in the cross-section for production of the resulting stable nucleus. Spallation contributions to unstable product nuclei with $\geq$ 60 sec. lifetimes are separately calculated and added to the abundance for the final stable nucleus into which it decays.

If one limits the model by assuming that tertiary and higher interactions do not occur, the solution to equation (58) can be written in the form:

$$J_i(E,X) = J_{i,1}(E,X) + J_{i,2}(E,X) \tag{59}$$

where $J_{i,1}$ represents the surviving source nuclei, and $J_{i,2}$ is the secondary interaction contribution. Using the boundary condition that $J_i(E,0) = J_{i,0}(E)$ (the source abundance), one finds that:[77]

$$J_{i,1}(E,X_0) = f^i_{ion}(E,X_0)\ J_{i,0}(E)\ \exp\left(-X_0\left(\frac{1}{\lambda_i} + \frac{1}{\gamma\rho_H v(E)\tau_i}\right)\right) \tag{60}$$

and,

$$J_{i,2}(E,X_0) = \exp(-X_0(\frac{1}{\lambda_i} + \frac{1}{\gamma\rho_H v(E)\tau_i})) \sum_{j>i}\left(\frac{P_{ji}}{\lambda_j} + \frac{B_{ji}}{\gamma\rho_H v(E)\tau_i}\right)$$

$$J_{i,0}(E) \int_0^{X_0} f^i_{ion}(E,X_0-X_j)\ f^j_{ion}(E,X_j)\ e^{-X_j(\frac{1}{\lambda_j} - \frac{1}{\lambda_i})}\, dX_j. \qquad (61)$$

An expression for the ionization loss correction factor $f_{ion}(E,X)$ which represents the effect of the energy loss term in equation (58), has been derived by Ramaty and Lingenfelter,[78] and further discussed by Gloeckler and Jokipii.[79] In order to obtain a usable function for $f_{ion}(E,X)$, one must make some assumptions regarding the energy loss rate and the energy dependence of the source spectrum. One can approximate the range-kinetic energy relation by:

$$E = K\, R^{\eta}_{Z,A} \quad , \qquad (62)$$

where $R_{Z,A}$, the range in gm/cm^2 of a nucleus with charge Z and mass $m_{nuc}A$, is approximated by $\frac{A}{Z^2} R_p(E)$ (where $R_p(E)$ = the range of a proton with kinetic energy per nucleon, E). For kinetic energies between 400 and 5000 MeV/nuc, this approximation causes E to be in error by less than 5%.[80] As discussed in Chapter IV, the data suggest that, in interstellar space, the differential energy spectrum is best approximated by a power law in total energy per nucleon, w, with spectral index $\sim$ 7.2. For small

changes in the kinetic energy per nucleon, E ($\Delta E << m_{nuc}c^2$), one can approximate a power law in <u>total</u> energy per nucleon with index $-\nu$, by a power law in <u>kinetic</u> energy per nucleon with index $-\frac{\nu E}{E + m_{nuc}}$. The error produced in $J_i(E)$ at 1000 MeV/nuc by this approximation with $\nu \sim 7.2$ is $\lesssim 3\%$, and the relative abundances are even less sensitive. Thus, to calculate $f_{ion}(E,X)$ the energy dependence of the differential energy spectrum is approximated by:

$$J_{i,0}(E) \propto E^{-\left(\frac{\nu E}{E + m_{nuc}}\right)} \tag{63}$$

Using these approximations, f_{ion} reduces to:[81]

$$f^i_{ion}(E,X) = \left(1 + \frac{Z_i^2 X}{A_i R_p(E)}\right)^{-\eta\left(\frac{-\nu E}{E + m_{nuc}} - 1\right) - 1} \tag{64}$$

$R_p(E)$ in Hydrogen gas has been tabulated by Barkas and Berger.[82]

The relative intensity of i-type nuclei predicted to exist at earth by the slab model, $J_{i,slab}$ is given by the sum of $J_{i,1}$ and $J_{i,2}$ from equations (60) and (61). The integral in equation (61) reduces to an incomplete gamma function which can be numerically integrated.

The only parameter that can be varied in the slab model is the slab thickness, $X_{slab} = X_0$. Figure 24 contains plots for Z > 45 of $J_{i,slab}$ at a kinetic energy of 1000 MeV/nuc, calculated for X_{slab} = 0.5, 2.0, and 4.5 gm/cm^2 (only even Z abundances have been plotted in the interest of legibility). For the spectra presented in Figure 24a, the source, $J_{i,0}$, was taken to be the solar system

FIGURE 24

THE RESULTS OF SLAB MODEL PROPAGATION

a. This plot contains the result of slab model propagation through 0.5, 2.0, and 4.5 gm/cm^2, on the solar system s - process abundances (based on Si = 10^6).

b. This plot contains the corresponding results for the solar system r - process abundances.

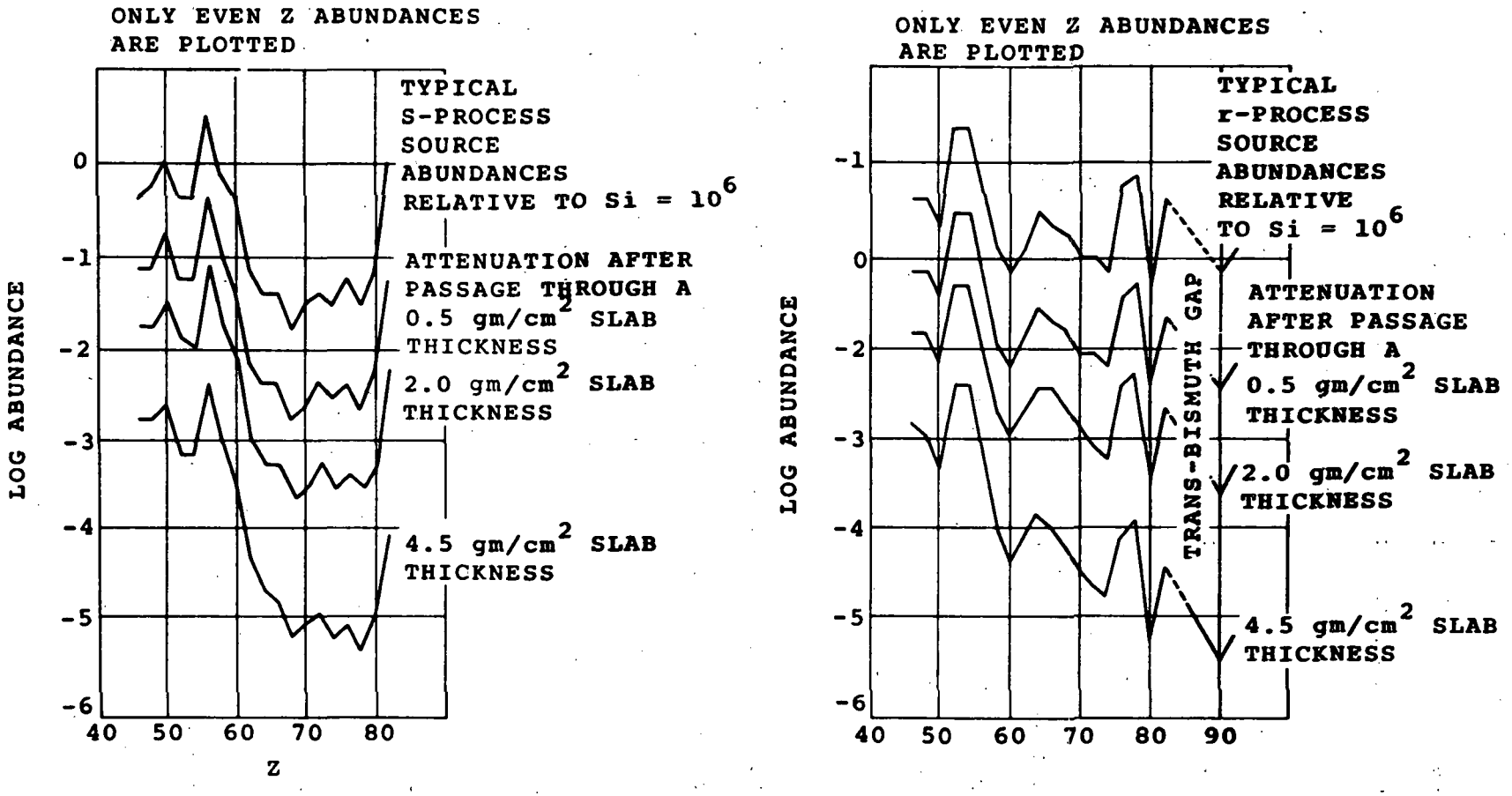
ONLY EVEN Z ABUNDANCES ARE PLOTTED
TYPICAL S-PROCESS SOURCE ABUNDANCES RELATIVE TO Si = 10^6
ATTENUATION AFTER PASSAGE THROUGH A 0.5 gm/cm^2 SLAB THICKNESS
2.0 gm/cm^2 SLAB THICKNESS
4.5 gm/cm^2 SLAB THICKNESS
LOG ABUNDANCE
Z
a.
ONLY EVEN Z ABUNDANCES ARE PLOTTED
TYPICAL r-PROCESS SOURCE ABUNDANCES RELATIVE TO Si = 10^6
ATTENUATION AFTER PASSAGE THROUGH A 0.5 gm/cm^2 SLAB THICKNESS
2.0 gm/cm^2 SLAB THICKNESS
4.5 gm/cm^2 SLAB THICKNESS
TRANS-BISMUTH GAP
LOG ABUNDANCE
b.

FIGURE 24

s-process relative abundances given in Figure 21a. The source abundances in Figure 24a have been plotted relative to Si = 10^6, and the calculation results have been plotted with respect to these source abundances. Figure 24b contains the corresponding plots for the case where the source was taken to be the solar system r-process abundances given in Figure 21b. For these calculations, ν was taken to be 7.2. The relative abundances are virtually insensitive to the kinetic energy per nucleon, E, that was employed for E > 600 MeV/nuc, but the energy spectrum is slightly flattened by the propagation. For example, interstellar propagation through a slab thickness $\sim$ 0.5 gm/cm^2, changes ν from 7.2 at the source, to $\sim$ 6.6 near the earth, for Z $\sim$ 75 nuclei.

Cowsik, et. al,[83] have previously considered the slab model as applied to the propagation of trans-iron cosmic ray nuclei. Their calculations assumed ν = 2.6, and they concluded that for a slab thickness of $\sim$ 4 gm/cm^2, in order to explain the ($80 \geq Z \geq 36/Z > 80$) ratio, which from the available data (corrected to outside of the solar cavity) is $\lesssim$ 15, one must assume a source which is composed of essentially only U-group nuclei. If the source had a ($80 \geq Z \geq 36/Z > 80$) ratio which was >> 1, then their slab model calculation for X_{slab} = 4 gm/cm^2 and ν = 2.6, indicated that the ratio near earth would be >> 100. The existence of a source that supplies only U-group trans-iron nuclei is contrary to our understanding of the r-process, which is currently the only theory that provides for

U-group nucleosynthesis. Thus, Cowsik, et. al. argued that the slab model is inadequate to explain the observed trans-iron cosmic ray fluxes when slab thicknesses $\sim$ 4 gm/cm^2 (i.e., the slab thickness required to explain the L/M ratio) are employed.

Since the CREPE II data indicate that the energy spectrum of the $Z > 60$ cosmic rays is much steeper than $\nu = 2.6$ (i.e., $\nu \sim 7.2$), we should recheck the validity of Cowsik, et. al.'s conclusion, for the case of a steeper energy spectrum.

Table 8 presents the results of the present slab model calculations with the solar system r-process source of Figure 21b, (i.e., no spheroidal effects) for $\nu = 2.6$, and $\nu = 7.2$. The table has been divided into various charge groups, and normalized in each case to the U-group. The values listed for the slab model results represent the relative integral flux above a kinetic energy of 600 MeV/nuc. The data from CREPE II and the combined currently available data for $Z > 50$ from all of the trans-iron cosmic ray experiments, corrected to outside of the solar cavity and normalized to the U-group, have also been included.

The last row in Table 8 contains the ($84 \geq Z \geq 51$/U-group) ratios. (The $84 \geq Z \geq 51$ group has been used for comparison rather than the $80 \geq Z \geq 36$ group used by Cowsik et. al., since the former group has greater relevance to this experiment.) From these ratios

TABLE 8

COMPARISON OF SLAB MODEL RESULTS

The results of slab model calculations with $X_{SLAB} = 4.5$ gm/cm^2 are presented for $\nu = 2.6$, and $\nu = 7.2$ (ν is the index of the differential total energy spectrum at the source). The source abundances employed in these calculations were the solar system r-process abundances from Figure 21b. These abundances do not include the effects of spheroidal deformation. Also included in the table are the corresponding abundance values from the data. Each of the columns in the table have been individually normalized to the U-group.

a. The final measurements from the CREPE II data for the $59 \geq Z \geq 51$ group have not yet been completed.

TABLE 8

COMPARISON OF SLAB MODEL RESULTS

	SOLAR SYSTEM r-PROCESS	DATA (Corrected to outside of the solar cavity)		SLAB MODEL (X_{slab} = 4.5 gm/cm^2 Fig. 21b Source - No spheroidal deformation effects) N(> 600 MeV/nuc)	
	No spheroidal deformation effects (Fig. 21b)	CREPE II	Combined currently available	ν = 2.6	ν = 7.2
96≥Z≥88 (U-group)	1.00	1.00	1.00	1.00	1.00
84≥Z≥80 (Pb-group)	1.10	1.0±0.7	$.57^{+.34}_{-.21}$	4.78	5.10
79≥Z≥74 (A_3-group)	5.83	3.8±1.3	1.75±.55	38.19	42.91
73≥Z≥60	4.36	6.0±1.6	2.28±.52	84.81	107.96
59≥Z≥51	20.12	1.1[a]	4.1 ±.9	1151.16	1679.59
(84≥Z≥51)/U-group	31.41	11.9	8.64±1.21	1278.94	1835.56

one can see that the disagreement between the data and a slab model, with an r-process source and $X_{slab} = 4.5$ gm/cm^2, is even greater when $\nu = 7.2$ than it is for $\nu = 2.6$. Thus, barring the existence of some, as yet, undiscovered U-group nucleosynthesis process one can reasonably rule out the slab model for slab thicknesses ~ 4 gm/cm^2. Since a slab thickness of ~ 4 gm/cm^2 is required to explain the L/M ratio, the slab model does not appear to provide a viable theory of cosmic ray interstellar propagation.

2.) Exponential Model

This particular version of the model was originally discussed by Cowsik, et. al.[84] and assumes a steady state of cosmic rays in the galastic disk, which is maintained by a uniform injection and rapid diffusion throughout the volume of the disk, with a slow leakage at the surface. Cowsik et. al., have employed a rigidity dependent expression for the mean vacuum path length for leakage out of the disk, λ_e, which is of the form $\lambda_e = 3 + 25/R(GV)$ gm/cm^2. However, since the relative abundances for the heavier trans-iron nuclei are extremely insensitive to λ_e, (see Figure 25), we have chosen to employ λ_e as a constant parameter, independent of rigidity. The diffusion equation for the exponential model (using the same notation

employed in the discussion of the slab model above), is given by:[85]

$$\frac{dJ_i(E)}{dX} = -\frac{J_i(E)}{\lambda_i} - \frac{J_i(E)}{\lambda_e} - \frac{J_i(E)}{\gamma\rho_H v(E)\tau_i} +$$

$$\sum_{j>i}\left(\frac{P_{ji}}{\lambda_j} + \frac{B_{ji}}{\gamma\rho_H v(E)\tau_i}\right)J_j(E) - \frac{\partial}{\partial E}\left(\left(J_i(E)\left(\frac{\partial E}{\partial X}\right)_i\right)\right) + Q_i\,, \quad (65)$$

where Q_i represents the source injection. The appropriate exponential vacuum path length distribution is of the form e^{-X/λ_e}.

Since an $X = 0$ path length is non-physical, one introduces[86] the additional parameter, X_{min}, which is the lower path length cut-off (i.e., the vacuum path length distribution is given by 0 for $X < X_{min}$ and $\exp(-X/\lambda_e)$ for $X \geq X_{min}$). Then, the solution of equation (62), in the form $J_i(E) = J_{i,1}(E) + J_{i,2}(E)$ is given by:[87]

$$J_{i,1}(E) = \frac{e^{X_{min}/\lambda_e}}{\lambda_e}\int_{X_{min}}^{\infty} f^i_{ion}(E,X)\, J_{i,0}(E)\, \exp\left(-X\left(\frac{1}{\lambda_i} + \frac{1}{\lambda_e} + \frac{1}{\gamma\rho_H v(E)\tau_i}\right)\right) dX, \quad (66)$$

and,

$$J_{i,2}(E) = \frac{e^{-X_{min}/\lambda_e}}{\lambda_e}\int_{X_{min}}^{\infty} \exp\left(-X\left(\frac{1}{\lambda_i} + \frac{1}{\lambda_e} + \frac{1}{\gamma\rho_H v(E)\tau_i}\right)\right)$$

$$\sum_{j>i}\left(\frac{P_{ji}}{\lambda_i} + \frac{B_{ji}}{\gamma\rho_H v(E)\tau_i}\right)J_{i,0}(E)\int_{X_{min}}^{X} f^i_{ion}(E,X-X_j)\, f^j_{ion}(E,X_j)$$

$$\exp\left(-X_j\left(\frac{1}{\lambda_j} + \frac{1}{\gamma\rho_H v(E)\tau_i} - \frac{1}{\lambda_i} - \frac{1}{\gamma\rho_H v(E)\tau_i}\right)\right) dX_j \quad dX\,. \quad (67)$$

In this case, $J_{i,0}$ represents the intensity of i-type nuclei in absnece of interstellar matter or any modulation effects.

The relative intensity predicted to exist in interstellar space by the exponential model, $J_{i,exp}(E)$ is then given by the sum of $J_{i,1}(E)$ and $J_{i,2}(E)$ from equations (66) and (67). For all of the exponential model calculations discussed below, the integrals in equations (66) and (67) were numerically integrated.

For this model, there are two parameters of interest, the exponential mean path length, λ_e and the lower path length cut-off, X_{min}. λ_e appears in the solution in the factor $\exp(-X\,[1/\lambda_e + 1/\lambda_i + \frac{1}{\gamma\rho_H v(E)\tau_i}])$; and thus, for $\lambda_e >> \lambda_i$, λ_e has very little effect on the relative abundances. As stated in Section 3A, the value for λ_e that best fits the cosmic ray data for $Z \leq 26$ is ~ 4.34 gm/cm^2. It is reasonable to suspect that the mean leakage path length for trans-iron nuclei is similar to that for Fe and lighter nuclei. Since, λ_i for the heavier trans-iron nuclei is < 1 gm/cm^2, the choice of λ_e is not significant.

Figure 25 includes plots for $Z > 45$ of $J_{i,exp}(E)$ at a kinetic energy of 1000 MeV/nuc and with $\lambda_e = 4.34$ gm/cm^2, for $X_{min} = 0.1$, 0.25, and 0.5 gm/cm^2 (as in Figure 24, only the even Z abundances have been plotted). In these calculations, ν was taken to be 7.2. For the spectra in Figure 25a, the solar system s-process abundances

normalized to Si = 10^6, were used for $J_{i,0}$, and the calculation results have been plotted relative to these source abundances. Figure 25b corresponds to the case where the solar system r-process abundances of Figure 21b (i.e., no spheroidal deformation effects) were used for $J_{i,0}$. As in the case of the slab model, the relative abundances are insensitive to the kinetic energy per nucleon, E, for E > 600 MeV/nuc, and the energy spectrum is flattened by the propagation. For the case where $\lambda_e = 4.34$ and $X_{min} = 0.1$, ν is decreased from 7.2 at the source to 6.3 in interstellar space, and for $\nu \sim 7.2$ in interstellar space, the source spectrum must have $\nu \gtrsim 8$.

Table 9 displays the results of exponential model calculations with $\lambda_e = 4.34$ gm/cm^2 and $X_{min} = 0.1$, for both $\nu = 2.6$ and $\nu = 7.2$, where the source abundances were taken to be the r-process solar system abundances presented in Figure 21b (i.e., no spheroidal deformation effects). The results of this calculation using $\nu = 7.2$ for the case where the source abundance reflects the minimum possible ($84 \geq Z \geq 51$/U-group) ratio that can be expected with the inclusion of the spheroidal deformation effects as discussed in Section 2B of this Chapter, have also been given in Table 9. This minimum ratio was 15.70, and it was calculated by taking Hoyle and Fowler's estimates for the maximum possible U-group abundances expected after the inclusion of the spheroidal deformation effects. From the combined data currently available (corrected to outside of the

FIGURE 25

RESULTS OF EXPONENTIAL MODEL PROPAGATION

a. This plot displays the results of exponential model propagation with $\lambda_e = 4.34$, on the s-process solar system abundances (based on Si = 10^6). The curves corresponding to $X_{min} = 0.1$, 0.25, and 0.5 are indicated. The result for $\lambda_e = 1.0$ gm/cm^2 and $X_{min} = 0.25$ gm/cm^2 is also indicated. One can observe from a comparison of the $\lambda_e = 1.0$ gm/cm^2, $X_{min} = 0.25$ gm/cm^2 curve with the $\lambda_e = 4.34$ gm/cm^2, $X_{min} = 0.25$ gm/cm^2 curve, that the different values of λ_e have almost no effect on the relative abundances. This demonstrates that the calculation of relative abundances is insensitive to λ_e, and justifies the use of λ_e as a constant parameter, independent of rigidity.

b. These are the corresponding curves for the solar system r-process abundance (based on Si = 10^6).

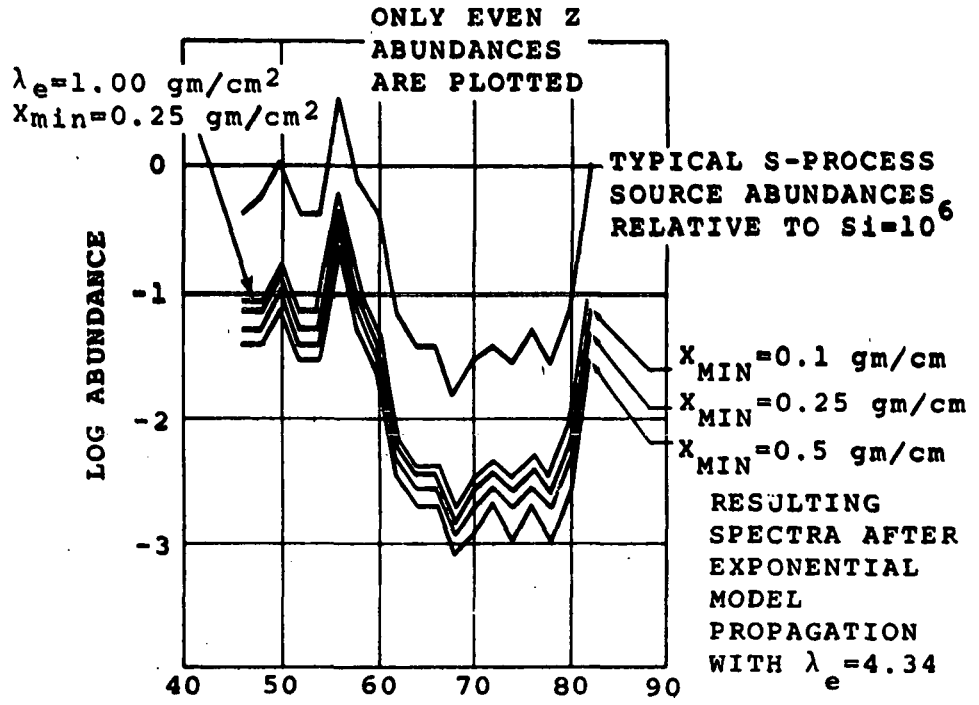
ONLY EVEN Z ABUNDANCES ARE PLOTTED
λ_e=1.00 gm/cm^2
X_{min}=0.25 gm/cm^2
TYPICAL S-PROCESS SOURCE ABUNDANCES RELATIVE TO Si=10^6
LOG ABUNDANCE
0
-1
-2
-3
40
50
60
70
80
90
X_{MIN}=0.1 gm/cm
X_{MIN}=0.25 gm/cm
X_{MIN}=0.5 gm/cm
RESULTING SPECTRA AFTER EXPONENTIAL MODEL PROPAGATION WITH λ_e=4.34

a.

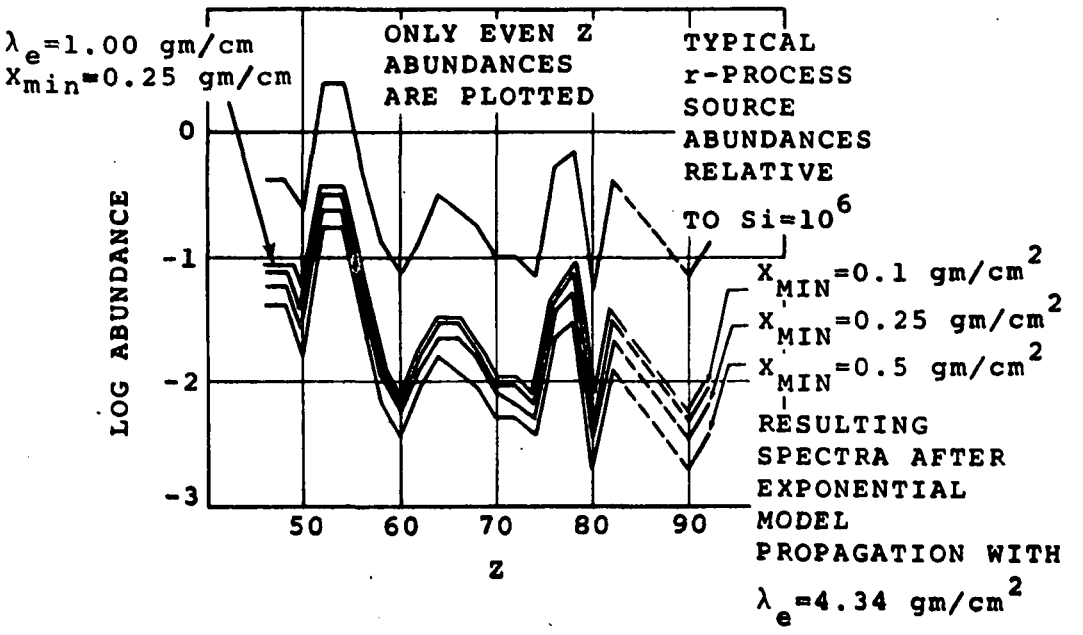
λ_e=1.00 gm/cm
X_{min}=0.25 gm/cm
ONLY EVEN Z ABUNDANCES ARE PLOTTED
TYPICAL r-PROCESS SOURCE ABUNDANCES RELATIVE TO Si=10^6
LOG ABUNDANCE
0
-1
-2
-3
50
60
70
80
90
Z
X_{MIN}=0.1 gm/cm^2
X_{MIN}=0.25 gm/cm^2
X_{MIN}=0.5 gm/cm^2
RESULTING SPECTRA AFTER EXPONENTIAL MODEL PROPAGATION WITH λ_e=4.34 gm/cm^2

b.

FIGURE 25

TABLE 9

COMPARISON OF EXPONENTIAL MODEL RESULTS

This table presents the results of exponential model propagation calculations with $\lambda_e = 4.34$ gm/cm^2 and $X_{min} = 0.1$ gm/cm^2. The results for the cases where the source spectrum is taken to be the r-process abundances which neglect spheroidal deformation effects (for both $\nu = 2.6$ and $\nu = 7.2$) are compared with the case where the maximum possible spheroidal deformation effects have been included in the source abundances (for $\nu = 7.2$). The data have also been included in this table, and all of the columns have been individually normalized to the U-group.

a. The final measurements from the CREPE II data for the $59 \geq Z \geq 51$ group have not yet been completed.

TABLE 9

COMPARISON OF EXPONENTIAL MODEL RESULTS

	SOLAR SYSTEM r-PROCESS		DATA (Corrected to outside of the solar cavity)		EXPONENTIAL MODEL (λ_e = 4.34 gm/cm^2, X_{min} = 0.1 gm/cm^2)		
	No spheroidal deformation effects (Fig. 21b)	Maximum spheroidal deformation effect	CREPE II	Combined currently available	Source - No spheroidal deformation effects N(> 600 MeV/nuc) ν=2.6	ν=7.2	Source - Max. spheroidal deformation effects ν=7.2
96≥Z≥88 (U-group)	1.00	1.00	1.00	1.00	1.00	1.00	1.00
84≥Z≥80 (Pb-group)	1.10	.55	1.0±0.7	$.57^{+.34}_{-.21}$	1.92	1.99	.99
79≥Z≥74 (A_3-group)	5.83	2.91	3.8±1.3	1.75±.55	10.76	11.20	6.60
73≥Z≥60	4.36	2.18	6.0±1.6	2.28±.52	10.21	10.82	5.41
59≥Z≥51	20.12	10.06	1.1[a]	4.1 ±.9	56.59	60.40	30.20
(84≥Z≥51)/U-group	31.41	15.70	11.9	8.64±1.21	79.48	84.41	43.20

solar cavity) which is discussed in Section 4 below, the ($84 \geq Z \geq 51$/U-group) ratio is 8.64 ± 1.21. This ratio is almost a factor of 2 less than the minimum obtainable ratio in the source abundance based on the current understanding of U-group nucleosynthesis. Since this ratio increases after interstellar propagation, there is clearly a discrepancy between the data and our estimates of the source abundances. This discrepancy makes it virtually impossible to evaluate the parameters of the exponential model. It may, however, be stated that the exponential model yields a ($84 \geq Z \geq 51$/U-group) ratio which is considerably closer to the source ratio than the ratio obtained from the slab model. Thus, in conclusion, we are at present unable to evaluate how well the exponential model represents the propagation of trans-iron cosmic rays, but one can observe that it gives significantly more compatible results than the slab model.

3.) Cosmic Ray Clocks

Since the presently available trans-iron charge resolution ($\sim \pm 4\%$) is unable to resolve individual elements, we cannot yet estimate the propagation time through a measurement of the abundances of individual radioactive nuclides and their decay products. We can, however, examine the relative abundances of groups of nuclides, and the abundance ratios between these groups. This may yield at least some information regarding the age of the heavier trans-iron cosmic rays.

Consider the U-group nuclei. All of these nuclei possess half lives $\leq 10^{10}$ years, and $\sim 2/3$ of them (based on solar system r-process abundances) have half lives $\leq 7 \times 10^{8}$ years. During propagation these nuclei are removed from the galactic flux by three processes: fragmentation, radioactive decay, and leakage out of the galactic disc. As discussed in Section 2 above, the mean free path for leakage out of the galaxy, λ_e, has a negligible effect on the observed trans-iron relative abundances (at least for $\lambda_e \geq 2$ gm/cm^2), and therefore, if $\lambda_e >> \lambda_i$, λ_e will have no significant effect on the ratio between groups of trans-iron nuclei. The fragmentation of U-group nuclei by interstellar H, according to the cross sections of Silberberg and Tsao, results primarily in a fission that produces two daughter nuclei both of which have $Z \leq 60$ Further, these cross sections indicate that only a small fraction (< 5%) of the U-group fragmentation products occur in the range $83 \geq Z \geq 80$. ($83 \geq Z \geq 80$ will be referred to as the "Pb-group", and includes Pb and Bi.) This last observation is important since the radioactive decay paths of the U-group nuclei all lead finally to the production of either Pb or Bi. This implies that the (U-group/Pb-group) ratio will decrease with time as the decaying U-group nuclei enhance the Pb-group. Since the U-group fragmentation products will not significantly effect the Pb-group abundance, the only other factor affecting this ratio is the slight difference in interaction mean free paths between the two groups ($\lambda_i \sim 0.54$ gm/cm^2 for U-group nuclei, and $\lambda_i \sim 0.58$ gm/cm^2 for the Pb-group

nuclei). Thus, the (U-group/Pb-group) ratio is relatively sensitive to the elapsed time since nucleosynthesis, and significantly less sensitive to the thickness of matter traversed. This was first pointed out by Mewaldt, et. al.[88] Their interest in a measure of the duration of the propagation, as opposed to a measure of the thickness of matter traversed, is due to the possibility that the density of matter in the medium being traversed may not have been constant during the entire propagation.

If the mean path length for escape of trans-iron nuclei from the disc were $<< 2$ gm/cm^2, λ_e would then become comparable to λ_i, and as such cause a non-negligible effect upon the trans-iron relative abundances. In addition to affecting the relative abundances predicted by the exponential model, a small λ_e would imply that a significant number of trans-iron nuclei would leak from the disc into the galactic halo, a region of considerably less gas density than the disc ($\sim$ 1 atom/cm^3 in the disc and $\lesssim$ 0.01 atom/cm^3 in the halo).[89] According to the theory originally proposed by Ginzburg and Syrovatskii,[90] after leakage from the disc, the nuclei would be "stored" in the halo region for some characteristic time determined by the rate of leakage out of the halo into intergalactic space, and the leakage from the halo back into the disc (for our galaxy this storage time is typically $\sim 10^8$ years).[91] Thus, the flux observed in the disc is the superposition of the nuclei that have not yet leaked out of the

disc (disc component), with those which have been stored in the halo and subsequently leaked back into the disc (halo component).

For the disc component with the exponential model, the effective mean path length in gm/cm^2, $\lambda_{mean,i}(E)$, traversed by an i-type nucleus with kinetic energy per nucleon, E, is given by:

$$\lambda_{mean,i}(E) = \lambda_0 \ (1 + X_{min}/\lambda_0) \quad , \tag{68}$$

where $1/\lambda_0 = (1/\lambda_i + 1/\lambda_e + 1/\gamma\rho_H v(E)\tau_i)$. Using equation (68), the "mean age", $\tau_{i,mean}(E)$, of the disc component of i-type nuclei with kinetic per nucleon, E, is given by:

$$\tau_{i,mean}(E) = \frac{\lambda_{mean,i(E)}}{\gamma\rho_H v(E)} \quad . \tag{69}$$

From equation (69) one finds that for "reasonable parameters" (e.g., λ_e = 4.34 gm/cm^2 and X_{min} < 0.5 gm/cm^2), the exponential model predicts the mean lifetime of the disc component of the heavier trans-iron nuclei (e.g., Pb at 1000 MeV/nuc) to be $\lesssim$ 5 x 10^5 years. This is less than the $\gtrsim$ 10^6 year lifetimes of the sub-iron disc component,[92] and much less than the 10^8 year halo storage time. Thus, a time sensitive ratio (e.g., U-group/Pb-group) should be able to determine whether or not the observed flux possesses any substantial halo component.

Figure 26 is a plot of the (U-group/Pb-group) ratio as a function of λ_e for the disc component and the halo component. The disc solutions were calculated by varying λ_e for the exponential model of the previous section, and the "halo solutions" were obtained by using the same model with $N_a = 0.01$ atoms/cm^3. For the halo solutions, λ_e is the mean leakage path length from the halo into intergalactic space. ν was taken to be 7.2 at the source, and the ratios were compiled for the integral fluxes with a kinetic energy $\geq$ 600 MeV/nuc. The range of solutions due to the possible effects of spheroidal deformation on the U-group abundances, have been indicated in each case. The ratio from the combined currently available data (as discussed in the next section), is $1.75^{+1.0}_{-.65}$, and is plotted in Figure 26, at $\lambda_e = 4.34$ gm/cm^2 for reference only. This plot illustrates the discrepancy between the data and our estimates of the source abundances. A measured (U-group/Pb-group) ratio of 1.75 implies (assuming a disc component with $\nu = 7.2$) that the source ratio should be $\sim$ 3.5 and the maximum ratio from the solar system r-process is $\sim$ 1.8. Because of this discrepancy we are prevented from drawing any serious conclusions. To illustrate this point, let us consider the admittedly highly unlikely but not impossible situation, that there are no Pb-group elements at the source. In this case, assuming a disc component with $\nu = 7.2$ at the source, it would require a mean propagation lifetime of $\gtrsim 10^7$ years to explain the observed ratio of $\sim$ 1.75. (For a predominantly halo component and $\nu = 7.2$, a (U-group/Pb-group) ratio of 1.75 is

obtained after $\sim 10^8$ years with a Pb-group deficient source.) Thus, we cannot absolutely rule out any mean propagation lifetime $< 10^8$ years, until we have some definite information regarding probable source abundances. This information may become available after the charge spectrum has been measured more accurately and such data as the locations of the r-process peaks are known. This will allow an accurate estimate of the actual r-process environment and in turn will allow a better calculation of the expected abundances.

There are a number of other time sensitive ratios that have been suggested by various authors (e.g., A_3-group/Pb-group, A_3-group/U-group, etc.). Unfortunately, these ratios all suffer from our uncertainties regarding the source abundances, and because of this, they offer no greater insight as to the mean age of the trans-iron cosmic rays.

4. DISCUSSION OF THE DATA

A. Charge Spectrum

The CREPE II charge data as presented in Figure 18 of Chapter IV, possess too few events to allow a meaningful evaluation of the $Z > 50$ trans-iron cosmic ray charge spectrum. However, a composite of the charge data from all of the previously conducted trans-iron cosmic ray experiments does possess enough events to begin to allow an analysis of the spectral abundances.

FIGURE 26

U-GROUP/Pb-GROUP vs. λ_e

This plot compares the variation of the (U-group/Pb-group) ratio as a function of λ_e where ρ_H is taken to be 1 atom/cm^2 (disc solution), with the case where ρ_H is taken to be 0.01 atom/cm^2 (halo solution). The range of possible solutions which arises in each case from the uncertainty in the effects that spheroidal deformation has on the possible source r-process U-group abundances. The ratio obtained from the data is plotted at λ_e = 4.34 gm/cm^3 for reference only.

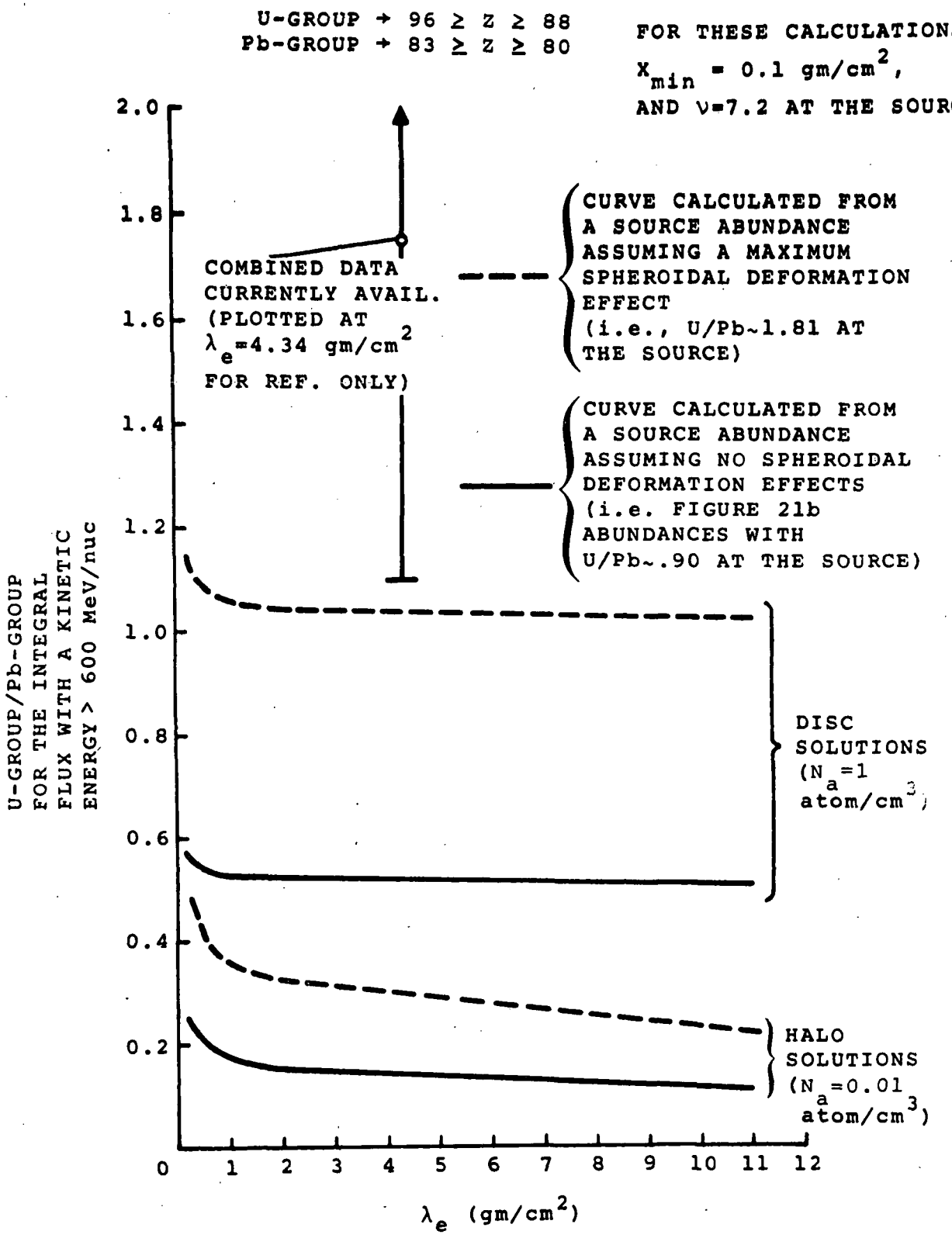
U-GROUP → 96 ≥ Z ≥ 88
Pb-GROUP → 83 ≥ Z ≥ 80
FOR THESE CALCULATIONS
X_{min} = 0.1 gm/cm^2,
AND ν=7.2 AT THE SOURCE
COMBINED DATA CURRENTLY AVAIL. (PLOTTED AT λ_e=4.34 gm/cm^2 FOR REF. ONLY)
CURVE CALCULATED FROM A SOURCE ABUNDANCE ASSUMING A MAXIMUM SPHEROIDAL DEFORMATION EFFECT (i.e., U/Pb~1.81 AT THE SOURCE)
CURVE CALCULATED FROM A SOURCE ABUNDANCE ASSUMING NO SPHEROIDAL DEFORMATION EFFECTS (i.e. FIGURE 21b ABUNDANCES WITH U/Pb~.90 AT THE SOURCE)
DISC SOLUTIONS (N_a=1 atom/cm^3)
HALO SOLUTIONS (N_a=0.01 atom/cm^3)
U-GROUP/Pb-GROUP FOR THE INTEGRAL FLUX WITH A KINETIC ENERGY > 600 MeV/nuc
2.0
1.8
1.6
1.4
1.2
1.0
0.8
0.6
0.4
0.2
0
1
2
3
4
5
6
7
8
9
10
11
12
λ_e (gm/cm^2)

FIGURE 26

Figure 27 contains a histogram charge spectrum which represents a composite of all of the currently available data for $Z > 50$ cosmic rays,[93] (including CREPE II). These plots have been corrected to outside of the solar cavity and are rounded off to the nearest whole charge. The plot is normalized to yield the number of U-group events in interstellar space required to account for the number of U-group events observed at balloon altitudes after all of the corrections have been applied. The average uncertainty in the charge assignment is $\sim \pm 4\%$.

The U-group can be easily distinguished from the $Z < 88$ events due to the existence of the trans-Bismuth gap $87 \geq Z \geq 84$, which contains no stable or long lived nuclides. Since the data possess such a gap, one considers all of the events above the gap to be U-group events. Thus, the error in the charge assignment does not hinder the identification of U-group events; it only limits the resolution of individual abundances within the group.

Unfortunately, the separation of the Pb-group ($83 \geq Z \geq 80$) events from the potential r-process A_3-group ($79 \geq Z \geq 75$) events is not as easy. Assuming, the $\pm$ 4% error, there are 8 (+7, -4) Pb-group ($83 \geq Z \geq 80$) events and 27 (+13, -10) A_3-group events in the composite (raw) data. The errors in the number of Pb-group and A_3-group events are coupled in the sense that the minimum value for the A_3-group corresponds to the maximum value for the Pb-group and

vice versa.

Even with these charge assignment uncertainties, one is still able to make the following comments regarding the nature of the nucleosynthesis at the source. First, the very existence of U-group nuclei in the trans-iron cosmic ray flux indicates that at least some r-process nucleosynthesis must be present at the source, and this, coupled with the overall data for $Z > 50$, strongly suggests that the source is "primarily" r-process. The A_2 and A_3 peaks are present, and combined with the apparent lack of a dominant Pb peak, one is hard pressed to make a case for a significant s-process contribution.

Proceeding then, on the assumption that the $Z > 50$ trans-iron cosmic rays are only synthesized through an r-process, information regarding the parameters of that r-process can be inferred from an examination of the corrected data. The location of the A_3 peak is a measure of the cycle time and the duration of the process, as outlined in Section 5B. From the data, the peak appears to be closer to $Z = 76$ rather than to the $Z = 78$ peak which is characteristic of the r-process elements contained in the solar system abundances. However, this difference is still within the charge assignment errors ($\sim \pm 3$ in the vicinity of $Z = 75$), and the statistics of only ~ 23 events with $79 \geq Z \geq 74$ preclude a strong claim on a peak at $Z = 76$, as opposed to 77 or 78. If the A_3 peak

FIGURE 27

Z > 50 CHARGE SPECTRUM ASSEMBLED FROM THE COMBINED PUBLISHED DATA

This histogram represents both the raw data available from all of the currently published trans-iron cosmic ray experiments (including CREPE II), and that data corrected to outside of the solar cavity, renormalized to the U-group abundance required to produce the number of U-group events observed at balloon altitudes, and rounded off to the nearest charge. The A_2 peak, A_3 peak, trans-Bismuth gap, and U-group are all clearly visible. This leads to the conclusion that the source nucleosynthesis is predominantly r-process.

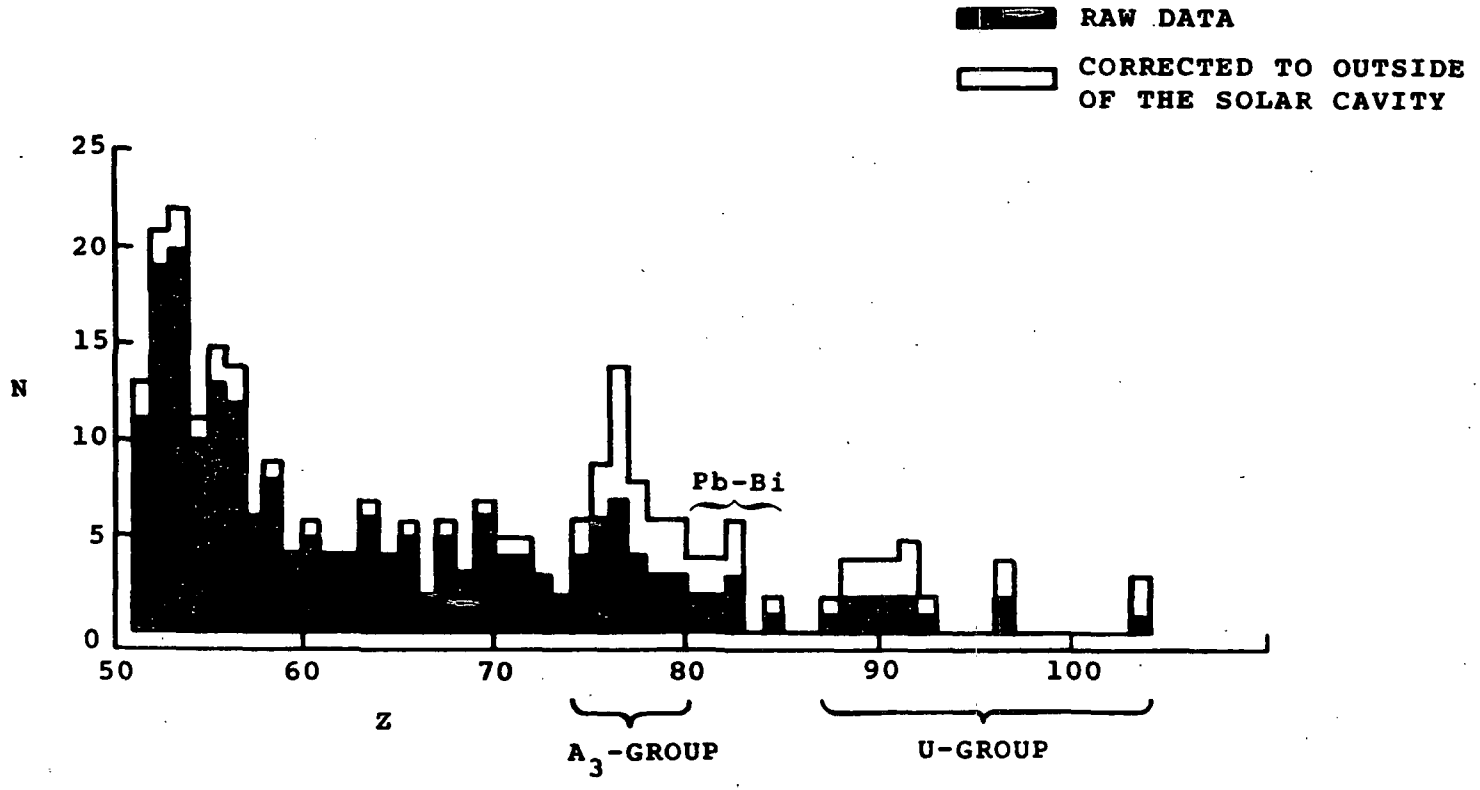
RAW DATA
CORRECTED TO OUTSIDE OF THE SOLAR CAVITY
N
25
20
15
10
5
0
50
60
70
80
90
100
Z
Pb-Bi
A_3-GROUP
U-GROUP

FIGURE 27

is indeed located at Z = 76, Figure 23 implies a very short cycle time, $\sim$ 1 second. Seeger, et. al.,[94] have shown as indicated in Figure 22, that a cycle time of $\sim$ 1 second implies that the temperature during nucleosynthesis was probably less than 1.4×10^9 °K and the corresponding neutron density was probably $\gtrsim 10^{28}/cm^3$. The final observation one can make from the data regarding the r-process environment is that the existence of a well formed A_3 peak and U-group indicates that the nucleosynthesis probably continued for a number of cycle times. If these two features had been less well formed, one would have predicted durations of $\lesssim$ 1 cycle time.

B. Energy Spectrum

The most significant result of the CREPE II experiment has been the observation that the Z > 60 cosmic ray nuclei have an energy spectrum which is considerably steeper ($\nu = 6.5 \pm 1.7$ at the top of the atmosphere and $\nu \sim 7.2 \pm 2$ outside of the solar cavity), than the almost universal $\nu \sim 2.6$ spectrum of the sub-iron cosmic rays. This difference cannot be accounted for by any of the corrections, nor by any reasonable uncertainties in the corrections. Further, the result of the exponential model calculations indicate that in general the Z > 60 energy spectrum is even steeper at the source.

The reason for the differences between the energy spectrum of the heavy trans-iron cosmic rays and the sub-iron cosmic rays, is not understood, partly because there is as yet, no clear-cut agreement on the acceleration mechanism which produces the observed $\nu \sim 2.6$ spectrum for the sub-iron cosmic ray nuclei.

Current theories concerning the acceleration of cosmic rays are based on their hypothesized supernova origin. With the recent discovery of rapidly pulsating stellar sources[95] (pulsars), and the subsequent association of several pulsars with supernova remnants,[96] it appears safe to conclude that at least some supernovae leave pulsars as remnants. Pulsars are believed to be rapidly rotating magnetic neutron stars which are capable of emitting electromagnetic energy in quantities necessary to explain the observed cosmic ray energy spectrum. In order for the rate of supernovae in the galaxy to support the observed cosmic ray energy spectrum, $\sim 10^{49.5}$ ergs would be required per supernova.[97] It is estimated that between 10^{50} and $10^{52.5}$ ergs are available in the form of pulsar rotational energy, of which $> 10^{49}$ ergs are dissipated by the acceleration of charged particles.[98] These pulsars are thought to be $\sim$ 10 km in diameter, and possess surface magnetic fields $\gtrsim 10^{12}$ gauss.[99] Rotational frequencies (i.e., pulsar frequencies) as high as $\sim$ 300/second, and decreases in frequency with time, which may be attributed to a slowing down due to electromagnetically radiated losses in rotational energy, have been observed.[100]

Grewing and Heintzmann[101] have purposed that the intense low frequency electromagnetic waves in the immediate vicinity of a pulsar are capable of accelerating charged particles to energies of 10^{18} - 10^{23} eV. Unfortunately, their model is unable to produce significant quantities of the moderately relativistic (10 GeV/nuc $\geq$ E $\geq$ 1 GeV/nuc) particles that comprise the bulk of the cosmic ray flux.

Kulsrud, Ostriker and Gunn,[102] have since suggested that the intense low frequency electromagnetic waves are probably not entirely dissipated in the vicinity of the neutron star, but are still strong enough when they reach the nebular filaments, to accelerate charged particles to relativistic energies. The very recent observation of polarized X-rays emanating from the Crab nebula,[103] which are thought to be due to synchrotron emission by accelerating nuclear charged particles, has been claimed as strong evidence for the acceleration of these particles in the Crab Nebula.

According to the model of Kulsrud, Ostriker, and Gunn, the nebular filaments are approximated by a single expanding spherical shell. The cavity bounded by the shell is filled with strong electromagnetic waves generated by a rapidly rotating neutron star at the center, whose magnetic dipole moment is assumed to have a non-zero component perpendicular to the axis of rotation. When $r_s(t)$, the time dependent radius of the shell, is $> \lambda \quad \nu_o^{2/3}$, where $\nu_o =$ (Z/A) x 2.26 x 10^{-12} $L^{\frac{1}{2}}$, (L being the pulsar magnetic dipole

luminosity in ergs/sec.), and λ is the wavelength of the magnetic dipole radiation, a particle which is injected into the cavity from the shell at some time t, will be accelerated to a kinetic energy per nucleon, E, which can be written:[104]

$$E = \frac{3m_{nuc} \nu_o^2 \lambda^2}{4 r_s(t)^2} - m_{nuc} \qquad (70)$$

Thus, the kinetic energy per nucleon to which a particle is accelerated by this model is a function of the radius of the shell at the time of injection. If one assumes that $r_s(t) \propto t^{\xi}$ and that the rate of injection of a given nuclear species from the shell is constant, then after long times, the differential energy spectrum of these nuclei produced by the entire event is a power law in <u>total</u> energy per nucleon with index $-1 - 1/(2\xi)$. Since ν_o is a function of A/Z, at any given radius $r_s(t)$, the kinetic energy per nucleon attained by an injected nucleus is a function of A/Z. However, the index of the differential total energy per nucleon spectrum for a given nuclear species resulting from a single supernova is independent of the A/Z ratio. Although this is in complete agreement with the current cosmic ray data for the sub-iron nuclei,[105] the model does not account for the observed differences between the energy spectra of the heavy trans-iron and the sub-iron cosmic rays.

In conclusion, the $Z > 60$ cosmic ray energy spectrum appears

to be fundamentally steeper than the sub-iron nuclei, and the current acceleration models are unable to account for this difference. Further, it is quite possible that the index of the differential energy spectrum has some Z^2, or Z/A dependence for trans-iron nuclei, with the heaviest nuclei having the steepest spectra. We clearly do not possess sufficient data to evaluate this conjecture. Finally, in light of this possibility, an effort should be made to take a very close look at the energy spectrum of the $60 \geq Z \geq 26$ nuclei.

CHAPTER VI

SUMMARY

During the course of this dissertation several observations and conclusions were made concerning fast film Cerenkov detectors, and the available data on the trans-iron cosmic rays. These are briefly summarized here.

Plastic track detectors and nuclear emulsions, which are the primary detectors employed in the present trans-iron cosmic ray experiments, are both hindered by the necessity of obtaining an independent measurement of the velocity of each particle (at least for the events with $\beta > 0.75$) in order for these detectors to provide an acceptable charge resolution. Conventional methods for velocity determination through the use of thick detector stacks suffer from the problem of nuclear interactions in the stack, and from the requirement of flying relatively heavy payloads, which is limiting in balloon altitude and total detector area. Thus, there is a requirement for a light, durable detector which is capable of providing these velocity measurements.

A fast film Cerenkov detector that is able to provide velocity measurements for particles with $Z \geq 60$ and $\beta \geq 0.68$ has been designed and flown as part of the CREPE II large area trans-iron cosmic ray experiment. These detectors consisted basically of a

sheet of film in optical contact with a transparent dielectric layer of uniform thickness which acts as a Cerenkov radiator. A charged particle with $\beta > 0.68$, incident from the radiator side, will illuminate an area on the film whose edge has the shape of a conic section. An analysis of the shape of the image appearing on the film will yield a measure of the velocity of the particle. Current film sensitivities limit these detectors to use with $Z \geq 60$ particles, and although theoretically capable of providing a charge measurement, the uncertainty in the film's response creates a considerable uncertainty in the charge estimates available from these fast film Cerenkov detectors. Therefore, the principle role of these detectors is that of determining the velocity.

CREPE II yielded a total of 64 events with $Z \geq 50$ (as determined by the plastic and emulsion measurements). For 27 of these events, fast film Cerenkov detector data were obtained. For the other events, the fast film Cerenkov detector layer either suffered flight damage, damage in processing, or has not yet been processed. Of the 27 events, 10 had Cerenkov images which have yielded velocity estimates that correspond well with the plastic and emulsion "thick stack" velocity estimates. The remaining 17 events were either below the charge or the velocity threshold of the detector. Thus, the fast film Cerenkov detectors provide a means of determining the velocity of particles with $Z \geq 60$ and $\beta > 0.68$.

CREPE II was the first flight with energy resolving capabilities, conducted with a large enough time-area exposure to allow an evaluation of the trans-iron cosmic ray energy spectrum. A maximum likelihood calculation using the 31 events with $Z > 60$ and kinetic energies/nuc between 600 and 1400 MeV/nuc (as measured in the plastics and emulsions, and corrected to the top of the atmosphere) yields an index of 6.5 ± 1.7 for the differential spectrum in total energy. (A similar calculation using only the 10 events for which fast film Cerenkov detector information is available gives a value of $8.8\ ^{+3.9}_{-3.5}$). These results are significantly different from 2.6, which is the accepted value of the index for primary cosmic ray H, He, L, and M nuclei. Existing pulsar acceleration models are unable to explain this difference.

When the $Z \geq 60$ charge data from CREPE II are combined with all of the $Z \geq 60$ data from previous experiments, the resulting spectrum shows the existence of elements with $Z \geq 83$, and a relative abundance peak at $Z \sim 76$-78. These observations, coupled with the apparent lack of any significant peak at $Z = 82$, strongly suggest that the ($Z \geq 60$) source spectrum is the product of an r-process nucleosynthesis.

When reasonable assumptions about the relative abundances at the source are made, slab model propagation calculations are generally inconsistent with the observed $Z \geq 60$ cosmic ray charge

spectrum (corrected to outside of the solar cavity). Unfortunately the present uncertainties in the understanding of the r-process preclude any further conclusions (e.g., regarding the exponential path length model) based on the current data.

REFERENCES

1. Nilsson, S. G., C. F. Tsang, A. Sobecyewski, Z. Sgymanski, S. Wycech, C. Gustafson, I. Lamm, P. Moller, and B. Nilsson, "On the Nuclear Structure and Stability of Heavy and Superheavy Elements", Nuclear Physics A131, 1 (1969)

2. Hess, V. F., "Uber Beobachtungen der Durchdringenden Strahlung bei Sieben Freiballonfahrten", Physik Z. 13, 1084 (1912)

3. Street, J. C. and E. C. Stevenson, "New Evidence for the Existence of a Particle of Mass Intermediate between the Proton and the Electron", Phys. Rev. 52, 1003 (1937)

4. Brode, R. B., "The Mass of the Mesotron", Rev. Mod. Phys. 21, 37 (1949)

5. Rochester, G. D. and C. C. Butler, "Evidence for the Existence of New Unstable Elementary Particles", Nature 160, 855 (1947)

6. Anderson, C. D., "The Positive Electron", Phys. Rev. 143, 491 (1933)

7. Johnson, T. H., "A Note on the Nature of the Primary Cosmic Radiation", Phys. Rev. 54, 385 (1938)

8. Freier, P., E. J. Lofgren, E. P. Ney, and F. Oppenheimer, "The Heavy Component of Primary Cosmic Rays", Phys. Rev. 74, 1818 (1948)

9. Bradt, H. L. and B. Peters, "Investigation of the Primary Cosmic Radiation with Nuclear Emulsions", Phys. Rev. 74, 1828 (1948)

10. Waddington, C. J., "The Composition of the Primary Cosmic Radiation", in Progress in Nuclear Physics, Vol. 8, O. R. Frisch, ed. (Pergamon Press, Inc., New York, New York, 1960)

11. Price, P. B., "Ultra-Heavy Cosmic Rays", Rapporteur talk given at the 12th International Conference on Cosmic Rays, Hobart Tasmania, August 16, 1971. Reprints available from the University of California, Berkeley, California, Space Sciences Laboratory Series 13, Issue 44. This review contains a good summary of the history of the trans-iron cosmic ray experiments.

12. Fleischer, R. L., P. B. Price, and R. M. Walker, "Solid-State Track Detectors: Applications to Nuclear Science and Geophysics" Ann. Rev. Nuc. Sci. 15, 1 (1965)

13. Fleischer, R. L., P. B. Price, R. M. Walker, M. Maurette, and G. Morgan, "Tracks of Heavy Primary Cosmic Rays in Meteorites", J. Geophys. Res. 72, 355 (1969)

14. Price, P. B., "Ultra-Heavy Cosmic Rays", op. cit. 11, p. 3

15. Fowler, P. H., R. A. Adams, V. G. Cowen, and J. M. Kidd, "The Charge Spectrum of Very Heavy Cosmic Ray Nuclei", Proc. Roy. Sec. A301, 39 (1967)

16. Fowler, P. H., V. M. Clapham, V. G. Cowen, J. M. Kidd, and R. T. Moses, "The Charge Spectrum of Very Heavy Cosmic Ray Nuclei", Proc. Roy. Soc. A318, 1 (1970)

17. Price, P. B., "Ultra Heavy Cosmic Rays", op. cit. 11, p. 3

18. These are all of the large area balloon flights that have been published.

19. Fowler, P. H., et. al., "The Charge Spectrum of Very Heavy Cosmic Ray Nuclei", op. cit. 16

20. Blanford, G. E. Jr., R. L. Fleischer, P. H. Fowler, M. W. Friedlander, J. Klarmann, J. M. Kidd, G. E. Nichols, P. B. Price, R. M. Walker, J. P. Wefel, and W. C. Wells, " Primary Cosmic Ray Particles With Z > 40", Acta Phys. dcad. Sci. Hun. 29 Suppl 1, 423 (1970)

21 Filz, R., "Large Area Cosmic Ray Experiments", to be published in the Proceedings of the "8th International Conference of Nuclear Photography and Solid-State Track Detectors, July 10-15, 1972, Bucharest, Romania

22. Binns, W. R., J. I. Fernandez, M. H. Israel, J. Klarmann, R. A. Mewaldt, "Observation of VH and VVH Cosmic Rays With an Ionization-Cerenkov Detector System", Vol. 1, Proc. 12th Int. Conf. on Cosmic Rays, Hobart, Tasmania (1971)

23. This estimate includes the CREPE II data assuming the CREPE II flight had an effective exposure time of 60 hours.

24. The charge measurements in the earlier experiments were subject to >> 4% uncertainties, and the principle values of some of these "measurements" changed by as much as 30% in successive reports. The value of 210 events with Z > 50 is based on the most recent published listing for each experiment.

25. Price, P. B., P. H. Fowler, J. M. Kidd, E. J. Kobetich, R. L. Fleischer, and G. E. Nichols, "Study of the Charge Spectrum of Extremely Heavy Cosmic Rays Using Combined Plastic Detectors and Nuclear Emulsions", Phys. Rev. D. 3 815 (1971)

26. Ibid., p 817

27. Ibid., p 819

28. Benton, E. V., private communication (1971)

29. Benton, E. V., private communication (1971)

30. Osborne, W. Z., private communication (1970)

31. Jelley, J. V., Cerenkov Radiation and Its Applications, (Pergamon Press, Inc., Los Angeles, Calif., 1958)

32. Badhwar, G. D., C. L. Deney, and M. F. Kaplon, private communication (1968)

33. Jelley, J. V., Cerenkov Radiation and Its Applications, op. cit. 31

34. Ibid.

35. See the discussion of the hyperbolic case ($\delta < \theta$) in Appendix

36. The author assisted G. D. Badhwar in this effort

37. Jelley, J. V., Cerenkov Radiation and Its Application, op. cit. 31, Jelley discusses all of the factors limiting the resolution of the Cerenkov angle in great detail

38. Tompkins, D. R., "Total Energy Loss and Cerenkov Emission from Monopoles", Phys. Rev. 138, B248 (1965)

39. Schwinger, J., "A Magnetic Model of Matter", Science 165, 757 (1969)

40. Thomas, G. B., Calculus and Analytic Geometry. (Addison-Wesley Publishing Company, Inc., Reading, Mass., 1962) p 500

41. Itek Corporation, Letter Report - Contract NAS-9-10727, May 14, 1971, Optical Systems Division, Itek Corporation, Lexington, Mass.

42. Hargrove, L. E., and J. S. Courtney-Pratt, "Some Photographic Studies of the Light Output of an Intracavity Modulated Gas Maser", J. of the Soc. of Mot. Pict. and T.V. Eng. 74, 1085 (1965)

43. Price, P. B., "Ultra-Heavy Cosmic Rays", op. cit. 11

44. Osborne, W. Z., private communication

45. As mentioned in the acknowledgements, all of the plastic scanning and measurements were accomplished in Price's group at the Space Sciences Laboratory of the University of California at Berkeley.

46. Longo, M. J., "Topical Conf. on High-Energy Collisions of Hadrons", CERN, Geneva, CERN 68-7, 1, 523 (1968)

47. Kaiser, T. B., J. R. Wayland and G. Gloeckler, "Production and Propagation of Particles with A>81 In the Galaxy", Technical Report # 72-008, Center for Theoretical Physics of the Dept. of Physics and Astronomy, University of Maryland, College Park, Maryland

48. Rudstam, G., "Spallation of Elements in the Mass Range 51-75", Phil. May. 46, 344 (1955)

49. Rudstam, G., "Systematics of Spallation Yields", Z. Naturforschung 21A, 1027 (1966)

50. Waddington, C. J., "The Composition of the Primary Cosmic Radiation", op. cit. 10

51. Barkas, W. H., and M. J. Berger, Tables of Energy Losses and Ranges of Heavy Charged Particles, NASA SP-3013, (1964). National Aeronautics and Space Administration, Wash., D. C.

52. Fermi, E., and B. Rossi, Rend. R. Accad. Naz. Lincei 17, 346 (1933)

53. The mean mass per nucleon for Z>26 varies only by a few MeV/nuc from 931 MeV/nuc which is the approximate value at Z=26. For the purposes of the calculations presented here, the value of 931.1 MeV/nuc will be adapted for all nuclei.

54. Parker, E. N., Interplanatary Dynamical Processes, (Vol. VIII, Monographs and Texts in Physics and Astronomy, edited by R. E. Marshak) (John Wiley & Sons, Inc., New York, 1963)

55. Goldstein, M. L., R. Ramaty, and L. A. Fisk, "Interstellar Cosmic Ray Spectra from the Nonthermal Radio Background from 0.4 to 400 MHz", Phys. Rev. Letters 24, 1193 (1970)

56. Silberberg, R., "Cosmic-Ray Modulation in the Solar System and in Interstellar Space", Phys. Rev. 148, 1247 (1966)

57. Bhatia, V. S., S. Biswas, V. S. Chohan, N. Durgaprasad, S. D. Pabbi, and S. Paruthi, "Solar Modulation of Cosmic Ray Heavy Nuclei (Z = 10-28)", Vol. 2, Proc. 12th Int. Conf. on Cosmic Rays, Hobart, Tasmania (1971)

58. Rao, U. R., "Solar Modulation of Galactic Cosmic Radiation", Sp. Sci. Rev. 12, 719 (1972)

59. Ibid.

60. Fowler, P. H., V. M. Clapham, V. G. Cowen, J. M. Kidd, and R. T. Moses, "The Charge Spectrum of Very Heavy Cosmic Ray Nuclei, op. cit. 16

61. O'Sullivan, D., P. B. Price, E. K. Shirk, P. H. Fowler, J. M. Kidd, E. J. Kobetich, and R. Thorne, "High Resolution Measurements of Slowing Cosmic Rays from Fe to U", Phys. Rev. Letters 26, 463 (1971)

62. Cameron, A. G. W., "The Role of Neutron Stars in the Acceleration of Cosmic Rays", Proceedings of Conf. on Isotopic Composition of Primary Cosmic Rays, P. M. Dauber, ed., Danish Space Research Inst., Lyngby, Denmark (1971)

63. Cameron, A. G. W., "Supernova Explosions", Proceedings of Conf. on Isotopic Composition of Primary Cosmic Rays, P. M. Dauber, ed., Danish Space Research Inst. (1971)

64. Burbidge, M. E., G. R. Burbidge, W. A. Fowler, and F. Hoyle, "Synthesis of the Elements in Stars", Rev. of Mod. Phys. 29, 547 (1957)

65. Seeger, P. A., W. A. Fowler, and D. D. Clayton, Nucleosynthesis of Heavy Elements by Neutron Capture" Ap. J. Suppl. 11, 121 (1964)

66. Seuss, H. E., and H. C. Urey, "Abundances of the Elements", Revs. Mod. Phys. 28 53 (1956)

67. Seeger, P. A., W. A. Fowler, and D. D. Clayton, "Nucleosynthesis of Heavy Elements by Neutron Capture", op. cit. 65

68. Hoyle, F., and W. A. Fowler, "On the Abundance of Uranium and Thorium in Solar System Material", Isotopic and Cosmic Chemistry, eds. H. Craig, S. Miller, and G. J. Wasserburg (North-Holland Publishing Co., Amsterdam 1963)

69. Clayton, D. D., "Nucleosynthesis of the Isotopes of Lead", in Origin and Distribution of the Elements, (Pergamon Press, Ltd., Oxford, England, 1968)

70. Schramm, D. N., and W. A. Fowler, "Synthesis of Superheavy Elements in the r-process" Nature 231, 103 (1971)

71. Waddington, C. J., "The Composition of the Primary Cosmic Radiation", op. cit. 10

72. Shapiro, M. M., R. Silberberg, C. H. Tsao, "The Distribution Function of Cosmic-Ray Path Lengths", Acta Phys. Acad. Sci. Hung. 29, Suppl. 1, 470 (1970)

73. Ibid, p 470

74. Ginzburg, V. L., and S. I. Syrovatskii, The Origin of Cosmic Rays, (The Macmillan Company, New York, New York, 1964) p 284

75. Ibid, p 128

76. Silberberg, R., and C. H. Tsao, "Partial Cross Sections in High-Energy Nuclear Reactions For Targets Heavier Than Nickel", Laboratory for Cosmic Ray Physics, Naval Research Laboratory, Wash. D.C. 20390

77. Shapiro, M. M., R. Silberberg, and C. H. Tsao, "Transformation of Cosmic-Ray Nuclei in Space", Acta Phys. Acad. Sci. Hung. 29, Suppl. 1, 463 (1970)

78. Ramaty, R., and R. E. Lingenfelter, "Cosmic-Ray Deuterium and Helium-3 of Secondary Origin and the Residual Modulation of Cosmic-Rays", Ap. J. 155, 587 (1969)

79. Gloeckler, G., and J. R. Jokipii, "Physical Basis of the Transport and Composition of Cosmic Rays in the Galaxy", Phys. Rev. Letters 22, 1448 (1969)

80. Shapiro, M. M., R. Silberberg, and C. H. Tsao, "Transformation of Cosmic Ray Nuclei in Space", op. cit. 77

81. Ibid.

82. Barkas, W. H., and M. J. Berger, Tables of Energy Losses and Ranges of Heavy Charged Particles, NASA SP-3013, (1964), National Aeronautics and Space Administration, Wash. D. C.

83. Cowsik, R., Yash Pal, S. N. Tandon, R. P. Verma, "Spectra of Heavy and Super-Heavy Nuclei in Steady State", Acta Phys. Acad. Sci. Hung. 29, Suppl. 1, 439 (1970)

84. Cowsik, R., Yash Pal, S. N. Tandon, and R. P. Verma, "Steady State of Cosmic-Ray Nuclei - Their Spectral Shape and Path Length at Low Energies", Phys. Rev. 158, 153 (1967)

85. Shapiro, M. M., R. Silberberg, C. H. Tsao, "Transformation of Cosmic-Ray Nuclei in Space", op. cit. 77

86. Shapiro, M. M., R. Silberberg, and C. H. Tsao, "The Distribution Function of Cosmic-Ray Path Lengths", op. cit. 72

87. Shapiro, M. M., R. Silberberg, and C. H. Tsao, "Transformation of Cosmic-Ray Nuclei in Space", op. cit. 77

88. Mewaldt, R. A., R. E. Turner, M. W. Friedlander, and M. H. Isreal, "The Propagation of Very Heavy Primary Cosmic Ray Particles", Acta Phys. Acad. Sci. Hung. 29, Suppl. 1, 432 (1970)

89. Ginzburg, V. L., and S. I. Syrovatskii, The Origin of Cosmic Rays, op. cit. 74, p 119

90. Ibid, p 303

91. Ibid, p 333

92. Ibid, p 333

93. This compilation includes in addition to data from CREPE II, data from the following flights mentioned in Chapter I, Texas I-IV, Barndoor I-III, and Sioux Falls I.

94. Seeger, P. A., W. A. Fowler, and D. D. Clayton, "Nucleosynthesis of Heavy Elements by Neutron Capture", op. cit. 65

95. Hewish, A., S. J. Bell, J. D. H. Pilkington, P. F. Scott, and R. A. Collins, "Rapidly Pulsating Radio Source", Nature 217, 709 (1968)

96. Large, M. I., A. E. Vaughan, and B. Y. Mills, "A Pulsar Supernova Association?", Nature 220, 340 (1968)

97. Kulsrad, R. M., J. P. Ostriker and J. E. Gunn, "Acceleration of Cosmic Rays in Supernova Remnants", Phys. Rev. Letters 28, 636 (1972)

98. Ibid, p 639

99. Gold, T., "Rotating Neutron Stars as the Origin of the Pulsating Radio Sources", Nature 218, 731 (1968)

100. Nather, R. E., B. Warner, and M. Macfarlane, "Optical Pulsations in the Crab Nebula Pulsar", Nature 221, 527 (1969), and Duthie, J. G., C. Sturch, H. B. Richer, and P. Rodney, "Optical Studies of Pulsar NP0532", Science 163, 1320 (1969)

101. Grewing, M., and H. Heintzman, "Constant-Cross-Field Acceleration, a Mechanism for the Generation of Cosmic Rays by Strong Low-Frequency Electromagnetic Waves", Phys. Rev. Letters 28, 381 (1972)

102. Kulsrud, R. M., J. P. Ostriker, and J. E. Gunn, "Acceleration of Cosmic Rays in Supernova Remnants", op. cit. 97

103. Weisskopf, M. D., R. Novick, R. Berthelsdorf, and R. Linke, "Detection of X-ray Polarization from the Crab Nebula", Presented at the 1972 Spring Meeting of the A.P.S. in Wash., D. C., 24-27 April 1972

104. Kulsrud, R. M., J. P. Ostriker, and J. E. Gunn, "Acceleration of Cosmic Rays in Supernova Remnants", op. cit. 97, p 637

105. Cowsik, R., and P. B. Price, "Origins of Cosmic Rays", Physics Today 24, #10, p 30 (Oct., 1971)

106. Mood, A. M., and F. A. Graybill, Introduction to the Theory of Statistics (McGraw-Hill Book Company, Inc., New York, New York, 1963)

107. This suggestion was first made by W. Z. Osborne in a private communication to the author. (1972)

APPENDIX A

CERENKOV IMAGE GEOMETRY FOR $\delta \leq \theta$

1. $\delta = \theta$ - PARABOLA

Chapter II contains a detailed discussion of the Cerenkov image geometry for the case of $\delta > \theta$ where it was shown that the image had the shape of an ellipse. When $\delta = \theta$ the image edge will be a parabola, and the general equation is given by:

$$Y^2 = 4CX \tag{A-1}$$

Using geometrical arguments similar to those employed in the elliptical case, one finds that:

$$C = \frac{T}{2} \tan \delta \tag{A-2}$$

where T is the thickness of the radiator. The polar equation of the parabola analogous to equation (21) in Chapter II is given by:

$$R' (\delta, T, \phi') = \left((X - X_o)^2 + 4CX \right)^{\frac{1}{2}} \tag{A-3}$$

where X is given by:

$$X (\phi') = \frac{X_o \tan^2 \phi' + 2C \pm 2(X_o C \tan^2 \phi' + C^2)^{\frac{1}{2}}}{\tan^2 \phi'} \tag{A-4}$$

and X_o is:

$$X_o = T \csc (2\delta) \tag{A-5}$$

All of the photon density relations given in Chapter II are valid for the parabolic case when equation (A-3) is used for R' (ϕ'). The upper sign in equation (A-4) is used for $\frac{\pi}{2} \leq \phi' < -\frac{\pi}{2}$ and the lower sign is used in the remaining two quadrants. The argument for this sign choice is identical to the one presented in Chapter II for the elliptical case.

2. $\delta < \theta$ HYPERBOLIC

When $\delta < \theta$, the problem is complicated by the fact that all of the Cerenkov light does not fall on the lower film sheet (see Figure A-1a). The resulting image in the lower film sheet is shown in Figure A-1b. In this case, the outer edge of the image is the hyperbola formed by the intersection of the Cerenkov cone and the film plane. The asymptotes of the hyperbola are found to be:

$$a = \frac{T}{2} \left(\cot (\delta - \theta) - \cot (\delta + \theta)\right) \tag{A-6}$$

and:

$$b = a \left(1 - \frac{\cos^2 \delta}{\cos^2 \theta}\right)^{\frac{1}{2}} \tag{A-7}$$

where T is the thickness of radiator. The polar equation $R'(\phi')$ for this hyperbola is given by:

$$R' (\delta, \theta, T, \phi') = \left((X + X_o)^2 - b^2 \left(1 - X^2/a^2\right)\right)^{\frac{1}{2}} \tag{A-8}$$

where:

$$X = \frac{-X_o \tan^2\phi' - b\left(\left(\frac{X_o^2}{a^2} - 1\right)\tan^2\phi' + b^2/a^2\right)^{\frac{1}{2}}}{\tan^2\phi' - b^2/a^2} \quad , \qquad \text{(A-9)}$$

and:

$$X_o = T\,(\cot(\delta) - \cot(\delta + \theta)) + a \; . \qquad \text{(A-10)}$$

The upper sign in equation (A-9) applies for $\frac{\pi}{2} \geq \phi' \geq \frac{\pi}{2}$ and the lower sign applies for $\frac{3\pi}{2} \geq \phi' > \frac{\pi}{2}$. For $\tan\phi' = \pm \frac{b}{a}$ (i.e., parallel to the asymptotes) when $\frac{3\pi}{2} > \phi > \frac{\pi}{2}$, $R'(\delta, \theta, T; \phi') \to \infty$. Since the photon density is inversely proportional to R', the photon density falls to 0 for these two angles and, is 0 for $\tan^{-1}\frac{b}{a} \geq \phi' \geq \tan^{-1}(-\frac{b}{a})$. This gives the image shape shown in Figure A-1b. As in the parabolic case, all of the photon density relations from Chapter II are valid when equation (A-8) is used for $R'(\phi')$. The appropriate photon iso-density curves are shown in Figure A-1b.

The image in the upper sheet is shown in Figure A-1c where the asymptotes are parallel to those occurring in the lower sheet ($\frac{a}{b} = \frac{a''}{b''}$). The polar equation of the hyperbola in Figure A-1c is given by:

$$R''(\phi'') = \left(X''^2 + b''^2\left(\frac{X''^2}{a''^2} - 1\right)\right)^{\frac{1}{2}} , \qquad \text{(A-11)}$$

where we have used the double prime (") to indicate coordinates in the upper sheet. X" is given by:

$$X'' = \frac{\tan\phi'' + (\tan^2\phi'' + 4\,b''^2/a''^2)^{\frac{1}{2}}}{2b''^2/a''^2} \qquad \text{(A-12)}$$

FIGURE A-1

HYPERBOLIC IMAGE GEOMETRY

a. This sketch demonstrates that for $\delta < \theta$, all of the light does not fall on the lower sheet, and that the upper sheet does receive some Cerenkov light.

b. This drawing illustrates the image geometry as observed in the lower sheet, and the corresponding iso-density contours (dotted lines) similar to those presented in Figure 9 of Chapter II for the elliptical case.

c. This represents the image geometry and iso-density coutours in the upeer sheet for the hyperbolic case.

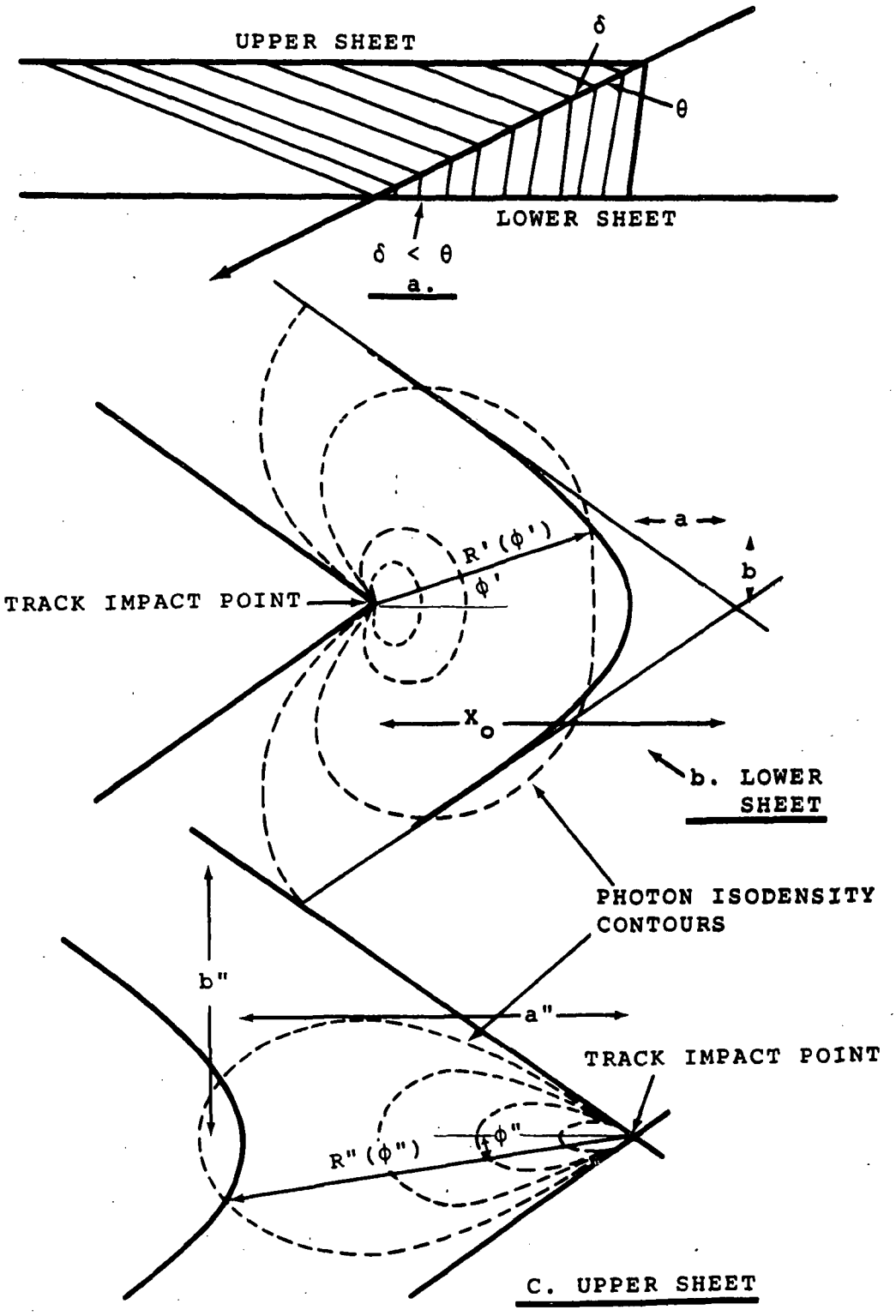
UPPER SHEET
δ
θ
LOWER SHEET
δ < θ
a.
a
b
R'(φ')
φ'
TRACK IMPACT POINT
X_o
b. LOWER SHEET
PHOTON ISODENSITY CONTOURS
b"
a"
TRACK IMPACT POINT
R"(φ")
φ"
C. UPPER SHEET

FIGURE A-1

with:

$$a'' = T(\cot(\theta-\delta) + \cot\delta) \ , \tag{A-13}$$

and:

$$b'' = a'' \left(1 - \frac{\cos^2\delta}{\cos^2\theta}\right)^{\frac{1}{2}} \ . \tag{A-14}$$

To find the photon iso-density curves in the upper sheet, one must find the relation for $\frac{r\ dr\ d\phi}{r''\ dr''\ d\phi''}$ where the unprimed coordinates are in the plane normal to the track. Then, as in Chapter II:

$$P''(r'', \phi'') = \frac{r\ dr\ d\phi}{r''\ dr''\ d\phi} \ P(r, \phi)$$

where $P(r, \phi) = \frac{P}{2\pi r} \sin\theta \cos\theta$, and P is given by equation (5) in Chapter II. $\frac{r\ dr\ d\phi}{r''\ dr''\ d\phi''}$ is given by:

$$\frac{r\ dr\ d\phi}{r''\ dr''\ d\phi''} = \sin^2\delta \ \frac{(-\cos(\frac{1}{2}\cos^{-1}D_o)}{B_o^2\ (1-D_o^2)^{\frac{1}{2}}\ [\sin^2\theta - \sin^2(\frac{1}{2}\cos^{-1}D_o)]^{\frac{1}{2}}} \ x$$

$$[2B_o(a'' - T\cot\delta) + 2A_o\ T\csc(\theta-\delta)\ \frac{(X''\ \frac{b''^2}{a''^2} - 1) - T\cot\delta}{b_o^{\frac{1}{2}}}]x$$

$$[\frac{a''}{2b''^{\frac{1}{2}}}\ (\sec^2\phi'' - \frac{\tan\phi''\ \sec^2\phi''}{(\tan^2\phi'' + 4\ b''^4/a''^2)^{\frac{1}{2}}})] \ , \tag{A-15}$$

where:

$$A_o = 2X\ (a'' - T\cot\delta) + T^2\ (\csc^2\delta + \csc^2(\theta-\delta)) - a^2 \ , \tag{A-16}$$

and:

$$B_o = 2T\ \csc\ (\theta-\delta)\ [X''^2(\frac{b''^2}{a''^2} - 1) - 2TX''\ \cot\delta + T^2\csc^2\delta], \tag{A-17}$$

and:

$$b_o = \frac{B_o}{2T \csc(\theta-\delta)} \quad . \tag{A-18}$$

The photon iso-density curves are plotted in Figure A-1c.

The photon density in the upper sheet for $\delta > 10^\circ$ will be below the film sensitivity threshold outside of the ionization spot region for all values of $\theta < 47.6^\circ$ (i.e., the Cerenkov angle for $\beta = 1$ with the index of refraction ~ 1.484) and all $Z < 100$. Thus, one would not expect to find any Cerenkov images in the upper film sheets with the current limitations in film sensitivity.

Page intentionally left blank

APPENDIX B

EASTMAN KODAK 2485 FILM CHARACTERISTICS

Eastman Kodak 2485 is an extremely high speed panchromatic recording film with an extended red sensitivity. The relative spectral sensitivity of the film is plotted in Figure B-1. The film grains actually have a short wavelength sensitivity that extends below .25 μm, but the photographic gel containing the grains has a transmission cut-off at ∿ .275 μm.

The exposure versus density curve obtained from the EK 2485 flown on CREPE II has been plotted in Figure 10 of Chapter II. This curve displays the speed and high contrast possessed by the film. The contrast is so high that the film "saturates" (achieves maximum photographic density) when the exposure is increased by ∿ a factor of 10 over the absolute threshold level.

The film's grain structure is quite coarse. The undeveloped grains are ∿ 0.5 μm in diameter, and the developed grains are from 2-5 μm in diameter depending upon the exposure level. The grains are suspended in an aqueous photographic gel and the entire photographic emulsion layer is ∿ 12 μm thick. The undeveloped grain density (grains/cm^3) is a function of the depth in the gel and gives the film a more and a less sensitive side (i.e., the surface with the higher grain density is more sensitive).

FIGURE B-1

RELATIVE SPECTRAL SENSITIVITY OF EK 2485

This plot is based on the Eastman Kodak data regarding the spectral sensitivity of their 2485 high speed recording film. The lower wavelength cut-off is actually determined by the transmission cut-off of the photographic gel, and not the actual film sensitivity.

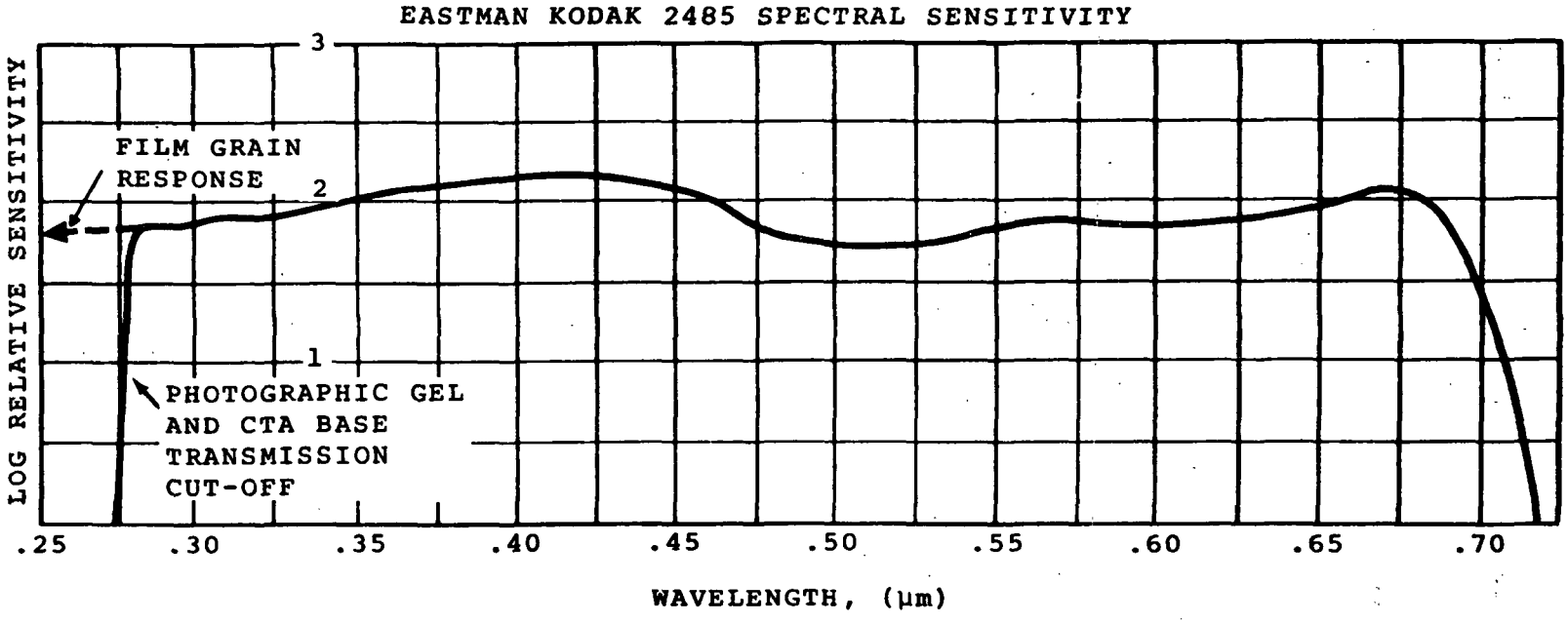
EASTMAN KODAK 2485 SPECTRAL SENSITIVITY
LOG RELATIVE SENSITIVITY
3
2
1
FILM GRAIN RESPONSE
PHOTOGRAPHIC GEL AND CTA BASE TRANSMISSION CUT-OFF
.25
.30
.35
.40
.45
.50
.55
.60
.65
.70
WAVELENGTH, (μm)

FIGURE B-1

The film can withstand moderate temperature excursions without loss of speed, and can be placed in a vacuum for extended periods with no ill effects. Unfortunately, the film suffers from extreme pressure sensitivity, and will mark if fingernails come into contact with the film surface during handling.

The EK 2485 film employed on CREPE II was mounted on a 0.004" estar base with an opaque "anti-halation" layer between the emulsion and the base. All of the details of this film are discussed in KODAK Publication No. P-94, which is available from Eastman Kodak, Rochester, New York.

APPENDIX C

EVALUATION OF THE ENERGY SPECTRUM

1. THE MAXIMUM LIKELIHOOD METHOD

The method of maximum likelihood is generally considered to the best statistical approach to a measurement problem when the functional relationship between the measured quantity and the desired parameter is known. In our case, we wish to evaluate the form of the energy spectrum in terms of the individually measured kinetic energies.

To begin, we assume that the spectrum has the functional form:

$$dN(E) = K\ (E + \Psi\ m_{nuc})^{-\nu}\ dE \qquad \text{(C-1)}$$

where $\Psi = 0$ is a power law in kinetic energy per nucleon, and $\Psi = 1$ is a power law in total energy per nucleon (i.e., E is the kinetic energy per nucleon, and $E + m_{nuc} = w$, the total energy per nucleon). The method of maximum likelihood requires that the functional form be normalized. Assuming that our measurements cover some range of kinetic energies from E_o to E_1, the normalized function, n(E), is given by:

$$n(E) = \frac{(\nu-1)\ (E + \Psi\ m_{nuc})^{-\nu}}{(E_o + \Psi\ m_{nuc})^{-\nu+1} - (E_1 + \Psi\ m_{nuc})^{-\nu+1}} \ . \qquad \text{(C-2)}$$

The likelihood function, L, is written:

$$L = \prod_{i}^{N} n(E_i) \quad , \tag{C-3}$$

where N is the number of events with measured kinetic energy per nucleon between E_o and E_1. Substituting equation (C-2) into (C-3), one finds:

$$L = \frac{(\nu-1)^N}{\left[(E_o + \Psi\, m_{nuc})^{-\nu+1} - (E_1 + \Psi\, m_{nuc})^{-\nu+1}\right]^N} \exp\left[-\nu \sum_{i}^{N} \ell n(E_i+\Psi m_{nuc})\right] \tag{C-4}$$

In the limit as $N \to \infty$, L approaches a normal distribution in ν, and the most likely estimate of ν is that value which makes L a maximum.[106] Since ℓn L is maximum when L is maximum, we can examine ℓn L to obtain the most likely estimate of ν.

$$\ell nL = N\, \ell n \left(\frac{\nu-1}{(E_o+\Psi m_{nuc})^{-\nu+1} - (E_1+\Psi m_{uuc})^{-\nu+1}}\right) - \nu \sum_{i}^{N} \ell n(E_i+\Psi m_{nuc})^{-\nu+1}. \tag{C-5}$$

Figure C-1 contains a plot of ℓn L versus ν for both $\Psi = 0$ and $\Psi = 1$. (ℓn L is plotted on an arbitrary relative scale) These curves were calculated from the kinetic energies per nucleon at the top of the atmosphere for the 31 events contained in Table 3 (Chapter III) with $Z > 60$ and $600 \leq E \leq 1400$ MeV/nuc (i.e., E_o = 600 MeV/nuc and E_1 = 1400 MeV/nuc). For the case of $\Psi = 1$ (power law in <u>total</u> energy per nucleon), the maximum in ℓn L occurred at $\nu \sim 6.5$. To evaluate the precision of this estimate, we note that

even with 31 events, L closely approximates a normal distribution. For a normal distribution, the standard deviation, S (i.e., the standard error), is the difference from the mean of the value of ν for which L has decreased by a factor of $e^{\frac{1}{2}}$. In our case, since ℓn L has been plotted, the standard deviation is $S = 6.5 - \nu_{.5}$, where $\nu_{.5}$ is the value of ν when ℓn L decreases from the maximum by $\frac{1}{2}$. From Figure C-1, one finds $S \sim 1.7$.

The curve for $\Psi = 0$ in Figure C-1 has a maximum (at $\nu_{\Psi=0} \sim 3.1 \pm 0.81$) of ℓn L = 1.28 which is considerably less than the ($\nu \sim 6.5 \pm 1.7$) maximum of ℓn L = 4.39 for $\Psi = 1$. This implies that the data fit a power law in total energy per nucleon ($\Psi = 1$), considerably better than a power law in kinetic energy per nucleon. A similar calculation for the 8 fast film Cerenkov detector events with $600 \leq E \leq 1400$ MeV/nuc at the top of the atmosphere, yields a value of $\nu \sim 8.8 \pm \frac{3.9}{3.5}$ for $\Psi = 1$.

In conclusion, a maximum likelihood calculation for the 31 CREPE II events with $Z > 60$ and $600 \leq E \leq 1400$ MeV/nuc, indicates that between these kinetic energies per nucleon the energy spectrum is best fit by a power law in <u>total</u> energy, w, with index 6.5 ± 1.7.

FIGURE C-1

LIKELIHOOD CURVES FOR THE INDEX OF THE DIFFERENTIAL ENERGY SPECTRUM OF THE Z > 60 CREPE II DATA

This plot represents the 2 likelihood curves based on the 31 events indicated on Table 3 in Chapter III, of the index of the differential energy spectrum of the Z > 60 CREPE II data. The curves for both a power law in total energy and a power law in kinetic energy are given. Both plots are drawn to the same arbitrary log scale.

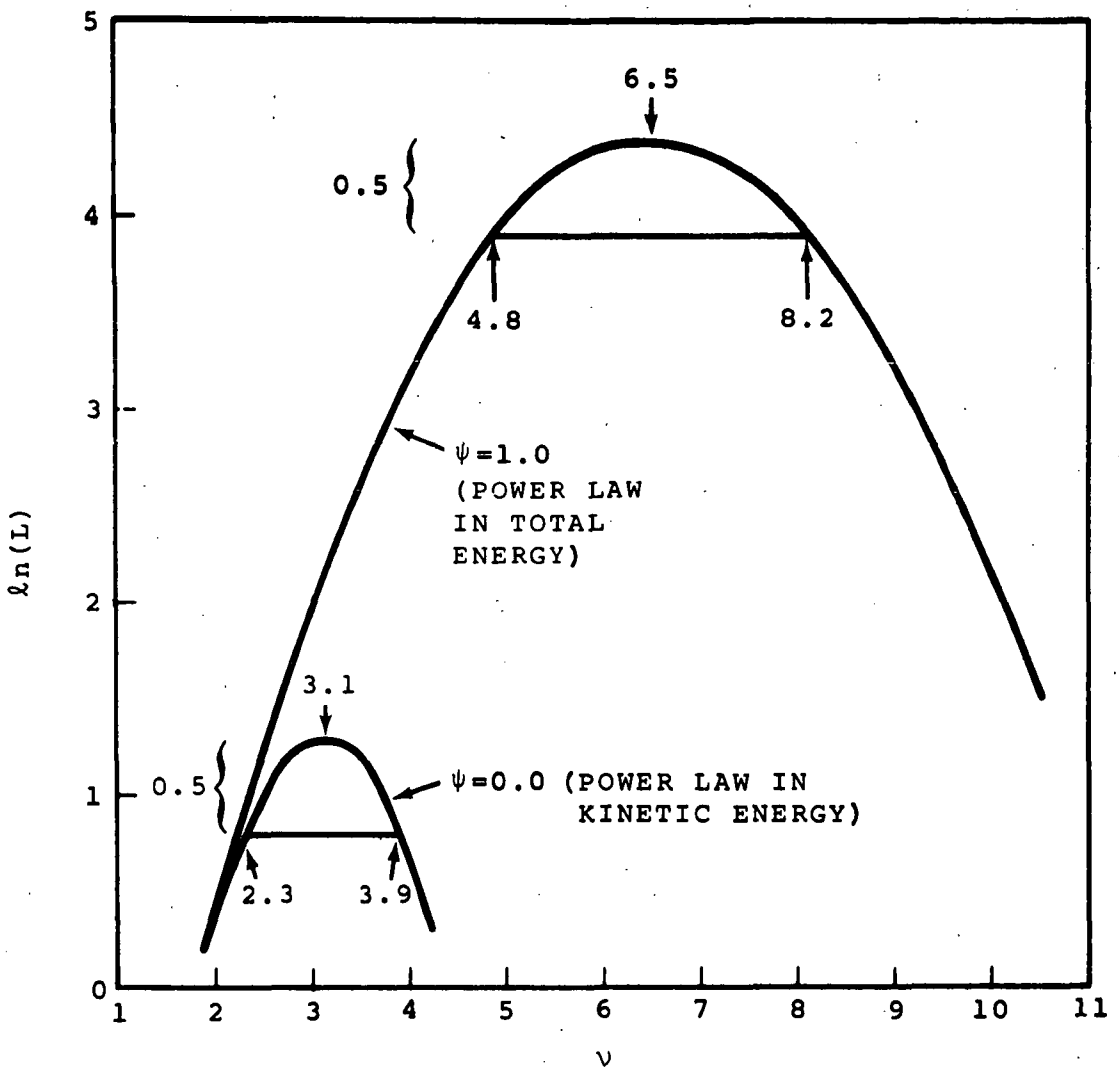
6.5
0.5
4.8
8.2
ψ=1.0
(POWER LAW
IN TOTAL
ENERGY)
3.1
0.5
ψ=0.0 (POWER LAW IN
KINETIC ENERGY)
2.3
3.9
ℓn(L)
ν
0
1
2
3
4
5
6
7
8
9
10
11

FIGURE C-1

2. UNCERTAINTIES IN THE ENERGY SPECTRUM

The previous section dealt with a maximum likelihood calculation of the spectral index from the measured energies. However, no mention was made of the uncertainty in the determination of the individual energies. As listed in Table 3, the experiment provides us with a measure of β and $\delta\beta$, the associated uncertainty, which is related to δE by the expression:

$$\frac{\delta E}{E} = (\gamma+1)\ \gamma\ \frac{\delta E}{\beta} \qquad \text{(C-6)}$$

where $\gamma = (1 - \beta^2)^{-\frac{1}{2}}$. The plastics and emulsions actually provide range estimates (and uncertainties) which have been translated into β and $\delta\beta$. The appropriate δE's propagated to the top of the atmosphere have been included in Table 3.

To examine the effect of δE on the uncertainty in the estimate of ν, consider the differential spectrum plotted in Figure C-2. This spectrum was compiled by grouping the 31 events in Table 3 with $Z > 60$ and kinetic energies between 600 and 1400 MeV/nuc, into bins of 100 MeV/nuc. (The two events between 1100 and 1400 MeV/nuc have been combined into one 300 MeV/nuc bin.) For the j^{th} bin, the principle data point was plotted at the mean kinetic energy per nucleon for the events in that bin:

$$E_j = \sum_{i=1}^{n_j} \frac{E_i}{n_i} \qquad \text{(C-7)}$$

where n_j is the number of events on the j^{th} bin, and the E_i's are the individual kinetic energies per nucleon of the n_j events in the j^{th} bin. The uncertainty in this point is given by:

$$\delta E_j = \left(\sum_{i=1}^{n_j} \left(\frac{\delta E_j}{\delta E_i} \right)^2 \delta E_i{}^2 \right)^{\frac{1}{2}} \qquad \text{(C-8)}$$

where δE_i is uncertainty in the kinetic energy per nucleon of the i^{th} point. Differentiating equation (C-7), one finds:

$$\delta E_j = \frac{1}{n_j} \left(\sum_{i=1}^{n_j} \delta E_i{}^2 \right)^{\frac{1}{2}} \qquad \text{(C-9)}$$

Since the uncertainties in the kinetic energy per nucleon for all of the events in Table 3 are not symmetric, the values of δE_j are not in general symmetric.

The uncertainty in the number of events in each bin obeys the binomial statistics of 31 total events. The standard deviation, S_j, for the number of events in the j^{th} bin is given by:

$$S_j = \frac{\left[n_j \, (1 - n_j/31) \right]^{\frac{1}{2}}}{\Delta E_j} \qquad \text{(C-10)}$$

where ΔE_j is the bin size of the j^{th} bin. For our purposes we will adopt a slightly more liberal (gaussian) error and assume that:

$$S_j = \frac{n_j{}^{\frac{1}{2}}}{\Delta E_j} \qquad \text{(C-11)}$$

FIGURE C-2

DIFFERENTIAL ENERGY SPECTRUM FROM CREPE II Z > 60 DATA

This plot contains the error ellipses constructed around the data points which have been assembled into 100 MeV/nuc bins (1100-1400 MeV/nuc has been combined into one 300 MeV/nuc bin). It can be seen that the flattest spectrum (in total energy) that can be simultaneously drawn through all of the error ellipses has an index of $\nu \sim 5.39$.

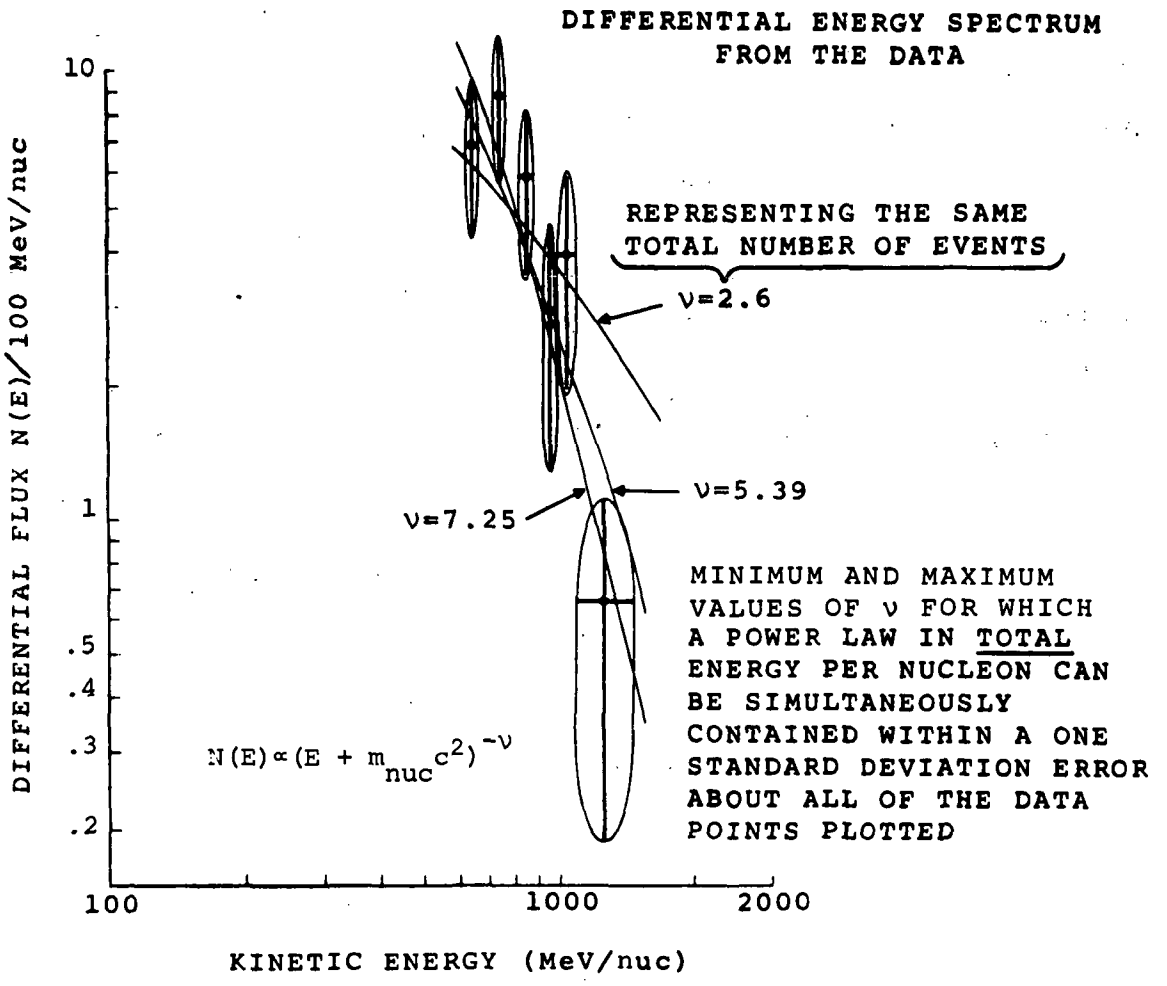
DIFFERENTIAL ENERGY SPECTRUM
FROM THE DATA
REPRESENTING THE SAME
TOTAL NUMBER OF EVENTS
ν=2.6
ν=5.39
ν=7.25
MINIMUM AND MAXIMUM
VALUES OF ν FOR WHICH
A POWER LAW IN TOTAL
ENERGY PER NUCLEON CAN
BE SIMULTANEOUSLY
CONTAINED WITHIN A ONE
STANDARD DEVIATION ERROR
ABOUT ALL OF THE DATA
POINTS PLOTTED
N(E)∝(E + m_nuc c^2)^-ν
DIFFERENTIAL FLUX N(E)/100 MeV/nuc
10
1
.5
.4
.3
.2
100
1000
2000
KINETIC ENERGY (MeV/nuc)

FIGURE C-2

To proceed, we construct ellipses about the error bars in Figure C-2 which contain the domain of probable values for each point. One then asks what are the maximum and minimum values of ν for which a power law in total energy per nucleon with spectral index $-\nu$, can be drawn, and simultaneously intersect all of the ellipses. As shown in Figure C-2, these values are $\nu = 7.25$ and $\nu = 5.39$, respectively. The curve with $\nu = 2.6$, representing the same total number of events between 600 and 1400 MeV/nuc (31), has also been included in Figure 2-C.

This curve plotting exercise tends to corroborate the result of the maximum likelihood calculation presented above. Thus, based on the 31 events from CREPE II with $Z > 60$, and $600 \leq E \leq 1400$ MeV/nuc, it would appear that the energy spectrum of the heavier trans-iron cosmic rays is significantly steeper than the $\nu = 2.6$ spectrum attributed to the sub-iron cosmic rays.

APPENDIX D

IMPROVEMENTS TO THE FAST FILM CERENKOV DETECTOR DESIGN

1. USING THE FILM BASE AS THE RADIATOR

Eastman Kodak has recently succeeded in placing the 2485 film emulsion on a CTA (Cellulose Triacetate) base. This base is non-scintillating and has a uniform index of refraction, which makes it a suitable Cerenkov radiator. Some of the CTA backed 2485 was produced with no anti-halation layer, and with the direction of maximum film sensitivity toward the base. This material is ideal for use as a fast film Cerenkov detector with the film base employed as the Cerenkov radiator.

Currently, the available CTA base thicknesses range from 65 μm to 200 μm. One might consider flying several thicknesses in the same detector stack,[107] and then compare the images, selecting the optimum detector thickness to analyze each event.

Under any circumstances, this form of the fast film Cerenkov detector should be free of the disassembly problems encountered in the version flown on CREPE II.

2. EXTENDING THE SPECTRAL SENSITIVITY OF THE DETECTOR

Since the Cerenkov photon output (equation (5) of Chapter II) is proportional to $(\frac{1}{\lambda_2} - \frac{1}{\lambda_1})$, where λ_1 and λ_2 are the lower and upper wavelength cut-offs respectively, if one could extend the spectral sensitivity of the detector, the current charge threshold limitation of $Z \sim 55$, could be lowered.

The EK 2485 film grain sensitivity already extends into the ultra-violet, past the transmission cut-offs for the photographic gel and the CTA base. If one could find a replacement for the gel that had a shorter cut-off wavelength, and a base (e.g., thin quartz glass plates) that also had a shorter ultra-violet cut-off, then, the resulting fast film Cerenkov detector would have a lower charge threshold, and the image sizes could be made larger (yielding more accurate measurements) through the use of a thicker radiator layer.

Both of the improvements suggested in this appendix will have no effect on the form of the analysis of the Cerenkov images as described in Chapter III.

APPENDIX E

THE CREPE II BALLOON FLIGHT

The *CREPE II* gondola weighed over 1400 pounds and contained a $\sim$ 22.3 m^2 detector array whose detailed stack configuration is given in Figure 12 of Chapter III. The gondola was launched on a 20 x 10^6 ft^3 polyethelene balloon from Fleming Field in South Saint Paul, Minnesota at $\sim$ 1915 CDT on September 4, 1970. The ascent was normal, and the balloon reached a float altitude $\gtrsim$ 130,000 ft (3.0 gm/cm^2 of residual atmosphere) by $\sim$ 2145, at which time the upper detector layer was shifted 1" with respect to the remainder of the stack. The time versus altitude graph is presented in Figure E-1.

The flight was relatively uneventful until $\sim$ 1200 CDT on September 6, when, because the flight trajectory was approaching rough terrain, an attempt was made to terminate the flight by command. This attempt failed due to a malfunction of several explosive bolts in the cut-down fitting. The balloon was then tracked with the hope that a back-up timer, which had been set for $\sim$ 1900 CDT on September 6, would terminate the flight. The timer also failed because some additional explosive bolts malfunctioned. An attempt to terminate the flight by opening the valve in the top of the balloon was made, but an electrical relay failed, and the valve would not open. The balloon floated on as a derelict and

FIGURE E-1

CREPE II ALTITUDE PROFILE

This plot represents the altitude profile of the CREPE II flight in gm/cm^2 of residual atmosphere. There was no telemetry after 0310 on September 7 and the remaining profile has to be pieced together from the other information as indicated.

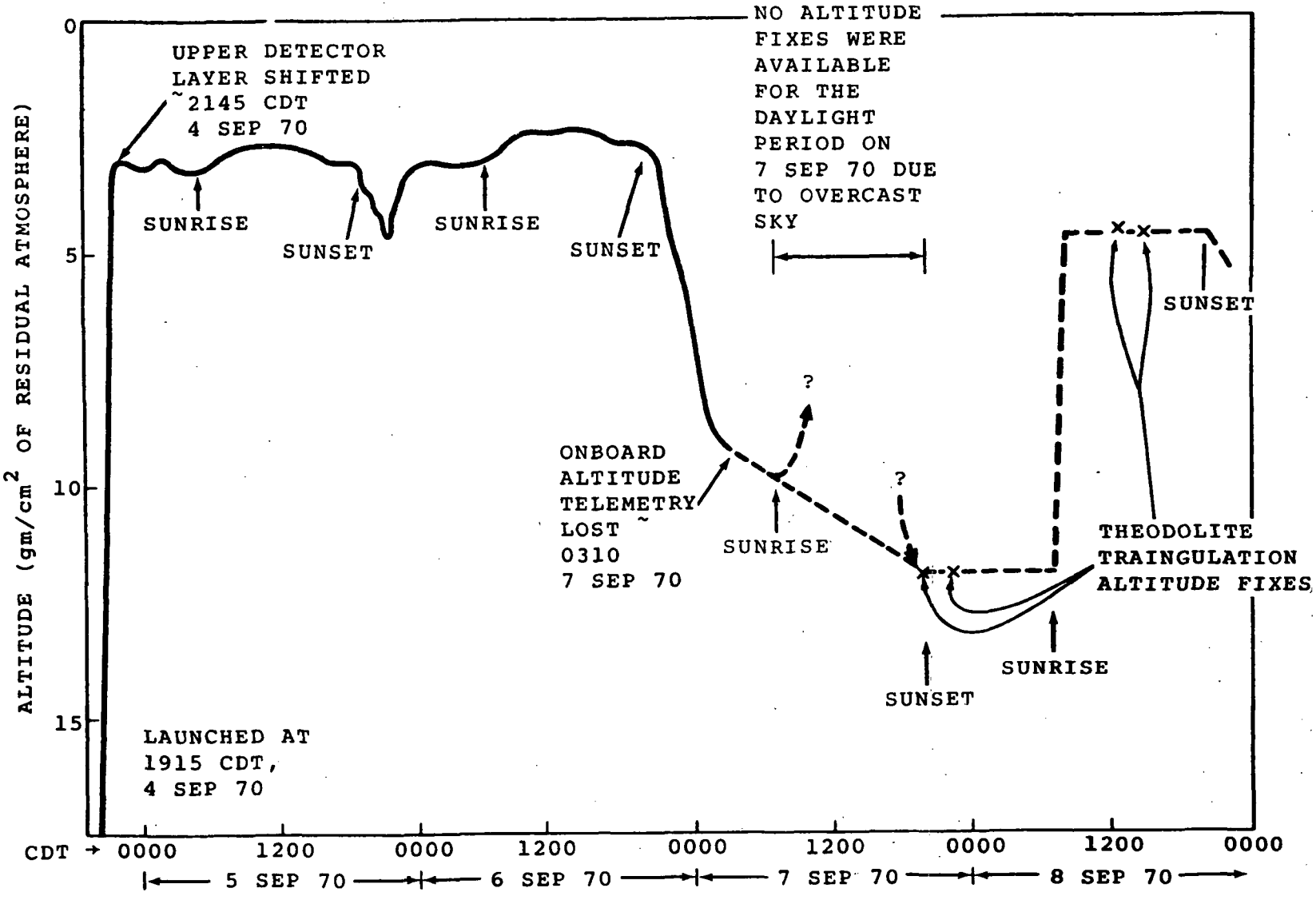
ALTITUDE (gm/cm² OF RESIDUAL ATMOSPHERE)
0
5
10
15
UPPER DETECTOR LAYER SHIFTED ~2145 CDT 4 SEP 70
SUNRISE
SUNSET
SUNRISE
SUNSET
NO ALTITUDE FIXES WERE AVAILABLE FOR THE DAYLIGHT PERIOD ON 7 SEP 70 DUE TO OVERCAST SKY
SUNSET
ONBOARD ALTITUDE TELEMETRY LOST ~ 0310 7 SEP 70
SUNRISE
?
?
THEODOLITE TRAINGULATION ALTITUDE FIXES
SUNRISE
SUNSET
LAUNCHED AT 1915 CDT, 4 SEP 70
CDT → 0000 1200 0000 1200 0000 1200 0000 1200 0000
5 SEP 70
6 SEP 70
7 SEP 70
8 SEP 70

FIGURE E-1

at ∿ 0310 CDT on September 7, the onboard altitude telemetry stopped due to battery exhaustion. From that point on, altitude data are available only from sporadic optical triangulations and less accurate radar fixes.

During the daylite hours of September 7, the balloon was over a thick cloud layer and no altitude measurements were made. The balloon most probably rose above the last recorded altitude of the previous night due to the effect of solar heating. However, the cloud layer will retard the normally seen daylight altitude gain because the reflection of the solar infrared by the clouds is far less than that experienced while over foliage. During the evening of September 7, the balloon was sighted, and a theodolite triangulation indicated an altitude ∿ 100,000 ft. (∿ 11.5 gm/cm^2). The next day the balloon rose to ∿ 120,000 ft. (∿ 4.5 gm/cm^2), where it apparently floated throughout the day. The balloon continued to drift for the next 10 days, and finally impacted near Regina, Saskachewan at 0530 CDT on September 19. During most of the latter 10 days of the flight, the balloon was over the Pacific Ocean and no altitude data are available at all. It is estimated that after the loss of the altitude telemetry (0310 CDT September 7), the balloon experienced no more than an additional ∿ 40 total hours at altitudes $\geq$ 6 gm/cm^2. The minimum additional exposure above 6 gm/cm^2 was ∿ 10 hours.

When the gondola first impacted near Regina, it was still attached to the balloon system. The balloon acted like a giant sail and dragged the package for more than five miles across the countryside, before being severed from the package by a power line. This dragging caused moderate damage to some of the fast film Cerenkov detectors as indicated in Table 3 of Chapter III.

Page intentionally left blank

APPENDIX F

PHOTOMICROGRAPH OF A CERENKOV IMAGE AND IT'S ACCOMPANYING UPPER SHEET IONIZATION SPOT

Figure F-1 contains a photomicrograph of the Cerenkov image corresponding to event number 41 in Table 3. The azimuthal direction of propagation is from about 10 o'clock to 4 o'clock, where page number represents the 3 o'clock position on the page. The upper sheet ionization spot is also pictured under the same magnification. The value of β from the measurement of the Cerenkov image is $> .95$ and the particle had a $Z > 60$ based on preliminary emulsion measurements.

FIGURE F-1

PHOTOMICROGRAPH OF A CERENKOV IMAGE AND
IT'S ACCOMPANYING UPPER SHEET IONIZATION SPOT

This figure contains a photomicrograph of a Cerenkov image and the corresponding ionization spot left in the upper sheet of the detector.

NASA
S-72-50695

FIGURE F-1

NASA — MSC